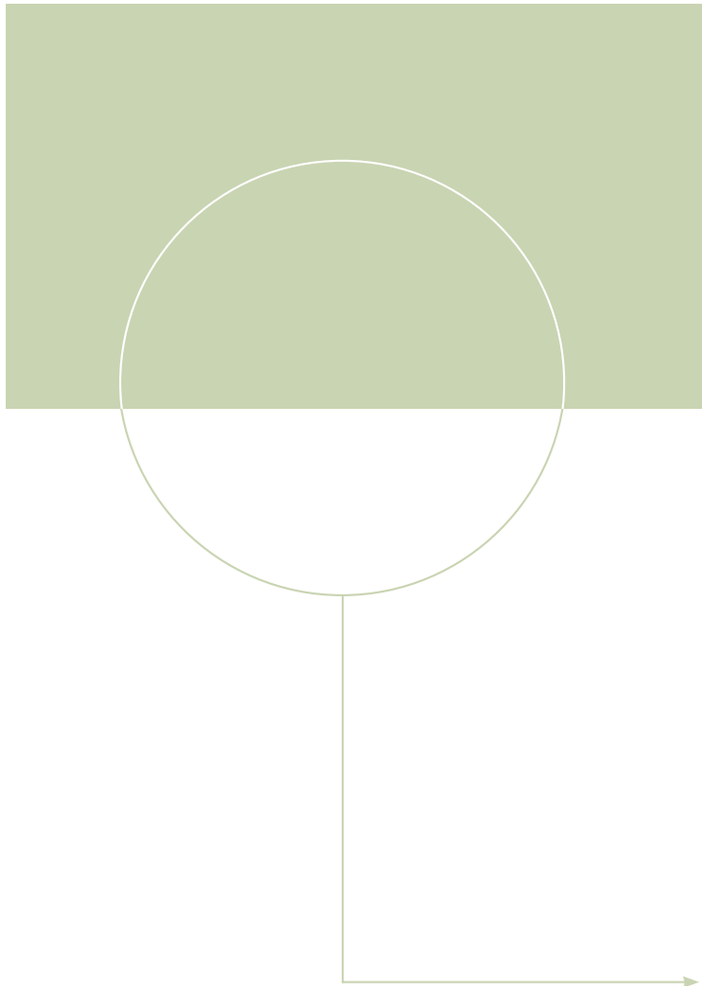

Master's thesis

2019

Eirik Andre Nordbø

NTNU
Norwegian University of
Science and Technology
Faculty of Natural Sciences
Department of Materials Science and Engineering

Eirik Andre Nordbø

Interaction of SiO-gas and Charcoal and the Formation of SiC and Si

June 2019

NTNU
Norwegian University of
Science and Technology

NTNU
Norwegian University of
Science and Technology

NTNU

Norwegian University of
Science and Technology

Interaction of SiO-gas and Charcoal and the Formation of SiC and Si

Eirik Andre Nordbø

Materials Science and Engineering
Submission date: June 2019
Supervisor: Merete Tangstad
Co-supervisor: Sethulakshmy Jayakumari

Norwegian University of Science and Technology
Department of Materials Science and Engineering

Preface

This report concerns the interaction of SiO-gas and charcoal and the formation of SiC and elemental Si. The work is the basis for evaluation in the course TMT4905 at the Norwegian University of Science and Technology, NTNU. The work has been funded by SFI Metal Production.

First and foremost, I want to give my utmost gratitude to my supervisor, Prof. Merete Tangstad. Merete has given me valuable insight even at the most hectic of times and I very much appreciate having a professor who is so devoted to her students as my supervisor.

Likewise, I want to thank my co-supervisor and Ph.D. candidate Sethulakshmy Jayakumari (NTNU) for much valued assistance and discussions. I wish her the best of luck.

I would also like to show gratitude to Ph.D. candidate Ivar Andre Ødegård (NTNU), Jonas Einan Gjøvik (SINTEF) and Ph.D. candidate Andrea Broggi (NTNU) for training in the proper use of equipment and much needed assistance once equipment descends into chaos. Additionally, I would like to thank everyone in the SiManTi group for guidance and important feedback.

At last, I would like to thank my fellow graduate students at Material Science and Engineering, NTNU. The worries of a master student disappear when one is surrounded by such amazing people. This has been five remarkable years I will never forget.

Eirik Andre Nordbø

Trondheim, June 2019

Abstract

To achieve a high yield in the silicon production process, the capture of ascending SiO-gas by reaction with carbonaceous materials to form SiC is of great importance. The following reaction between SiC and SiO-gas is known to produce elemental Si. Although several studies on the use of charcoal in silicon furnaces exist, the knowledge within this field is lacking. Newer studies indicate a lower temperature of Si formation in SiC than previously thought possible[1]. The goal of this thesis will be to investigate the interaction of SiO-gas and charcoal and the formation of SiC. Furthermore, the lower temperature of elemental Si formation in SiC will be investigated.

To accomplish this, a graphite resistance-heating furnace was used to heat up graphite crucibles containing SiO_2/Si and charcoal separated by a gas-permeable disc. Temperatures were chosen both above and below the theoretic minimum temperature of Si production and exact temperatures were measured inside the charcoal charge.

Shown in this thesis, is the formation of SiC and elemental Si from charcoal. A linear mass change of the charcoal charge was found to occur when compared with temperature. Furthermore, this study shows a significant growth of mono- and poly-crystals both on the particle surface and inside pores. The various morphologies of these crystals, combined with XRD results, confirm 3C β-SiC and indicate to 4H α-SiC. Structural changes in charcoal were observed as it converts to SiC and crystal growth inside pores is believed to have caused this. Finally, elemental Si was found to have been formed at 1781.8 °C, which is below the theoretic minimum temperature of Si formation.

Samandrag

For å nå eit høgt utbytte i produksjonen av silisium, er det viktig å fange stigande SiO-gass ved reaksjon med karbonhaldig materialar for å danne SiC. Den påfølgjande reaksjonen mellom SiC og SiO-gass er kjend for å produsere elementær Si. Til trass for fleire studiar om anvendelegheita av trekol i silisiumsomner er kunnskapen innanfor dette feltet manglande. Nyare studiar indikerer mot en lågare temperatur for silisiumsproduksjon i SiC enn tidlegare tenkt mogleg. Målet med denne avhandlinga vil vere å utforske interaksjonen mellom SiO-gass og trekol og formasjonen av SiC. Vidare vil den lågare temperaturen for silisiumsproduksjon i SiC bli granska.

For å oppnå dette, vart ein omn med varmeelement av grafitt brukt for å varme opp grafittdiglar med SiO_2/Si og trekol separert med ein gass-gjennomtrengeleg disk. Temperaturar vart valt både over og under den teoretiske minste temperaturen for Si-produksjon og eksakte temperaturar vart målt inne i ladninga av trekol.

Vist i denne oppgåva, er formasjonen av SiC og elementær Si frå trekol. Ein lineær samanheng vart funnet mellom endring i massen til trekolet når samanlikna med temperatur. Vidare viser studien ein signifikant vekst av både ein- og fleirkrystallar på både partikkeloverflater og innsida av porer. Dei ulike krystallmorfologiane, saman med resultat frå XRD-analyse, bekrefter 3C β-SiC og indikerar til 4H α-SiC. Strukturelle endringar vart observert når trekol blir konvertert til SiC og krystallvekst inne i porer er tenkt til å forklare dette. Det ble òg funne elementær Si ved 1781.8 °C, ein temperatur som er under teoretisk minimum for Si-produksjon.

Contents

Chapter 1

Introduction

Silicon is one of the most abundant elements in the earth's crust and has a foothold within many important industries: it is used to improve the strength of concrete, to increase the castability of metals, and as semiconductors in the electronics industry. Furthermore, the demand for pure silicon for use in solar cells seem to only be increasing as the world aims for cleaner energy sources. To fulfill these increasing demands, the production process for silicon should always be in the subject of improvement.

In a typical silicon furnace, high temperatures are combined with carbonaceous materials to reduce quartz (SiO_2) to silicon. A mixture of woodchips, charcoal, and coal is added as carbon materials. The main difference between silicon and ferrosilicon furnaces is the source of iron which is added to the furnace charge mixture. The main product, silicon or a ferrosilicon alloy, is tapped through one of several tapholes positioned at the lower part of the furnace. A secondary product, microsilica (SiO_2) is captured from the effluent gas.

The energy required for this process is supplied from the electric arc which is produced by one or more submerged electrodes in the charge mixture. The most common furnace design applies a three-phase alternating current as electrical power and has three electrodes which together function as both cathode and anode. Söderberg electrodes are normally used when producing FeSi alloys due to the large amounts of iron in the electrode casing. When the product is pure silicon, a similar continuously baked electrode is used, where the mechanical strength comes from a graphite core instead of an iron casing. This is known as a composite electrode. Compared with a Söderberg electrode, the composite electrode does not contaminate the silicon with iron.

Both furnace design and operation has a large influence on the temperature distribution in the fur-

nace, which can be anywhere between 700°C at the surface to 2000°C in the core. Directly in the electric arc produced by the electrodes, the temperature can exceed the core temperature by several thousands of degrees.

$$SiO_2 + 2C = Si + 2CO(g) \tag{1.1}$$

Reaction (1.1) shows a simplification of the reduction of quartz to silicon. During the complete and more complex reduction, the intermediate compounds SiO (g) and SiC are also formed through several intermediate reactions. While SiO (g) is produced through reactions (1.2) and (1.3) mainly in the high temperature zone, SiC can be formed at much lower temperatures through several reaction mechanisms.

$$2SiO_2 + SiC = 3SiO(g) + CO(g) \tag{1.2}$$

$$SiO_2 + Si = 2SiO(g) \tag{1.3}$$

Some of the SiO (g) reacts together with SiC at temperatures around 1800 °C in what is known as the main silicon producing Reaction (1.4). The remaining SiO(g) rises upwards in the furnace to be captured by descending carbon in Reaction (1.5) to produce SiC. Note that Reactions (1.2) and (1.3) are reversible reactions where SiO-gas can be both a product and a reactant. During the rise of the SiO(g) to the cooler zone, condensation will occur given low enough temperatures, through the reverse direction of Reaction (1.3). SiO(g) can also react with CO(g) in the reverse direction of Reaction (1.2). Reaction (1.5) and the reverse direction of Reactions (1.2) and (1.3) are important for the capture of SiO(g) and to achieve a high silicon yield.

$$SiO(g) + SiC = 2Si + CO(g) \tag{1.4}$$

$$SiO(g) + 2C = SiC + CO(g) \tag{1.5}$$

The silicon yield is the mass of silicon produced compared with the mass of silicon in the raw materials. For obvious economic reasons, the industry wants the highest yield possible. A low silicon yield can almost always be traced to a high loss of SiO (g) to the effluent gas. The accumulation of silicon containing compounds, such as SiC, in the furnace can also contribute to a reduced silicon yield.

However, compared with the loss of SiO(g), the effect of SiC accumulation on the silicon yield is negligible. Still, the long term effect of accumulated species and the resulting furnace clogging can be devastating. During the excavations of several ferrosilicon and silicon furnaces, a significant amount of α-SiC was discovered[2]. Once formed, these solid deposits are difficult to remove. The accumulation will obstruct the process and can eventually lead to the end-of-life of the furnace. With this said, the interaction between SiO(g) and carbonaceous materials to form SiC is of great importance to the silicon production process.

With this in mind, it is not surprising that research within the silicon production industry is often directed towards the reaction between SiO(g) and carbon to form SiC. This type of research is often accompanied by the increasing attention towards the use of non-fossil charcoal. To better understand how different carbon materials react with SiO(g), Raaness & Tuset (1976)[3] developed the SINTEF SiO-reactivity test in the 70s, a test which is still in use today. Other publications of importance within this field is the research of Myrhaug (2003)[4] and Ramos (2018)[5] on the use of charcoal in the silicon process. In a newer unpublished study of Jayakumari (2018)[1] on the transformation of β- to α-SiC, elemental silicon was found to be formed in β-SiC particles at temperatures less than 1800 °C.

Despite the research mentioned above, it is believed that the research on the interaction between SiO(g) and charcoal is lacking relative to its importance. As there were severe complications with the only furnace which could both reach 1800 °C and accurately measure temperatures, the work shifted away from varying parameters such as carbon material, SiO-pressure, and holding time. Instead, more time was spent on characterization. Hence, the goal of this master thesis will be to investigate the transformation of charcoal to SiC when exposed to SiO-gas. The resulting particles will be thoroughly investigated using characterization techniques such as Scanning Electron Microscopy (SEM) and X-Ray Diffraction (XRD). Furthermore, the lower temperatures of elemental silicon formation in SiC will be investigated in accordance following the finds of Jayakumari.

Chapter 2

Theory

2.1 Si-C system

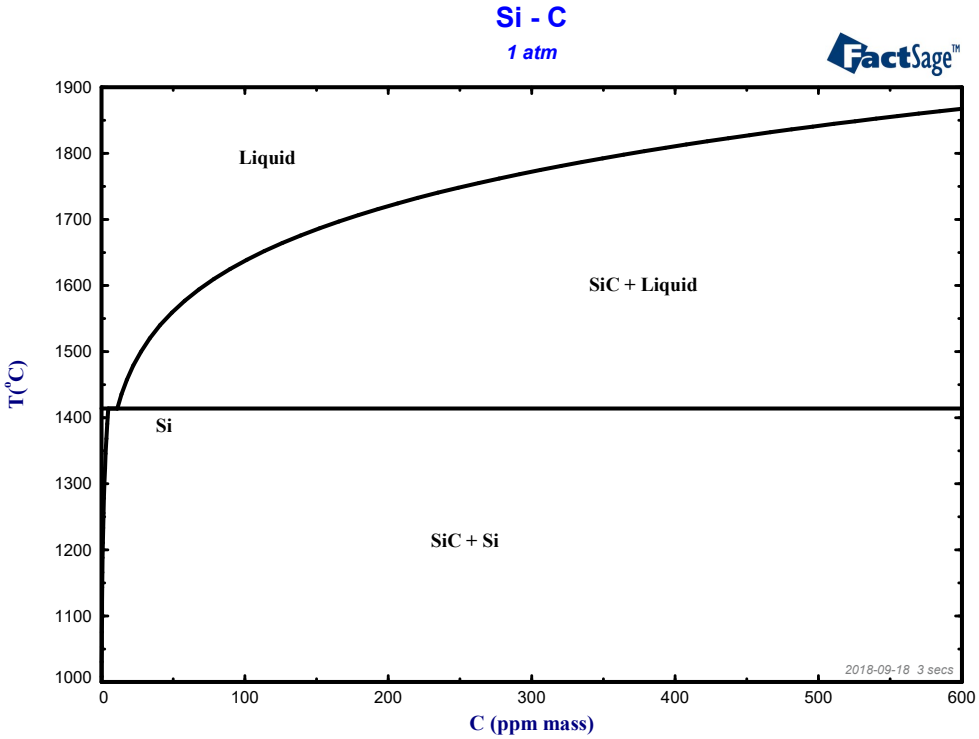

Figure 2.1: Si-C phase diagram at low carbon concentrations. Diagram is created by NTNU PhD candidate Jian Meng Jiao in FactSage with the FSupsi database.

A Si-C phase diagram for very low C contents was created by using FactSage with the FSupsi database. The resulting diagram is plotted in Figure 2.1. The solubility of C in Si is much lower for the solid phase, compared with the liquid phase. Hence, after the solidification of a C saturated Si solution, the dissolved C will be less than 10 ppm. According to the phase diagram, this C will precipitate as SiC. Si, graphite and their compound, SiC, are the only stable crystalline phases in the Si-C system. Dolloff (1960)[6] found the eutectic transformation temperature to be 1404 ± 5 °C at a C concentration of 0.75 ± 0.5 at%. The melting point of pure Si is found to be 1415 ± 5 °C.

SiC can, depending on the stacking of the atomic layers, exist in many different types of polytypes. A Ramsdell notation, where a number is followed by a letter, is often used to organize the many polytypes. The number represents the number of double layers in the stacking sequence and the letter represents crystal structure.

Harris (1995)[7] has done extensive research on the properties of SiC. The 3C (cubic) is typically referred to as β-SiC, while the hexagonal (H) and rhombohedral (R) crystal structures are referred to as α-SiC. The 6H is the most stable and common polytype of the α-SiC. The 3C transforms to 6H at temperatures above 2000 °C. The 3C β-SiC exhibits a yellow or greenish-yellow colour depending on the impurities. SiC has a density in the range from 3.17 to 3.25 g/cm^3 depending on the polytype. The 3C polytype has a density of 3.21 g/cm^3.

2.2 Si-O system

One of the earliest constructed phase diagrams of the Si-O system indicates the presence of SiO as a stable crystalline phase. Additionally, the phase diagram indicates to complete miscibility between Si and SiO_2. This phase diagram has later been criticized for being "erroneous" and "highly speculative"[8, 9].

In their study to construct a correct Si-O phase diagram, Johnson & Muan (1968)[9] heated up mixtures of SiO_2 and Si in a vertical-tube furnace. CO_2-gas was passed through the furnace during the 0.5 to 1 hour long runs and the samples were subsequently quenched. Their resulting phase diagram, shown in Figure 2.2, confirms the presence of only one stable solid compound in the Si-O system, namely SiO_2. Both Schei et al. (1998)[10] and Wiik (1990)[8] point out the diagram to be correct in principle, but also that it should not be used for quantitative purposes. SiO is also a stable compound in the Si-O system; however, only in a gaseous state at high temperatures.

There are three crystalline forms of SiO_2 at atmospheric pressure: quartz, tridymite, and cristobalite. Furthermore, each of these crystalline forms can be subdivided into low and high temperature modi-

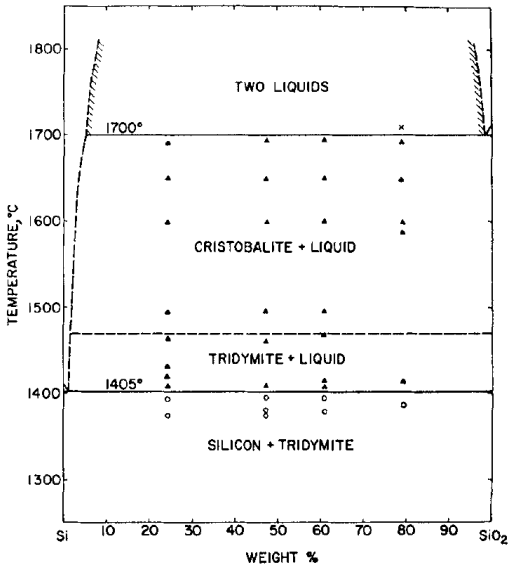

Figure 2.2: Si-O phase diagram from Johnson & Muan (1968)[9]. Dashed lines represent boundary curves whose precise location have not been determined.

fications (α and β respectively). The temperature of transformations between these crystalline forms of SiO_2 are collected from Wells (1984)[11] and is summarized in Table 2.1. The high temperature modification β-cristobalite melts at 1710 °C[11].

Table 2.1: Transformation temperatures between different crystalline forms of SiO_2 from Wells (1984)[11]. α and β is low and high temperature modifications, respectively.

Transformation	**Temperature (°C)**
Quartz → Tridymite	870
Tridymite → Cristobalite	1470
α- → β-Quartz	573
α- → β-Tridymite	110-180
α- → β-Cristobalite	218± 2

2.3 Si-C-O

Gibbs phase law can be written as $Ph + F = C + 1$ for systems with one fixed variable, such as temperature or pressure. Schei et al. (1998)[10] argue that for high-temperature systems, the number of components, C, can be simplified to the number of elements. By this approximation, C is equal to 3 (Si, C, and O) and the phase law becomes $Ph + F = 4$. By varying the degree of freedom, F, the reactions in the system can be identified. At $F = 1$, one variable needs to be given to determine the

complete system, which translates to a line on a binary phase diagram. Henceforth, the number of phases, Ph, is 3 (one gas phase and two condensed phases). Reactions that fulfill this criteria are summarized in Table 2.2. Similarly, the two triple points in the phase diagram can be identified at $F = 0$.

Table 2.2: Reactions in the Si-C-O-system according the Gibbs phase law with one fixed variable and at one degree of freedom (F=1).

Reaction	**Comment**
$SiO_2(l) + C(s) = SiO(g) + CO(g)$	
$2SiO_2(l) + SiC(s) = 3SiO(g) + CO(g)$	
$SiO_2(l) + Si(l) = 2SiO(g)$	
$SiO(g) + 2C(s) = SiC(s) + CO(g)$	
$SiO(g) + C(s) = Si(l) + CO(g)$	Metastable
$SiO(g) + SiC(s) = 2Si(l) + CO(g)$	

To better understand which of the reactions in Table 2.2 will occur and under which conditions, the partial gas pressure has to be included in the calculations. The common rule that reactions go to the right when $\Delta G^\circ < 0$ is only true for reactions containing no mixtures (or gas). For reactions containing one or more gas species, either as a reactant or product, the partial pressure of this gas has to be included.

By using data from the JANAF Thermochemical Tables and assuming that the sum of the partial pressure of SiO- and CO-gas is equal to one bar, Schei et al. (1998)[10] calculates an equilibrium diagram containing the reactions in Table 2.2 (not including the metastable reaction). This equilibrium diagram can be seen in Figure 2.3. The phases stable in each region of the diagram are noted. The invariant point and the minimum temperature where Si can be produced can be seen at 1811 °C. According to this diagram, the required partial pressure of SiO-gas for the Si producing reaction declines when the temperature increases. Furthermore, the condensation of SiO-gas will occur somewhere below 1811 °C, depending on the partial pressure. The condensation reaction will produce SiO_2 & Si. Alternatively, SiO-gas can react with CO-gas to form SiO_2 & SiC.

For comparison, a similar equilibrium diagram is created using the HSC Chemistry 9 database and is shown in Figure 2.4. A β polytype of SiC and a liquid phase of SiO_2 was assumed. In the resulting diagram, the triple point is found at a temperature of 1800 °C, significantly lower 1811 °C as calculated by Schei et al.

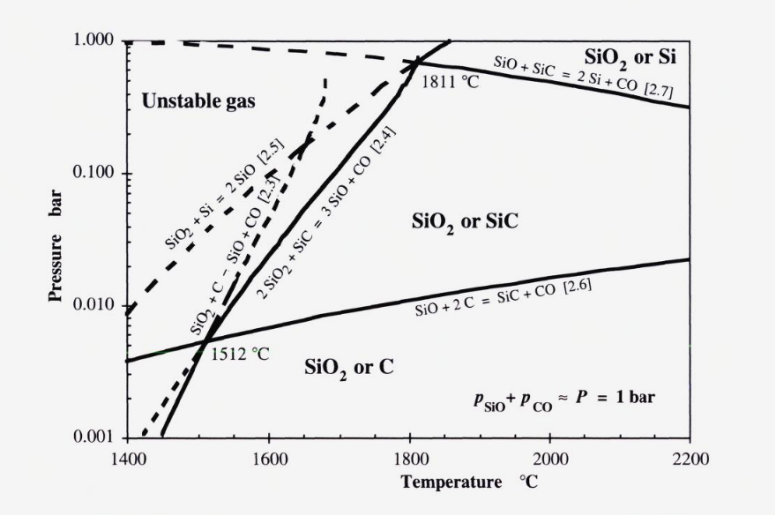

Figure 2.3: Equilibrium diagram of the Si-C-O-system with SiO-gas partial pressure on the y-axis and temperature on the x-axis. The dotted lines indicate that the gas composition lies in an unstable area. The equilibrium diagram is constructed by Schei et al. (1998)[10] using the JANAF Thermochemical Tables.

2.4 Kinetics

According to Szekely et al. (1976)[12], a gas-solid reaction can typically be divided into several intermediate steps such as:

1. **External mass transfer:** Gaseous diffusion or transport of reactants and products between the bulk of the gas phase and the internal surface of the reacting solid particle.

2. **Pore diffusion:** Diffusion of gaseous reactants or gaseous products through the pores of a solid reaction product or the pores of a partially reacted solid.

3. **Adsorption/desorption:** Adsorption and desorption of gaseous reactants on and from the solid surfaces.

4. **Chemical reaction:** Chemical reaction between adsorbed gas and the solid.

Any of these steps might be rate-determining and limit the rate of the entire gas-solid reaction. Additionally, which step is considered rate-determining can be a function of both temperature and particle size. At high temperatures, diffusion is expected to be rate-determining, while at low temperatures, the chemical reaction may be rate-determining. Other variables, such as porosity and the extent of reaction of the solid is also important. Structural changes of the particle are expected due to the reaction process. Furthermore, exothermic and endothermic reactions will be accompanied by the transfer of heat (convection/conduction), which leads to additional structural changes. These

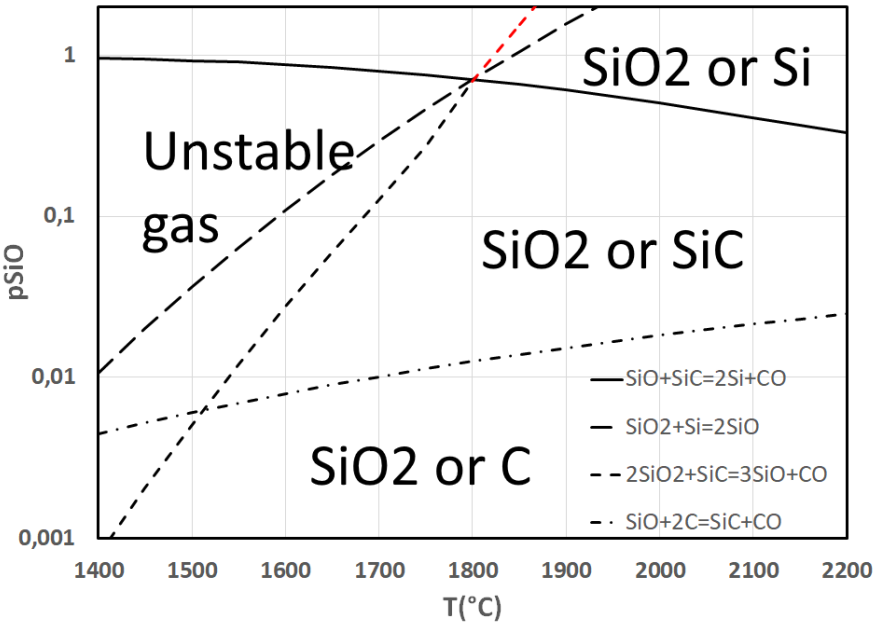

Figure 2.4: Equilibrium diagram of the Si-C-O-system with SiO-gas partial pressure and temperature as variables. The equilibrium diagram is constructed assuming a total pressure of one atmosphere with the HSC Chemistry 9 database. The dotted red line are values extrapolated from the corresponding dotted black line.

structural changes can affect the overall reaction rate.

2.4.1 Shrinking core model

During a study on the combustion of carbon particles in flames and fluidized beds by Yagi & Kunii (1955)[13], the shrinking-core model was first developed. In this study, the combustion of single carbon particles is investigated with the assumption that a layer of ash remains around the unburned core of the particle. Initially, only the mass transfer through the boundary film and the chemical reaction has to be accounted for. However, due to the assumption of a solid layer of ash remaining around the unburned core, the diffusion of gas through the solid layer also has to be considered. Figure 2.5 illustrates how the overall particle size remains constant, while the unreacted core shrinks, hence the name shrinking-core model.

In his book on extractive metallurgy, Rosenqvist (2004)[14] investigates the kinetics of the shrinking-core model. Depending on the temperature and the product layer thickness, the rate-determining step can be diffusion, chemical reaction, or a combination of these two.

Assuming that the chemical reaction is the slowest step in the reaction, Rosenqvist derives Equation (2.1) for the complete reaction time. This scenario best describes low-temperature systems where

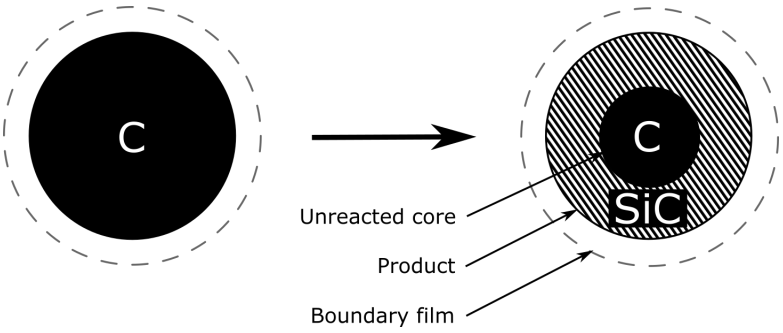

Figure 2.5: Illustration of the shrinking core model during the reaction between SiO-gas and C to form SiC.

a porous product layer is formed. The variables are the initial particle diameter, d_0, density, ρ, and the molecular weight, M. The final variable is the rate per unit area, R_A. In this equation, time is proportional to the particle diameter, d_0.

$$t_{tot} = \frac{d_0 \rho}{2 R_A M} \tag{2.1}$$

Similarly, Equation (2.2) is derived assuming that diffusion is the slowest step of the reaction. This assumption is well suited for reactions where a dense product layer is formed. In the following variables, the diffusing species is denoted as B. The new variables in the equation are pore diffusivity, D_B, and the difference between the diffusing species B on the external surface and the reacting surface, ΔC_B. As seen in this equation, time is proportional to the square of the particle diameter.

$$t_{tot} = \frac{{d_0}^2 \rho_B}{24 D_B \Delta C_B M_B} \tag{2.2}$$

Similarly, assuming that the overall reaction rate is determined by both chemical reaction and diffusion, Szekely et al. (1976)[12] derived an equation for the overall reaction time. The non-dimensionless time variants of the equation tell the same story: time is proportionate to the square of the particle radius.

The presence of pores does complicate things. As pointed out by Rosenqvist, Equations (2.1) and (2.2) both assume the formation of a dense product layer, while in many cases, the product layer can be porous. First of all, pores contribute to the transport of reactants and products, which again gives a faster complete reaction time than what is told by the two equations. Secondly, a porous substance can be volume controlled, i.e. the reactions take place throughout the entire volume of the particle, independently of particle size. The volume control phenomenon is related to low particle sizes. At larger particle sizes, the shrinking core model better describes the system.

In his studies, Myrhaug (2003)[4] found indications that pores do contribute to the transport of SiO- and CO-gas. To highlight the contrast between the two different phases, C and SiC, BSE images were taken of a partially reacted particle of charcoal. One such image shows an increased degree of conversion along the parallel cell structures, which indicate that pores transport the SiO-gas better.

Although based on the combustion of carbon particles, the shrinking core model is also fit to describe the reaction between carbonaceous materials and SiO-gas in a Si furnace.

In a study on the use of non-fossil reduction materials in the Si process, Myrhaug (2003)[4] investigated various kinetic models for the reaction between SiO-gas and carbonaceous materials. The complete shrinking-core model was compared with the two cases where either diffusion or chemical reaction was rate determining. For comparison with the kinetic models, thermogravimetric experiments with carbonaceous material and SiO-gas was run at 1650 °C. By measuring the weight of carbonaceous spheres at different times as the spheres are exposed to known gas concentrations of SiO, CO, and Ar, and by using the known reaction between SiO-gas and C to form SiC and CO-gas (Reaction (1.5)), the necessary kinetic parameters were obtained. The resulting comparison between the kinetic models indicates that charcoal was best simulated with the ordinary shrinking-core model. Hence, at 1650 °C, the reaction between SiO-gas and charcoal is limited by a combination of chemical reaction and diffusion. For the much less reactive coke, the diffusion-limited shrinking-core model was the best fit with experimental data.

2.4.2 Morphology

As many crystals composed of SiC was observed during this thesis, it became necessary to investigate the mechanism of growth and resulting shape to understand the underlying crystal structure. This in turn can assist in identifying which polytypes of SiC is present.

After a stable nucleus has been formed further growth can be limited by amongst others, the kinetics of atom attachment to the nucleus interface. According to Kurz & Fisher (1989) [15], these kinetics can decide if a substance exhibits a *faceted* or *non-faceted* morphology. During the solidification of a *non-faceted* material, typically metals, atoms can easily be added to any point of the interface. In this case, capillary effects and diffusion of heat or mass will dictate a typically smooth final structure. On the other hand, a *faceted* material, typically intermetallic compounds or minerals, will have a morphology depending on the growth rate of the different index planes. The macroscopic difference between faceted and non-faceted growth is illustrated in Figure 2.6. Rougher high-index planes have a faster growth rate, which as a result leads to the crystal being bound by the slower growing low-

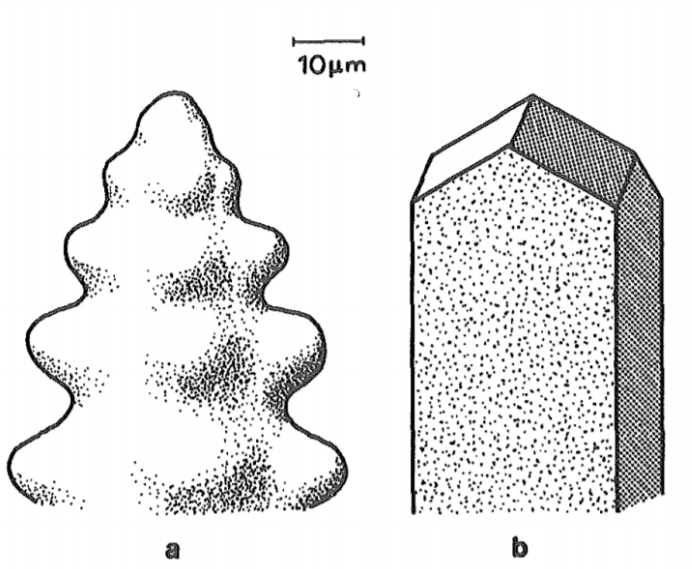

Figure 2.6: Non-faceted growth, (a) vs faceted growth (b). Illustration originates from Kurz & Fisher (1989) [15].

index planes. A comparison between two different plane growth rates for the simple cubic system, and the resulting crystal morphology, is illustrated in Figure 2.7.

In general, the greater the difference in structure and bonding between the two phases, the more difficult it is for incorporating new atoms between them. This difference is well demonstrated by the use of entropy. A convenient criterion for predicting faceted or non-faceted crystal growth during solidification of a liquid is by using the melting entropy (Equation (2.3)). A value of α lower than $\sim$2 has a tendency towards non-faceted growth, while larger α-values prefer a faceted growth. According to Kurz & Fisher, semi-conductors or -metals, such as Si, has α equal to 2-3 and can grow as either faceted or non-faceted crystals.

$$\alpha = \frac{\Delta S_f}{R} \tag{2.3}$$

However, there is a much larger entropy difference between gases and solids. For this reason, crystals grown during solidification of a liquid substance can be smooth (non-faceted) compared to the rough (faceted) crystals formed during the deposition of a gas.

During crystal growth, atoms will be adsorbed on the crystal surface and through diffusion move to a more stable position. Atoms continuously enter and leave the system through adsorption and desorption. Logically, more chemical bonds result in a more stable atom on the surface. For this reason, the step between a lower terrace and a raised layer is the more favourable position. A *kink* is

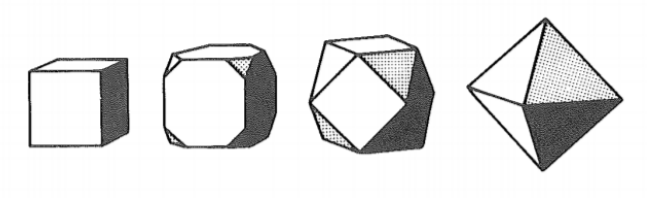

(a)

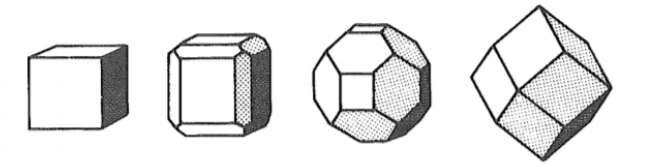

(b)

Figure 2.7: Different growth rates of index planes can result in different crystal morphologies of the simple cubic structure. **(a)** is bound by the (111) plane due to a fast growing (100) plane. **(b)** is bound by the (110) plane. Usually the low-index planes such as the (110) are the slowest growing planes, which would result in scenario **(b)**. Illustrations are collected from Kurz & Fisher (1989)[15].

a term describing a corner position on a step. With that said, kink sites are more stable for adsorbed atoms due to the many chemical bond sites there. However, the kink sites are limited, and at some point a new raised layer or *island* has to be nucleated. Such nucleation does, however, have a free energy barrier. This crystal growth mechanism is described by both Chernov (1961)[16] and Kurz & Fischer (1989)[15]. An illustration is also shown in Figure 2.8.

Typically, the crystal morphology is dictated by the underlying crystal structure. A few examples of this in practice are presented here. There are some studies by Sotillo et al. (2014 & 2015)[17, 18] on the crystal structure of doped ZnS, which typically have a cubic or hexagonal crystal structure. Typically, the transformation between cubic to hexagonal ZnS occurs around 1020 °C. After initial heat treatments above 1020 °C, XRD revealed the hexagonal wurtzite crystal structure. Characterization using SEM also shows the crystals grown as hexagonal pyramids, sometimes with and sometimes without a tip. Similarly, the hexagonal (4H) α-SiC has been grown by Harada et al. (2013)[19] at 1700 °C using a Top-Seeded Solution Growth (TSSG). The resulting morphology of these crystals is also hexagonal. The lowest temperatures of hexagonal α-SiC growth is reported by Matsunami (1991)[20] at 1500 °C using a Chemical Vapour Deposition (CVD) method. These crystals which had a hexagonal shape were confirmed to be hexagonal α-SiC.

By varying temperature and flux of reactants in the CVD of Si film on a Si substrate, Bloem (1979)[21] found that the resulting Si crystal structure varies between three modes of heterogeneous nucleation: mono-, amorphous-, and poly-crystalline growth. Mono-crystals have the same growth directions,

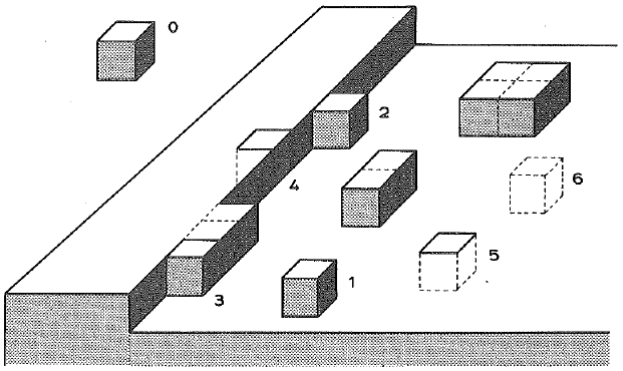

Figure 2.8: Mechanism of crystal growth at a step by Kurz & Fischer (1989)[15]. Atoms are illustrated as cubes. The illustration shows the different possible positions of a newly adsorbed species. In general, the more neighbouring bonds, the more stable the position of the adsorbed atom is. With this in mind, the atom is position 3, typically referred to as a *kink* on a step, is surrounded by most bonds and is most stable. In comparison, the atoms in position 1 could start a new raised layer typically called an *island* if the size reaches a critical level.

poly-crystals can have several directions, and amorphous-crystals lack any long-range order of atoms. It is stated by Bloem that the nucleation of Si on a Si substrate is the most straightforward example which illustrates how various parameters can affect the nucleation process. The proposed mechanism of amorphous crystal growth is a large flux of newly adsorbed atoms combined with low diffusivity. Consequently, there are many new atoms and too little time for the diffusion of new atoms to more energetically favourable crystallographic sites. The results of Bloem, as seen in Figure 2.9, are well summarized by Cao (2004)[22]:

- Growth of mono-crystals is most difficult and requires amongst other things, a high growth temperature, and a low impinging rate of growth species (allow sufficient structural relaxation before the arrival of the next growth species).
- Amorphous films occur under low growth temperatures, and/or during a large influx of growth species.
- Poly-crystalline films grow under conditions between mono- and amorphous-crystals. Hence, a moderate temperature with a relatively high flux of growth species is required.

In addition to temperature and flux of reactants, the final morphology of a crystal will also depend on impurities and the surface on which it grows. Impurities or trace elements can also affect the growth rate of different facets. They can both impede or increase the growth[17, 18, 23]. A well known industrial example of this phenomenon is the addition of magnesium to molten iron before casting to induce the formation of nodular graphite particles inside the iron matrix. On the other

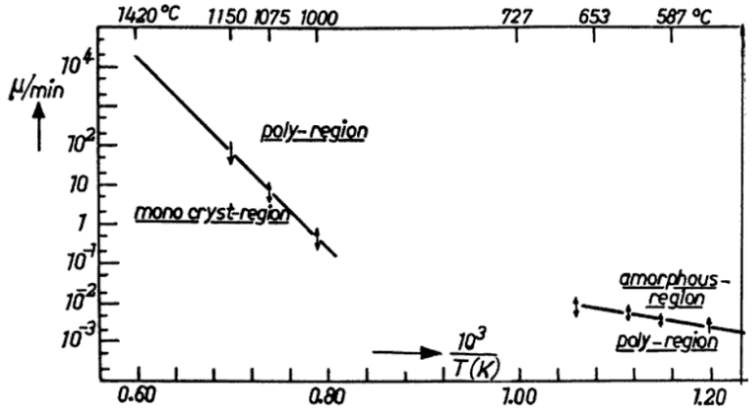

Figure 2.9: Figure collected from Bloem (1979)[21] and illustrates how temperature and the growth rate (from the flux of reactants) can affect the final crystal morphology. At higher temperatures with a large flux of reactants, a poly-crystalline growth is preferred. If the temperature is sufficiently high, but the flux of reactants is low, the growth of mono-crystals can occur. Amorphous crystals are found at both low temperatures and low growth rates.

hand, the presence of sulphur will lead to the formation of graphite flakes. Nodular graphite particles are sometimes preferred as they increase the ductility of the cast iron. Furthermore, crystals grown on defects can have crystal structures depending on the defect[15].

2.5 SiO-reactivity

One method to investigate the reactivity between different carbons and SiO-gas is by use of the SINTEF SiO-reactivity test developed by Raaness & Tuset (1976)[3]. Earlier reactivity tests were based on the oxidation of carbon, which is argued to not be comparable with the reaction between SiO-gas and carbon (Reaction (1.5)). The author points to the formation of a β-SiC layer around carbon particles, which effectively slows down the reaction. Hence, the reactivity tests based on the oxidation of carbon is not comparable with the reaction between carbon and SiO-gas.

A mixture of SiO_2 and SiC reacts to form SiO (g) according to Reaction (1.2). At 1650 °C the evolved gas contains 13.5% SiO and 4.5% CO according to equilibrium. This gas mixture is transported by the use of Ar as a carrier gas into a chamber containing a sample carbon material. Assuming that only Reaction (1.5) occurs inside the sample chamber, Raaness & Tuset measures the degree of C to SiC conversion by measuring the content of CO in the effluent gas against time. The resulting profile of CO vs. time can be used to quantify the reactivity of the sample carbon material. Figure 2.10 shows such profiles of a reactive material, (a), compared with a less reactive material, (b). The

authors mention the possibility of SiO- and CO-gas counter-diffusion through the pores of the partly converted material to be rate controlling for the overall reaction. The SiO-reactivity test was further improved in 2007[24].

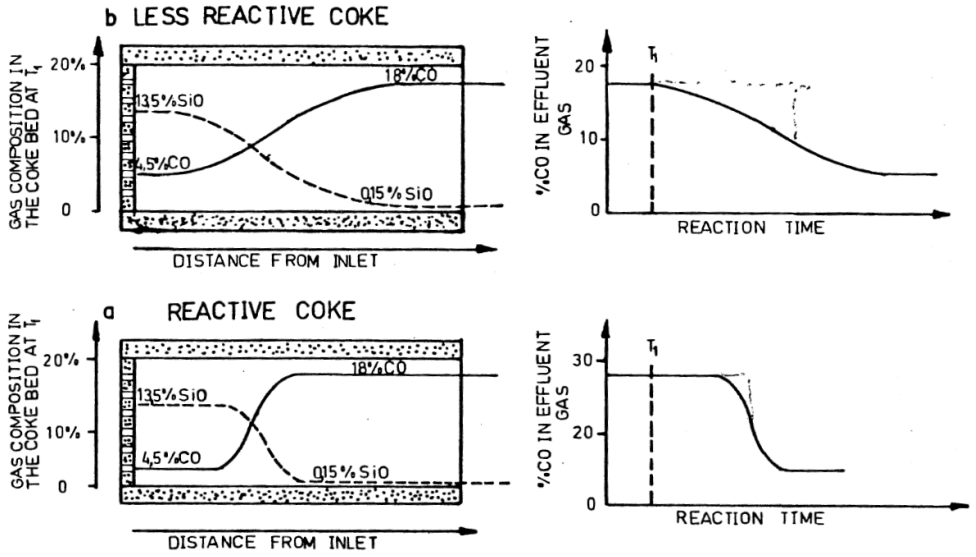

Figure 2.10: Tentative gas compositional profiles through a bed of (a) reactive material and (b) less reactive material. The corresponding CO-gas vs time profiles illustrates the steep curve which characteristic for the reactive material. Figure is taken from Raaness & Tuset (1976)[3].

2.6 Similar works

NTNU Ph.D. candidate Jayakumari (2018)[1] studied the high-temperature transformation of β- to α-SiC. This transformation is believed to occur around 2000 °C. The study is based on the large amounts of α-SiC found during furnace excavations by Ksiazek et al. (2016)[2].

At first, the author produced β-SiC for use as raw materials in the study of the β- to α transformation. The SiO-gas was produced by a mixture, placed at the bottom of a crucible, consisting of either SiO_2/Si or SiO_2/SiC. Directly on top of this SiO-producing mixture, a charge of carbon material was added. Hence, there is physical contact between the Si-containing mixture and the carbon materials. This setup, including the position of two thermocouples, is depicted in Figure 2.11. The crucibles were heated to target temperatures in an induction furnace. In the following characterization, the carbon particles converted to β-SiC was investigated. Some particles were cast in an iodoform-containing epoxy and investigated with an Electron Probe Micro Analyzer (EPMA).

It is emphasized that the data from these experiments have been retrieved by personal communica-

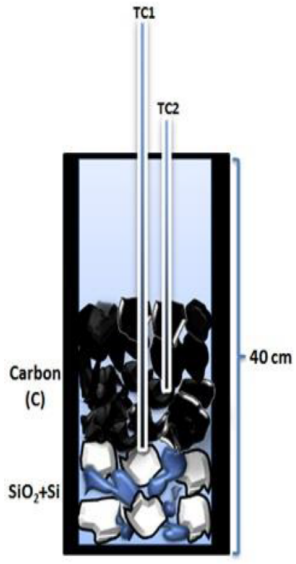

Figure 2.11: Illustration of the experimental setup. The figure is collected from Jayakumari[1].

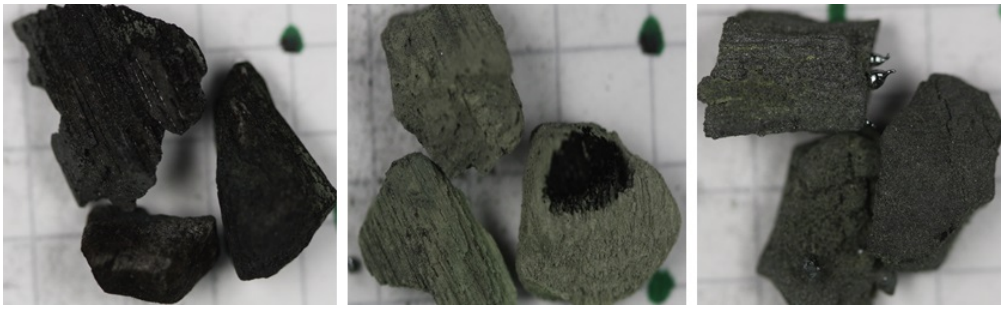

Figure 2.12: From Jayakumari (2018)[1]. After experiments with charcoal, particles was collected from the charcoal charge. From left to right, the change of colour is believed to illustrate the degree of transformation from black charcoal to grey-blue SiC. Some elemental Si is visible on the surface of the latter.

tion between the author and Jayakumari.

Visually, three different particle types could be identified. While using charcoal as the carbon material, experiments were run at target temperatures of 1750, 1800, 1850 and 1900 °C. The results from the carbon charge after one of these experiments is shown in Figure 2.12. Three different colours, or types of particles, can be distinguished: black, yellow-green and grey-blue. From left to right the colours are believed to illustrate the degree of transformation from C to SiC. This also corresponds to their location in the carbon charge, where black particles were found on top, far away from the SiO-producing mixture, while grey-blue particles are found on the bottom. Elemental Si, in the form of droplets, is visible on the surface of the grey-blue particles to the right in Figure 2.12.

One of the characterized charcoal particles had an unreacted core of carbon, which was surrounded

by a product layer of SiC. The experiment, where charcoal was used as the carbon material and SiO_2/Si as SiO-producing mixture, had a target temperature of 1830 °C. One of the particles located in the middle of the carbon charge is imaged using a mapping technique with EPMA, and is shown in Figure 2.13. A pink, purple or red colour indicates to a high concentration of the respective element. With this in mind, it can be concluded that the particle is partially reacted to SiC with an unreacted core of C. This particle appears to follow the shrinking-core model.

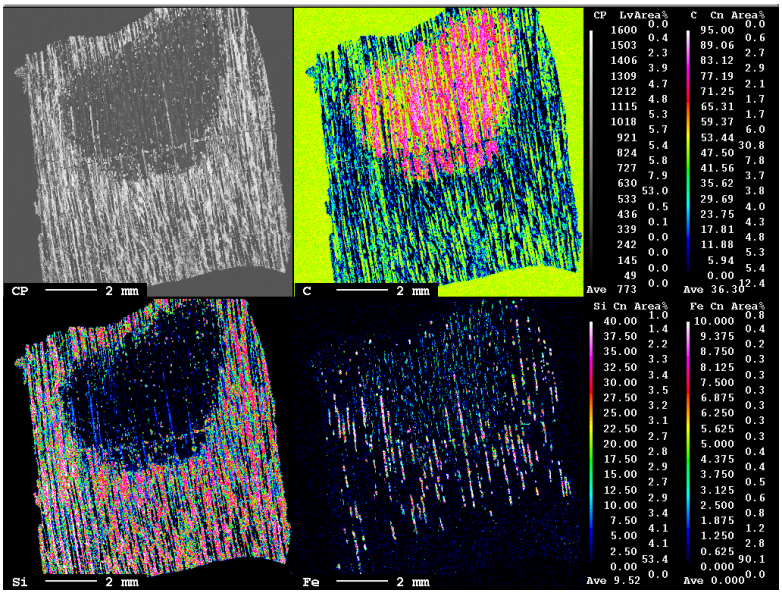

Figure 2.13: Jayakumari (2018)[1]. At 1830 °C whilst using charcoal the shrinking-core model was seen.

Investigations also indicate that elemental Si does not follow a similar shrinking-core model. A collection of EPMA BSE images from varying temperatures using charcoal as the carbon material is shown in Figure 2.14. In these images, the darkest phase is epoxy or pores, the grey phase SiC, and the brightest phase elemental Si. In most cases, the formation of Si does not seem to prefer any specific location on the SiC particles. Images **(a)** and **(b)** could even indicate that Si prefers to concentrate the center of the SiC particle.

One of the more interesting finds of Jayakumari is the discovery of elemental Si in a region where the temperature was measured to be between 1762 to 1783 °C. This is an interesting find as Si is expected to be formed above 1800 °C. However, it is possible that Si could have been transported via fines to the carbon charge, which gives an impression of formed Si. Additionally, as this was a large scale experiment to produce large amounts of β-SiC, there are many other variables which have to be accounted for.

Ramos (2018)[5] studied the quality of three differently carbonized charcoals of the type eucalyptus for use in the Si production process. Before experiments, the charcoal samples were calcined at

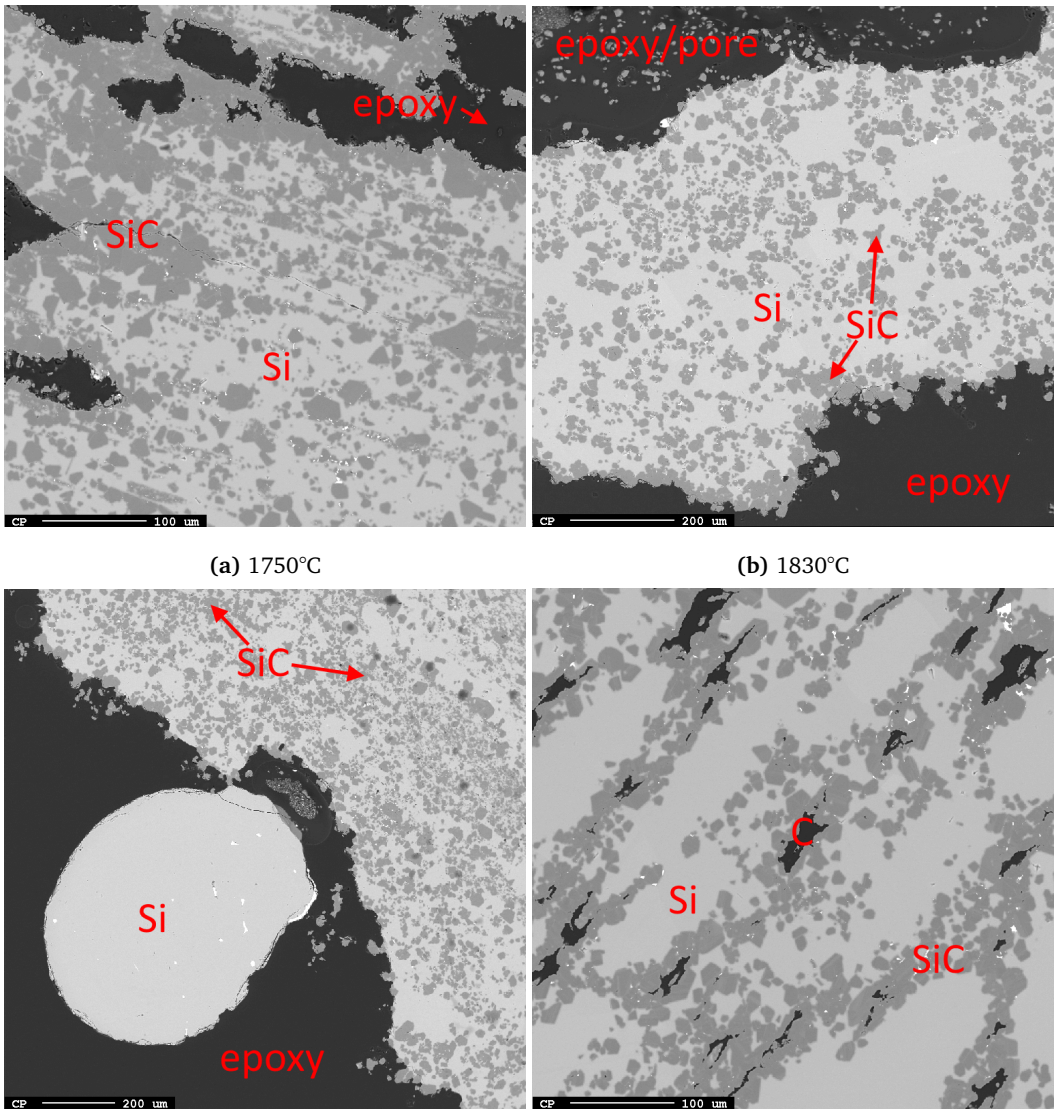

(a) 1750°C **(b)** 1830°C

(c) 1830°C **(d)** 1900°C

Figure 2.14: Jayakumari (2018)[1]. EPMA BSE images of particles collected from a charcoal charge after heat treatment at varying temperatures. The images show the formation of Si in particles of SiC. Elemental Si does not seem to prefer any specific location inside the SiC particles as the bright phase of Si is scattered on almost all the images. One exception, or a concentration of Si, is **(c)** which show the cross section of a droplet of Si on the particle surface.

1200 °C at 20 min to remove volatile matters. Next, the charcoal samples were put through the SiO-reactivity test where samples are exposed to SiO-gas at 1650 °C for 120 min. The percentage of CO in the effluent gas was measured during these experiments. The samples were characterized using SEM both before and after the SiO-reactivity test.

It was concluded by Ramos, that the typical structure of charcoal was preserved after the SiO-reactivity test. However, as pointed out by Ramos, one of the charcoal samples had reduced diameters of the fiber lumen. Lumen refers to the channel within the tubular structure. The deposits, which had resulted in this reduced diameter, is believed to occur from an initial reaction between SiO- and CO-gas to form SiC and SiO_2, followed by a reaction between SiO_2 and C to reproduce SiO- and CO-gas. The remaining species on the surface according to this mechanism would be SiC.

A pilot-scale experiment simulating the Si production process was carried out by Myrhaug (2003)[4]. In this simulation, the amount of charcoal in the carbon charge mixture was varied. Wood chips were added to the top of the furnace. After experiments, the pilot scale furnace was excavated and several locations were chosen for analysis. Wood chips added to the top of the furnace were later found to be all converted to charcoal. At the top of the charge, particles of charcoal were found with a thin green layer of SiC. SEM images of the partially converted charcoal particles also show such a layer of SiC. The structure of wood is still recognizable in the areas of SiC. Condensates from SiO-gas were a common feature on many of the investigated charcoal particles.

Chapter 3

Experimental apparatus, procedures and materials

3.1 Raw materials

In the bottom of the graphite crucible, a mixture of SiO_2 and Si is used to produce SiO-gas. Above this mixture, charcoal was used to capture the ascending SiO-gas. Analysis of the Si, charcoal, and quartz (SiO_2) are located in tables in Figure 3.1. Furthermore, porosity data for the graphite crucibles can be found in Table 3.1.

Table 3.1: Analysis of the porosity of the graphite parts done by Toyo Tanso Co.

Bulk density	**Cumulative pore volume**	**Open porosity**	**Radius of Average Open Porosity**
1.9 Mg/m^3	0.052 m^3/g	10 %	1.4μm

3.2 Furnace

The crucible together with the raw materials is placed inside a graphite resistance furnace to be heated to a target temperature.

The furnace used for all experiments is shown in Figure 3.2. The furnace has a vertical design and consists of graphite resistance heating elements inside a water-cooled cylinder. In addition to a

(a) Chemical analysis of the Si

Product	**Si**	**Fe**	**Ca**	**Ti**	**P**
Elkem	wt%	wt%	wt%	ppmw	ppmw
Si 40 10	Min 99.0	Max 0.40	Max 0.10	200-300	20-40

(b) Analysis of charcoal. All values given in wt%.

Moisture	**FixC**	**FixC**	**Ash**	**Ash**	**Volatiles**	**Volatiles**
-	DB	WB	DB	WB	DB	WB
8.03	90.32	83.07	1.62	1.49	8.05	7.41

(c) Analysis of quartz from 25.07.2015. All values given in wt%.

Fe_2O_3	**SiO_2**	**Al_2O_3**	**CaO**	**TiO_2**	**MgO**	**Na_2O**	**K_2O**	**P_2O_5**
0.0352	99.82	0.1157	0.0058	0.0031	0.0028	0.004	0.0205	0.0014

Figure 3.1: Analysis of the different raw materials used in the experiments. DB and WB is short for Dry Basis and Wet Basis.

pyrometer which controls the furnace temperatures, a C-type thermocouple is added from the top of the furnace and is positioned directly inside the sample crucible, as illustrated in Figure 3.3. The tip of this added thermocouple is placed about 3.5 cm above the crucible bottom, right above the gas-permeable disc. This allows for accurate measurements of temperatures in the area where SiO-gas reacts with carbon materials. The pressure inside the furnace is measured to be around 1.45 bar during the experiments.

3.3 Experimental setup

The crucible is set up as illustrated in Figure 3.3. The crucible outer diameter is 45 mm. The inside of the crucible walls is machined to form a ledge that will act as support for a gas-permeable disc. This disc divides the crucible into a lower zone where SiO-gas can be produced and an upper zone for the capture of ascending SiO-gas. In the center of the crucible, a graphite pipe is placed for the protection of the thermocouple and to lead Ar-gas into the system. The Ar-gas enters the crucible through a couple of small holes in the graphite rod at about 0.1 standard litre per minute. These holes are placed 6 cm from the bottom of the graphite rod, which corresponds to the very upper

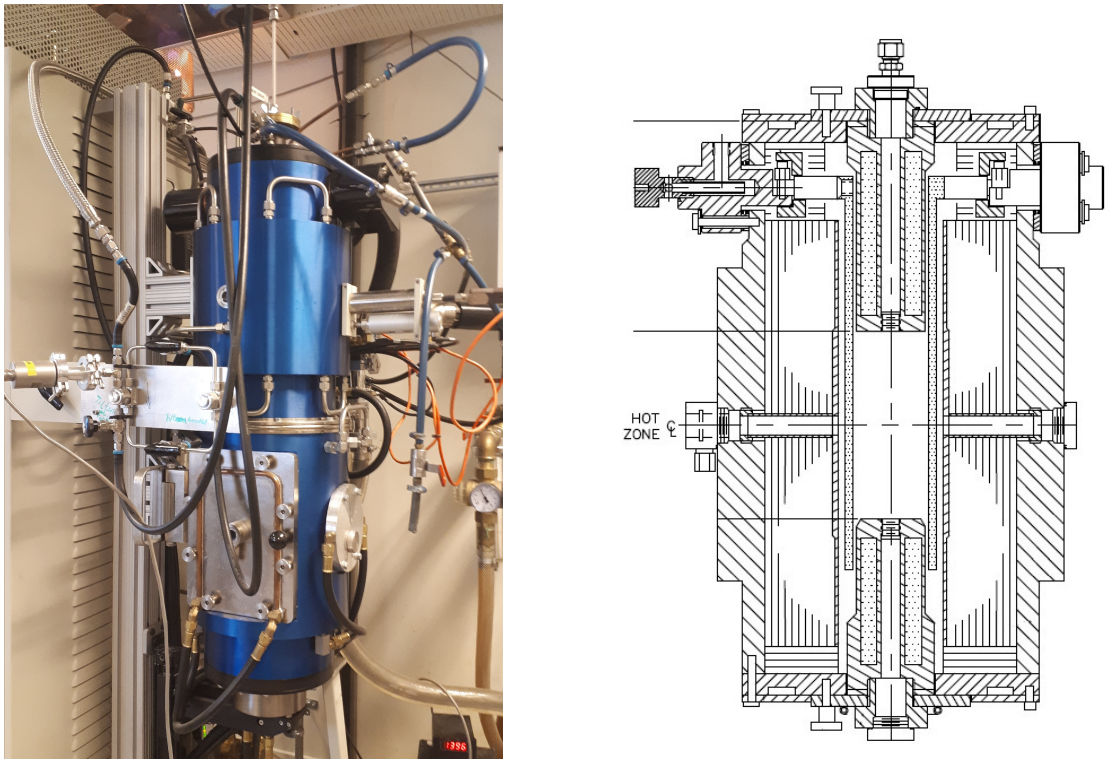

(a) **(b)**

Figure 3.2: A vertical tube furnace was used to reach the target temperatures. A photo is shown in **(a)** and the cross-section in **(b)**.

region of the carbon charge.

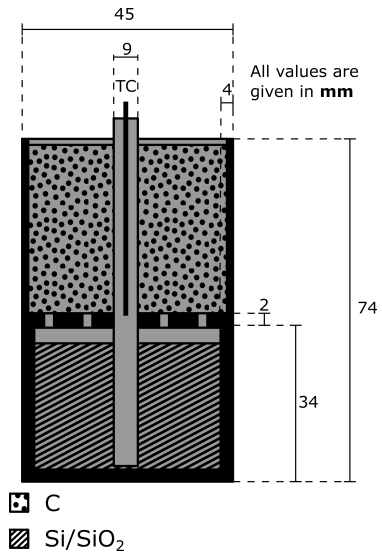

Figure 3.3: Schematic of the graphite crucible with the thermocouple position (noted as TC). All dimensions are given in mm. The crucible is divided into two zones; one for producing and one for the capture of SiO-gas.

Due to furnace design, the bottom graphite pipe had to be extended upwards by an Al_2O_3 pipe. Initially, the graphite and Al_2O_3 pipes were welded together by smearing a paste mixture of powdery Al_2O_3 and water at the contact point between the two pipes. Furthermore, the paste was hardened by heat treating it at 90, 180 and 270 °C with a 2 hour holding time at each temperature. The resulting weld was however too brittle and unstable to be used for further experiments. In the following trials to weld Al_2O_3 and graphite, a proprietary high-temperature adhesive mixture was used. The mixture, which is used by Ph.D. candidate Ødegård[25], was found to have better mechanical properties compared with the mixture of powdery Al_2O_3 and water.

A gas-permeable disc was used to separate the carbon from the Si-containing raw materials. The thickness of this disc is 2 mm and the diameter of the holes is approximately 1.9 mm. For the fitting of the graphite pipe, as seen in the center of the crucible in Figure 3.3, an additional 9 mm diameter hole was made in the center of the gas-permeable disc.

The amount of raw materials added to the crucible for each experiment with the corresponding target temperatures can be seen in Table 3.2. The first test experiment, labeled sample 0, had a conservative amount of Si/SiO_2 added. Consequently, there was a lack of reaction between charcoal and SiO-gas in this sample, and the following experiments were all adjusted to fill the entire volume below the gas-permeable disc with the SiO-producing raw materials.

Table 3.2: Experimental setup with both raw materials added (in grams) and the target temperatures (in °C).

Sample	**T (°C)**	**Si**	**SiO_2**	**Charcoal**
0 (Test)	1800	5.14	10.12	8.94
1	1900	13.65	26.65	8.68
2	1850	13.64	26.67	9.45
3	1800	13.61	26.42	9.99
4	1800	13.41	26.84	9.59
5	1815	13.40	26.78	9.40

Due to furnace difficulties during the experimental period of the work, there were some parameters which were not varied. One of which was to run a few experiments with coal instead of charcoal to investigate the effect of i.e. porosity. Another variable that was planned, but not implemented, is the use of a SiC/SiO_2-mixture instead of SiO_2/Si. The use of SiC and SiO_2 was planned to measure the effect of lower SiO-gas pressures.

3.4 Sample preparation

During the sample preparation, the Si-containing materials, SiO_2 and Si, are sieved to achieve a particle diameter of 2-4.75 mm. Before being added to the crucible, the SiO_2 and Si were mixed. The carbon materials are sieved to 4-4.75 mm particle diameter. This is done to reduce the probability of carbon falling through or blocking the holes of the disc. Additionally, the sieving reduces the amount of Si fines, which could be suspended in gas and subsequently ascend to the carbon materials. Si transported in such a matter could give a false impression that it has been formed in the carbon charge.

The resulting particles in the carbon charge were collected and divided into three groups by colour. They were then prepared for SEM analysis, both with and without the use of iodoform-containing epoxy. The addition of about 10% iodoform to the resin and hardener mix increases the contrast between the epoxy matrix and the carbon particles[26].

3.5 Temperature measurements

The target temperatures were set to investigate the effect of temperature on the charcoal to SiC-conversion and to investigate the lower temperatures of Si-formation. The first two samples, set to 1900 and 1850 °C, was planned to measure the effect of temperature on SiC conversion and eventual Si formation. At such large temperatures, it was certain that SiC and Si would be produced. The next two target temperatures, 1820 and 1800 °C were chosen to investigate the lower temperatures of Si formation. Due to the temperature gradient inside the furnace, the temperature inside the crucible is lower than what is measured outside. With this in mind, 1820 and 1800 °C was chosen to achieve a carbon charge temperature around 1800 and 1780 °C, respectively. The invariant point, and the lower temperature of Si formation is believed to be around 1800 to 1811 °C, depending on the source. Due to furnace difficulties, an additional sample had to be run with a target temperature of 1800 °C.

The temperatures measured by the pyrometer (outside crucible) and thermocouple (inside crucible) are seen in Figure 3.4. There are a few things to point out: First, during the ascent to reach the target temperature, the furnace overshoots the temperature by about 25 °C. Sample 5, which was set to 1815 °C, was run with a heating curve which adjusted for this error. Secondly, some minor temperature spikes occurred in both samples 1 and 2. In addition, sample 3 demonstrates a much larger irregularity as seen by the contradicting values given by the pyrometer and the thermocouple. A large temperature increase is measured by the thermocouple, while a temperature decrease is

measured by the pyrometer. It is believed that the thermocouple measured the correct temperatures and that sample 3 has experienced much larger temperatures than what was planned.

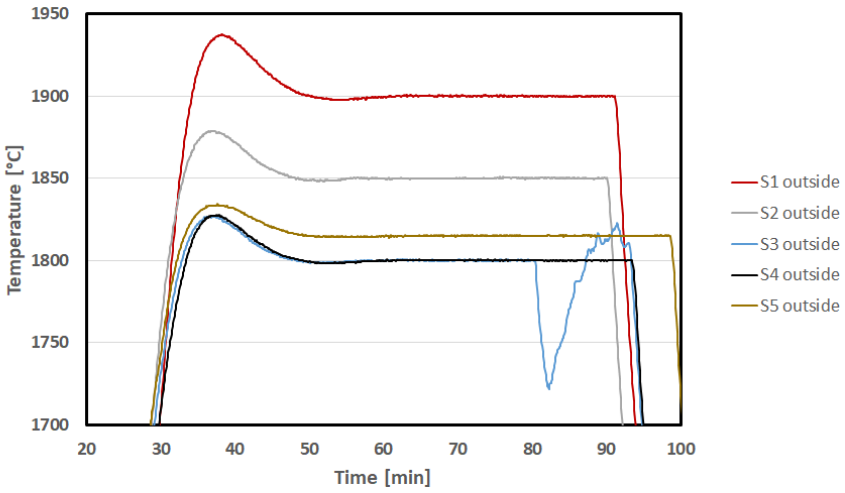

(a) Outside crucible, pyrometer

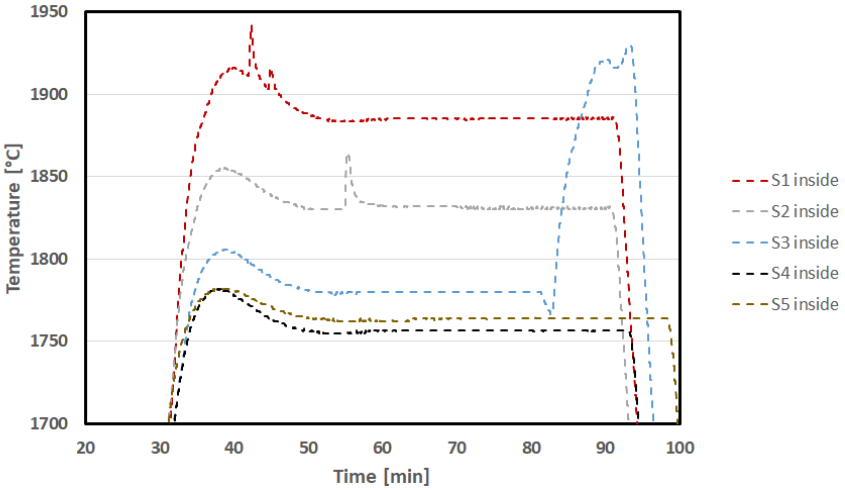

(b) Inside crucible, thermocouple

Figure 3.4: Temperatures measured inside the furnace by both pyrometer and thermocouple is shown in **(a)** and **(b)**, respectively. The outside temperature of sample 0 is not shown in this figure. The added thermocouple measured the temperatures in the center of the crucible, inside the carbon charge, just above the gas-permeable disc. Hence, these temperatures measured by the thermocouple are thought to best represent the system.

As the temperatures measured inside the carbon charge best represent our system, they are presented together with their corresponding samples in Table 3.3. In this table, the maximum and stabilized temperatures of the thermocouple are presented together with their accuracy range. The stabilized temperatures are found at the point where the temperature has reached an equilibrium with the temperature profile of the system, typically after reaching a maximum temperature. The stabilized temperature will often be referred to as just temperature. A C-type thermocouple was used

to measure the temperatures as given in Figure 3.4 **(b)**. The limits of error using a standard C-type thermocouple is, according to manufacturer OMEGA, given as ± 1% up to 2320 °C. This accuracy range is included together with the measured temperatures in Table 3.3.

Table 3.3: The maximum and stabilized temperatures measured by the C-type thermocouple inside the carbon charge. The stabilized temperatures are found at the point where the temperature has reached an equilibrium with the temperature profile of the system, typically after reaching a maximum during heating. These values are accompanied by an accuracy range of ± 1% for C-type thermocouples.

Sample	**Max. Temp. (°C)**	**Stab. Temp. (°C)**
1	1941.8 ± 19.4	1885.6 ± 18.9
2	1855.0 ± 18.6	1831.0 ± 18.3
3	1921.7 ± 19.2	1780.0 ± 17.8
4	1781.8 ± 17.8	1757.8 ± 17.6
5	1781.8 ± 17.8	1763.7 ± 17.6

3.6 Mass balance

The change in mass due to the formation of SiC and evaporation of volatiles and moisture can be estimated using the chemical analysis of charcoal in Table 3.1. Both Dry Basis (DB) and Wet Basis (WB) are used in the calculations for comparison. The amount of volatiles is assumed to evaporate resulting in a mass decrease. Consequently, this mass decrease due to volatiles is 8.05 wt% using DB and 7.41 wt% using WB. Similarly, the evaporation of moisture will result in further mass reduction. Next, it is assumed that all FixC is converted to SiC according to Reaction (1.5). This reaction will use two moles of C to produce one mole of SiC. Combined with the molar mass of 12 and 40 $\frac{g}{mol}$ for C and SiC, it is found that 24 g of C will result in 40 g of SiC. Hence, a 66% mass increase is expected if all FixC is converted to SiC. The amount of ash is assumed to remain throughout the experiment. The combined change of mass is found to be +35.47 wt% for DB and +23.95 wt% for WB.

The weight of particles collected from the carbon charge was weighed both before and after experiments.

3.7 Sample characterization

Any reacted or unreacted charcoal was collected from the carbon charge and divided into groups by colour. Furthermore, the different particle colour types were investigated in SEM both with and

without the use of epoxy. Some of the particles collected from sample 1 were prepared for XRD analysis. Particles from the three different colour groups were pulverized using a wolfram-carbide ring mill at 600 rpm for 1 min. The powders were given a flat surface and prepared for XRD analysis by using a back-loading technique.

A Field Emission Scanning Electronic Microscope (FE-SEM), the Zeiss Ultra 55 LE, was used for sample analysis. A field emission gun is used to eject electrons towards the surface of the sample. Electrons can interact in several ways with the sample atoms and the resulting ejected signals contain different types of information. The Back-Scattered Electrons signal (BSE) occurs from an elastic collision with the electrons in the atoms. Atoms with a larger atomic weight produce a stronger BSE signal and appear brighter in BSE images. This contrast between atoms is used to more easily separate phases with different compositions from each other. On the other hand, the inelastically scattered electrons, known as Secondary Electrons (SE), produce a topography image where height differences are more easily distinguished. Lastly, the excitation of electrons in the sample can produce X-ray signals. This type of signal contains information about the chemical element and can be used for qualitative analysis in what is called Energy-Dispersive X-ray Spectroscopy (EDS).

One important limitation using the SEM is the penetration depth of different signals. Compared with SE, the BSE has a larger penetration depth beneath the sample surface. In other words, the BSE signal which is used to create the image will also contain information about the composition beneath the surface. A larger acceleration voltage of electrons will also increase this penetration depth. Nevertheless, as the BSE penetration depth for steel is both measured and simulated to be less than 100 nm[27], it is probably safe to assume that BSE penetration depth for other materials will be less than 2 μm. X-ray signals, which are used for EDS analysis, derive from a larger volume compared with BSE signals. Using Castaing's formula[28], the X-ray penetration depth can be estimated to be around 3.66 μm for C (density of charcoal) and 1.5 μm for Si, both at 10 kV. Consequently, EDS analysis of charcoal particles smaller than 5 μm should be avoided.

For X-ray Diffraction (XRD) analysis, a D8 A25 DaVinci X-ray Diffractometer with a LynxEye Super-Speed Detector was used. In XRD a beam of X-ray signal hits the sample surface at varying angles and the diffracted beam angle and intensity is measured. The measured angles and corresponding signal intensities give information about the density of electrons within the sample crystal. In other words, the XRD can be used to identify different phases in the sample. This analysis technique will mainly be used to identify which phase of SiC is present in the sample. In addition, the qualitative amounts of each phase such as SiC vs. Si can be found using the TOPAS software. It should be noted that TOPAS investigates the amounts of each phase it is told to look for and compares them relatively. With this in mind, the values given by the TOPAS does not always represent reality, which is especially true for particles containing carbon, as carbon was overlooked in this XRD-analysis.

Chapter 4

Results

4.1 Visual observations

After each experiment, the lower sections of the crucibles were cut to produce a cross-section. This was done to investigate the consumption of the two SiO-producing reactants, SiO_2 and Si. The resulting cross-sections can be seen in Figure 4.1. Included to the sample numbers are the corresponding stabilized temperatures as measured by the thermocouple inside the carbon charge. All samples have a substantially large remaining bulk of the two SiO-producing reactants, SiO_2 and Si.

The initial test experiment, labeled sample 0, produced results indicating that more SiO-producing raw materials should be added. The experiment was held at 1 hour at 1800 °C without an external thermocouple. After the sample had been collected from the furnace, it was discovered that practically none the charcoal had reacted with SiO-gas. Visually, no condensates could be found, and almost no SiC was found to be formed on the charcoal. Due to lesser amounts of SiO-producing raw materials added to the crucible bottom, there was a substantial empty volume between the Si/SiO_2-mixture and the gas-permeable disc above, before the experiment. Consequently, all other samples were filled to the brim with SiO_2 and Si to increase the production of SiO-gas.

As visually seen from Figure 4.1, it is difficult to see any correlation between temperature and the consumption of SiO_2 and Si. Since sample 0 had a lower initial mass of the SiO-producing mixture, this sample is not comparable with the other five samples. Sample 1 has less remaining mixture of raw materials and has been exposed to the highest temperatures. This is a small indication that the reaction rate between SiO_2 and Si increases with temperature.

There are some observations concerning the crucible itself. First of all, large cracks were observed

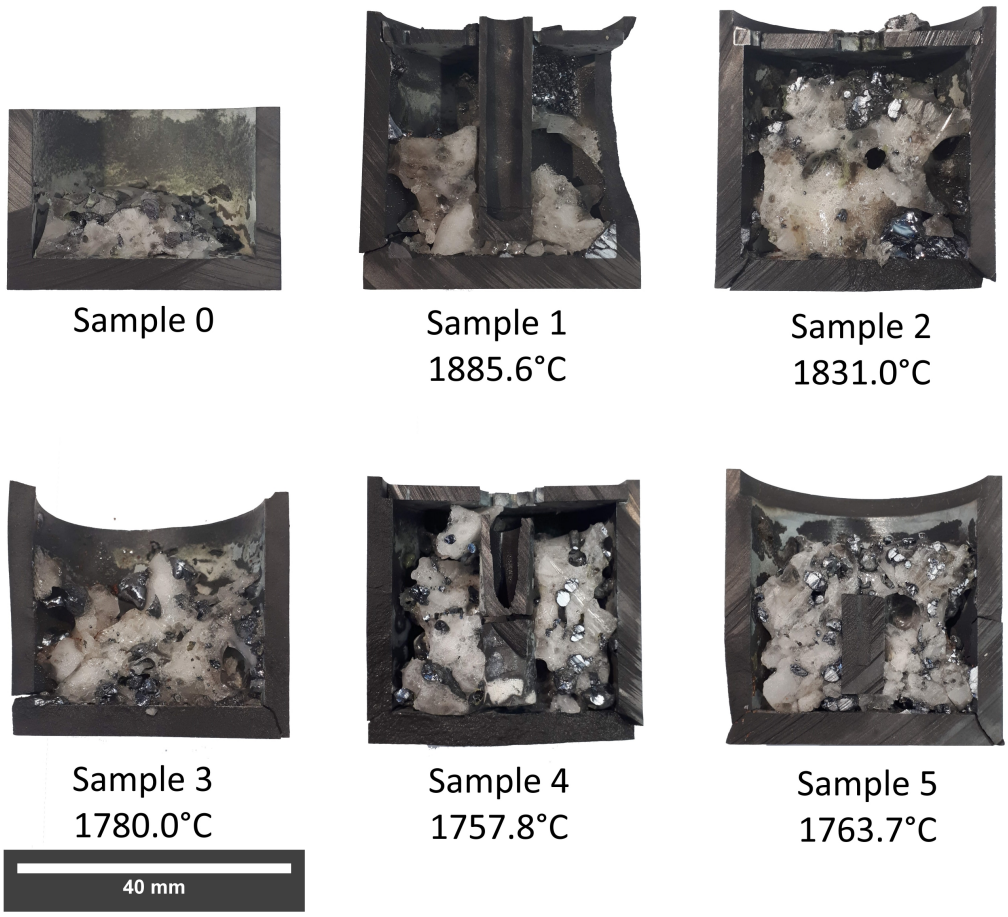

Figure 4.1: Cross-sections of the lower sections of the crucibles, where the two reactants SiO_2 and Si were added to form SiO-gas. The corresponding temperatures are the stabilized temperatures as measured in the carbon charge above this section. Note that the temperature inside the carbon charge of sample 0 was not measured. Additionally, there were less raw materials added to sample 0. In all samples, substantial amounts of SiO_2 and Si were found remaining inside the crucibles. If sample 0 is excluded, there are rough indications that samples exposed to larger temperatures have less remaining mass of SiO_2 and Si.

on the crucible walls after the experiments. In spite of this, no leak of SiO_2 or Si was observed along these cracks or in the crucible holder. These cracks are believed to have occurred during the final cooling and solidification due to the expansion of Si. The weld which connected the graphite purging end to an alumina rod was also covered with cracks. Hence, it is probable that some Ar-gas has leaked through the weld just above the crucible. Secondly, a green or white coloured substance was found covering the walls of the crucibles and on the gas-permeable disc.

Particles were collected from the carbon charge of each sample and were divided into three groups according to colour (see Figure 4.2). The colour of each particle is not always uniform and a few

particles were discovered to have all three colour types on the same surface. Typically, the black particle type was found furthest away from the SiO-producing mixture, in the upper region of the carbon charge. Yellow-green particles were found in the center of the carbon charge, often close to the gas permeable disc. The grey-blue particles were only found at the bottom of the carbon charge, directly above the gas-permeable disc. On some occasions, these grey-blue particles were attached to the gas-permeable disc and had to be extracted using some mechanical force.

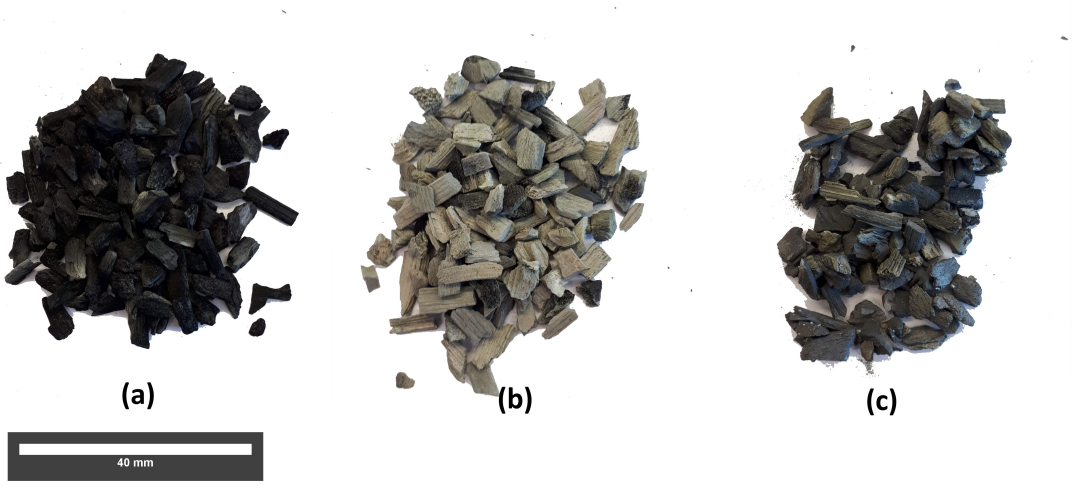

Figure 4.2: (S1 - 1885.6 °C): Particles collected from carbon charge of samples are divided into groups according to colour. The groups are, from left to right in the image, **(a)** black, **(b)** yellow-green and **(c)** grey-blue. Si can be seen formed on many of the particles in the grey-blue group.

Naturally, as SiC was expected to be formed by the reaction between C and SiO, it is believed that the change of colour derives from the formed SiC. The black particles **(a)** is probably unreacted charcoal while the grey-blue particles **(c)** is mostly SiC. An additional group of yellow-green coloured particles **(b)** can also be easily distinguished. Compared with the two other particle types, the yellow-green type has the lowest mechanical stability and leaves powder on any surface it touches. On the contrary, the grey-blue particles seem to have stronger mechanical properties. On the surface of these grey-blue particles, many small droplets or particles of Si could be seen.

Visually, almost no condensates, or the formation of a crust, could be found, in any of the samples. However, a few of the particles from the grey-blue type were sometimes found "glued" together, indicating that some condensation reaction may have occurred. These particles were found at the bottom of the carbon charge, close to the graphite gas-permeable disc. Sometimes, these grey-blue particles were glued to the gas-permeable disc.

4.2 Mass balance

The different groups of particles from Figure 4.2 was weighed and compared to see the effect of temperature. Table 4.1 shows the mass of the different particle types for each sample. As these particles were sorted visually, the resulting measured mass comes with large uncertainties. Consequently, the values should only be used for qualitative comparison between each other. However, the total mass, which is simply the sum of the weight of the three particle types, can be used for quantitative purposes.

The change of mass, **ΔMass**, is calculated using the difference in measured weight of charcoal in Table 3.2 and the total mass in Table 4.1. The resulting column, labeled **ΔMass**, show an increase in the carbon charge mass as the temperature increase. Samples 3 and 4 were both set to 1800 °C, but as previously explained, sample 3 briefly experienced temperatures exceeding 1900 °C due to technical problems. This explains the different results of samples 3 and 4 in Table 4.1. Peculiarly, the measured mass of particles collected from the carbon charge mixture of samples 4 and 5 is significantly lower than what was put in. In other words, the mass balance of samples 4 and 5 has a negative output.

Table 4.1: Measured mass (gram) of particles of each colour type after the experiments. The total sum of these three groups is included in the **Total Mass** column. For comparison with the initially added charcoal, the change of mass **ΔMass** is included as both mass and percentage. Both mass and percentage is relative to the original mass of the added charcoal. *Note that sample 3 experienced temperatures as large as 1920 °C for a few minutes due to a furnace error.

Sample	**Stabilized Temperature**	**Black**	**Yellow-Green**	**Grey-Blue**	**Total Mass**	**ΔMass**	**ΔMass**
Number	*°C*	*grams*	*grams*	*grams*	*grams*	*grams*	*wt%*
1	1885,6	2.81	3.74	5.73	12.28	+3.60	+41%
2	1833,0	5.22	1.95	4.44	11.61	+2.16	+22%
3	1780,0	5.76	1.35	3.35	10.46	+0.47	+5%
4	1757,8	7.47	0.39	0.02	7.88	-1.71	-18%
5	1763,7	6.97	1.13	0.08	8.18	-1.22	-13%

This change of mass, when plotted against temperature, shows a linear trend as the temperature increase or decrease. From Figure 4.1, the mass change of the carbon charge of all samples can be seen. This mass change is given in percentage relative to the original mass before the experiments (**ΔMass**). This mass increase or decrease is seen to follow a linear trend, with a small exception of the red dot. This dot, which is sample 3, is marked red due to furnace difficulties leading to higher

temperatures than planned. This is believed to be the reason for why this red outlier does not follow the linear trend similar to the other four samples.

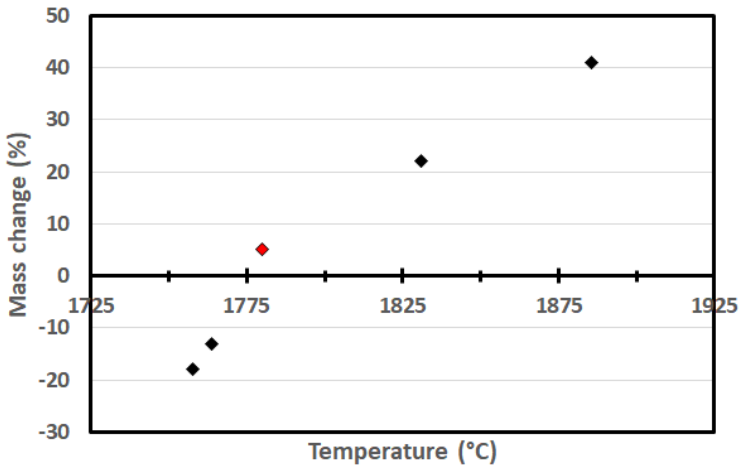

Figure 4.3: Mass change (wt%) of the charcoal particles relative to their original mass before the experiment. The mass change is plotted against the temperatures as measured by the thermocouple. With the exception of a red colored outlier (sample 3), which can be explained by furnace difficulties and increased temperatures, the mass change follows a linear trend.

4.3 SEM

In this section, the results from the SEM analysis will be presented. The **topography** of the particles will be presented first, followed by an investigation of their **inner pore structure**. The topography and the inner pore structure are presented in this order due to an interesting similarity, the presence of crystals both on surfaces and inside pores. Next, a **phase analysis** of the different particle types will be given. Here, the different particle types will be investigated using mainly BSE imaging and EDS analysis. Lastly, the **morphology** of the different phases and the crystals are highlighted. The shortened sample number followed by the measured temperatures are included in the captions of all SEM images.

4.3.1 Topography

The topography of the black, yellow-green, and grey-blue particle types (as seen in Figure 4.2) was investigated using Secondary Electron (SE) imaging. As a reference, charcoal particles were investigated in a similar matter. These particles as presented in the topography section were not cast in epoxy.

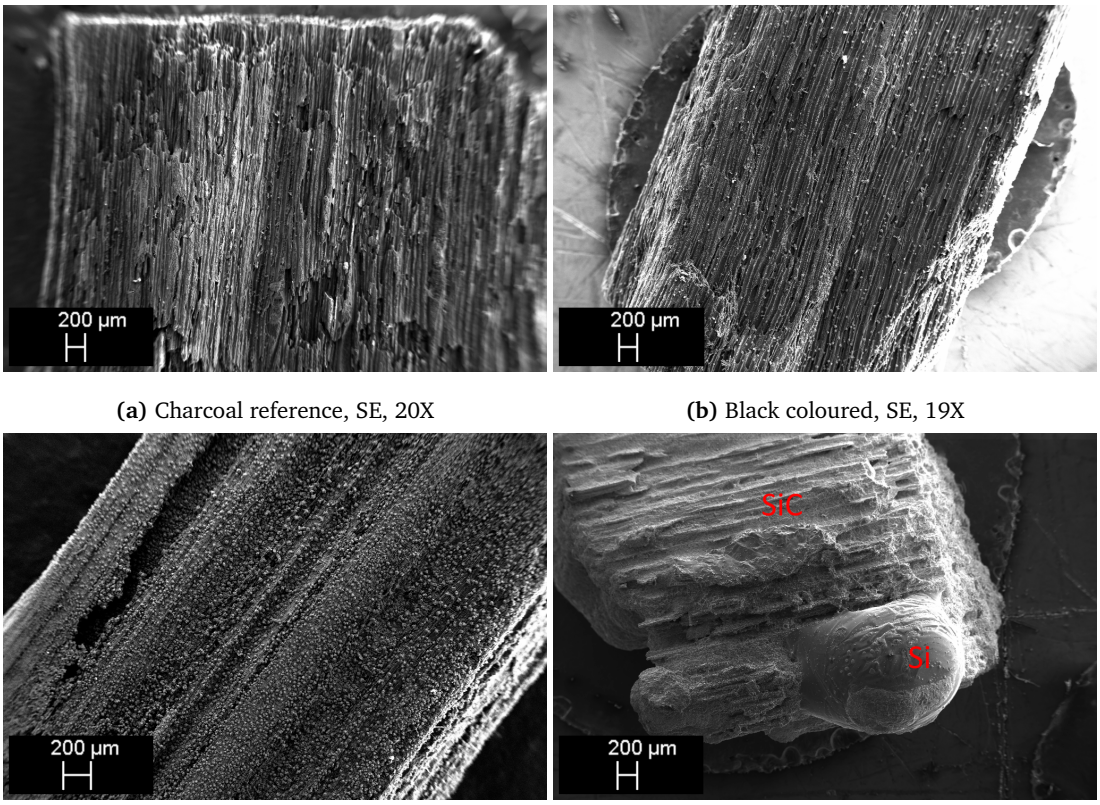

(a) Charcoal reference, SE, 20X

(b) Black coloured, SE, 19X

(c) Yellow-green coloured, SE, 29X

(d) Grey-blue coloured, SE, 21X

Figure 4.4: (S1 - 1885.7°C): SE images of the different particle types collected from the carbon charge, **(b)-(d)**, in comparison with a reference non-heat-treated charcoal particle, **(a)**. These particles are not casted in epoxy. The fibrous structure of charcoal is somewhat visible in all particles. A large droplet of Si is visible on the grey-blue particle.

Low magnified images of charcoal compared with the three different particle types (black, yellow-green and grey-blue) are shown in Figure 4.4. The four images have a similar magnification at 20-30X. Compared with the charcoal reference particle, the black, yellow-green, and grey-blue coloured particles have a similar fibrous structure. However, the topography of all these particles depends very much on the direction of the fibers. Fibers oriented parallel with the image plane will result in a different topography compared to perpendicularly oriented fibers. A droplet of Si can be seen on the surface of the grey-blue particle in **(d)**.

Higher magnified images of the same particles reveal the growth of smaller particles on the surface. The different particle types were also investigated at higher magnifications and the results are seen in Figure 4.5. A reference charcoal particle, **(a)**, was also investigated for comparison with the particles collected from sample 1, **(b) - (d)**. From **(a)** to **(c)** an increasing amount of smaller SiC crystal growth on the surface can be seen. These SiC crystals appear to increase in size from black to yellow-green. In the SE image of the grey-blue particle type, **(d)**, it becomes more difficult to distinguish the crystals from the underlying surface, implying that the entire particle surface has reacted.

Several SE images, which highlights the topography of a grey-blue particle type, can be seen in Figure 4.6. Contrary to the black and yellow-green particle, the grey-blue surface has a faceted morphology similar to the crystals. This faceted topography, which makes the surface look rougher, is shown in both images **(b)** and **(c)**. Consequently, as seen in image **(c)**, it is difficult to effectively separate crystals from the particle surface. Still, the original fibrous structure of charcoal is somewhat visible in both images **(a)** and **(b)**. It was common to find droplets of elemental Si on the surface of grey-blue particles. One such droplet of Si is visible in the bottom right corner of image **(a)** and its smooth non-faceted surface is depicted in **(d)**.

An EDS was performed on the crystals in comparison on the surfaces which they had grown (Figure 4.7). This EDS analysis was performed on all three different particle types (black, yellow-green and grey-blue), however, only the black and yellow-green particle types are included in the figure (The EDS of the grey-blue particle is included in Appendix A). As this EDS was done on a non-flat surface, the resulting calculated compositions are even more uncertain. Hence, EDS spot 6 gives indications of elemental Si, which seems unlikely.

The resulting EDS analysis of all three different particle types shows that these crystals growths are SiC. The conclusion is based on two main observations: the significant presence of silicon and the absence of oxygen. Consequently, SiO_2 can be ruled out and the one remaining silicon-containing crystalline phase in the system is SiC.

The surface, directly next to the where the crystals have been adsorbed, is identified to be C for the black particle types, and SiC for yellow-green and grey-blue particle types. The surface composition

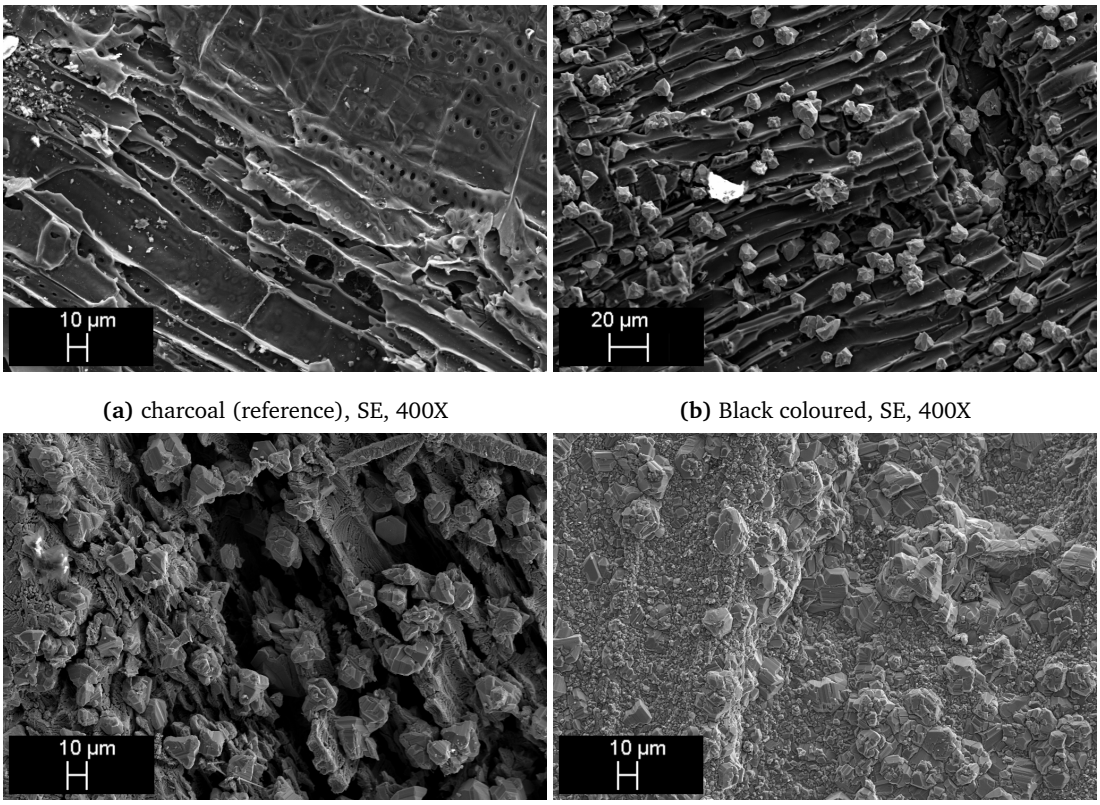

(a) charcoal (reference), SE, 400X

(b) Black coloured, SE, 400X

(c) Yellow-green coloured, SE, 400X

(d) Grey-blue coloured, SE, 400X

Figure 4.5: (S1 - 1885.7°C): 400X SE images of the different particle types collected from the carbon charge, **(b)-(d)**, in comparison with a reference non-heat-treated charcoal particle, **(a)**. These particles are not casted in epoxy. An increasing size of crystals on the particle surfaces is observed from **(b)** to **(c)**. The grey-blue particle surface is more rough/faceted compared with the other particle types.

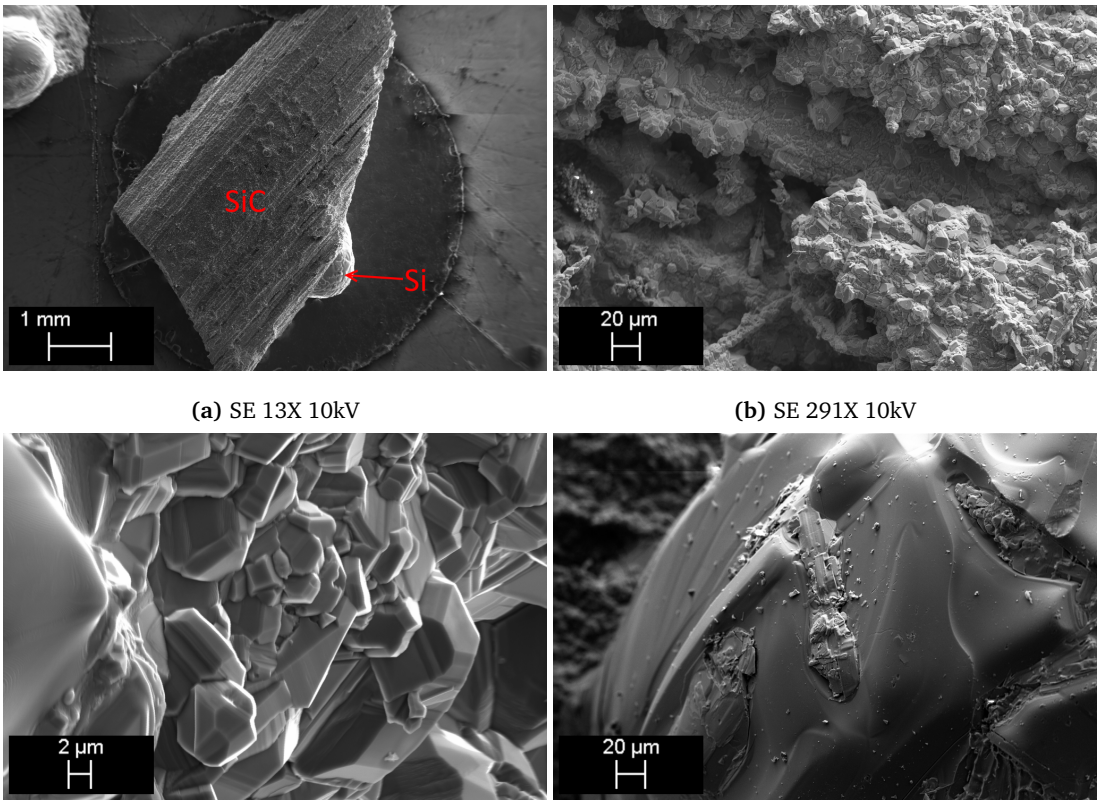

(a) SE 13X 10kV

(b) SE 291X 10kV

(c) SE 2350X 10kV

(d) SE 303X 10kV

Figure 4.6: (S1 - 1885.7°C): Four topography images of a grey-blue particle. **(a)** shows the overview of the entire particle where a large Si droplet can be seen. **(b)** and **(c)** depicts the faceted (rough) surface of the particle. **(c)** depicts the smooth surface of the Si droplet found on this grey-blue particle.

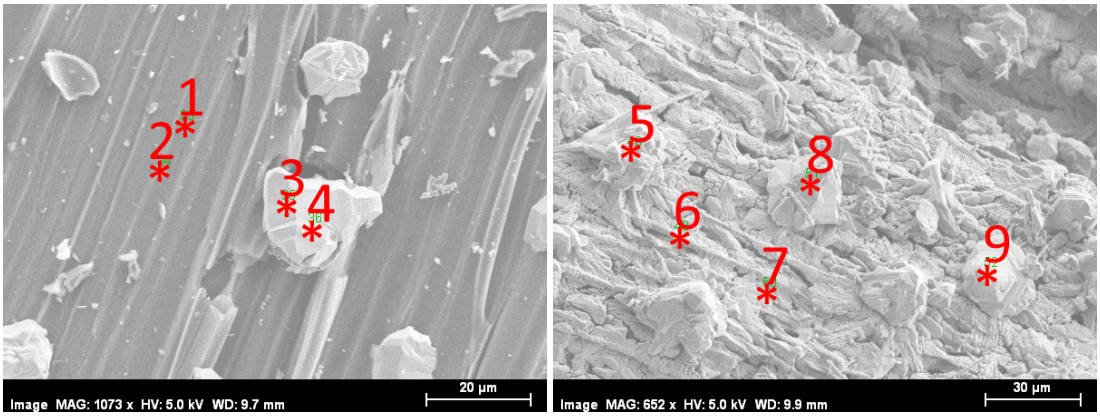

(a) Black particle **(b)** Yellow-green particle

Spot	C (at%)	O (at%)	Si (at%)
1	99.27	0.73	-
2	100	-	-
3	50.01	-	49.99
4	50.96	0.97	48.06
5	49.54	-	50.46
6	11.60	-	88.40
7	39.14	-	60.86
8	40.03	-	59.97
9	48.60	-	51.40

(c)

Figure 4.7: (S3 - 1780.0°C): Images **(a)** and **(b)** show the crystal spots where EDS analysis was performed on the black and yellow-green particles. The results are shown in **(c)** where the values are given in atomic percentage (%). The crystals are identified to be SiC. The surface next to these crystals are identified to be C for the black particles type, and SiC for the yellow-green and grey-blue particle types. The surface of the black particles also sometimes gave peaks indicating the presence of Na, Cl, K and Ca.

directly beneath each crystal growth is still not certain. Although not included in this table, it should be mentioned that lesser amounts of Na, Cl, K and Ca were also sometimes detected. It was mostly found on the surface of the black particle type along with C, but was also detectable on a grown crystal on the grey-blue particle surface.

No correlation was found between temperature and the morphology, size or amount of these crystals.

4.3.2 Interior pore structure

In this section, the results regarding the pore structure of the different particles will be presented. First, the charcoal structure will be investigated, followed by the structures of the black, yellow-green, and grey-blue particles. These particles were cast in epoxy.

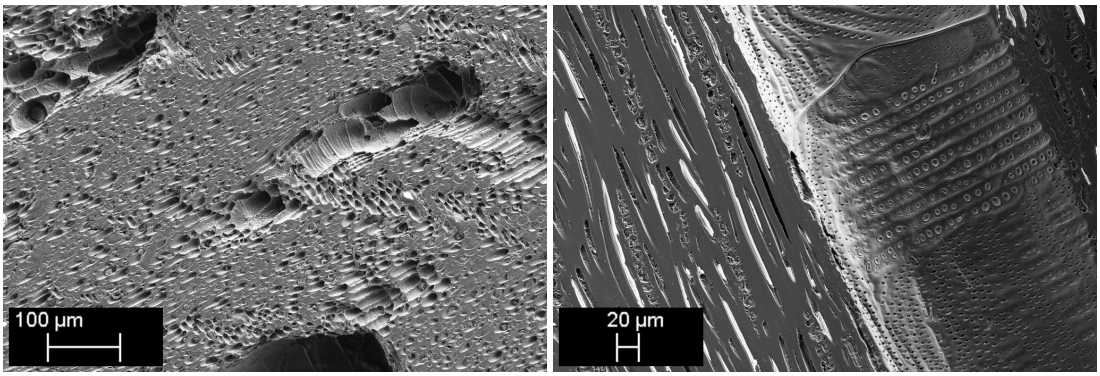

(a) SE 152X 5kV **(b)** SE 230X 5kV

Figure 4.8: The interior structure of two charcoal particles. Image **(a)** show the two different size groups of the fibrous pores, small and large. This particular charcoal particle is cut somewhere between longitudinal and transverse sections. The more magnified image **(b)** also show the smaller pores in comparison with a larger one. The larger pore, which covers large portions of the image, also show indications of a cellular structure.

In general, the structure of charcoal is difficult, if not impossible, to predict. As previously mentioned, the resulting charcoal structure depends very much on the fiber direction relative to the image plane. A cross-section following the longitudinal direction, which is along the longest axis, will give a different structure compared to structure from a transverse section. Similarly, the cross-section of longitudinal and transverse sections of a tree trunk will look completely different. Furthermore, it is often found that one charcoal particle exhibits more than one direction of fibers. To make matters more complex, in addition to the directional variable, the structure of charcoal also depends on many other features such as the fiber size, diameter, and numbers. Accompanied by the different ash content of charcoal particles, it is not difficult to see that the structure of charcoal is unpredictable.

Anyhow, the lengths and diameters of these fibrous pores were quickly measured to give a rough estimate. It was possible to divide the investigated pores into small and large, depending on the diameter. Varying numbers of smaller pores were always found inside the investigated charcoal particles. The diameter of these pores is found to be between 1 and 15 μm. The length of the smaller pores is not always that easy to measure as they sometimes disappear into the charcoal bulk. However, some of the longest fibrous pores were measured to be up to 250 μm long. Larger pores, which had a typical size of 100 and 250 μm diameter, were also sometimes found. Some charcoal

particles had no such large pores, while others had many. Similar to the smaller pores, the length of the larger pores is also difficult to measure as they often disappear into the bulk. Still, some of them managed to stretch to a few mm in size. In Figure 4.8 these two different pore sizes can be seen.

Whilst investigating the grey-blue particles, it was found that during the conversion from charcoal to SiC, some changes regarding the pore structure could occur. As discussed more thoroughly below, the amount of smaller pores in the 1-15 μm diameter range was lacking in many, although not all, of the investigated grey-blue particles. However, the same grey-blue particles was often found with an abundance of larger pores with 25-100 μm diameters. It is emphasized that there are large variations between the investigated particles, which is believed to be caused by the unpredictable structure of charcoal. Still, the lack of pores inside any particle converted from charcoal is peculiar and indicate to a structural transformation.

First of all, from the investigation of both areas of SiC and areas containing unreacted charcoal surrounded by SiC, it was found that the smaller 1-15 μm diameter pores are sometimes removed as charcoal converts to SiC. Images **(a)** and **(b)** in Figure 4.9 depict areas of unreacted charcoal inside grey-blue particles collected from samples 1 and 2, respectively. The darkest coloured areas are unreacted charcoal, while a more brightly coloured SiC surrounds the charcoal. In image **(b)** some white coloured epoxy can also be seen. From these two images, it is possible to see a large contrast between the structures of charcoal and SiC. The carbon area contains many smaller 1-15 μm diameter pores, which is similar to the smaller pores found in the charcoal reference particle. However, similar small pores are lacking in the grey coloured areas containing SiC. The final image, **(c)**, is inside another grey-blue particle collected from sample 4. Here, inside an area of only SiC, these smaller pores are to some degree preserved around a bulk. It is possible that this bulk once contained pores, which have been removed during the conversion from charcoal to SiC.

Secondly, a few of the investigated grey-blue particles were found with an abundance of large pores. To the right in image **(a)**, Figure 4.9, several larger 25-100 μm pores are visible inside an area of SiC. Similarly, in image **(a)**, Figure 4.10, another grey-blue particle where the center is covered with such large pores is shown. The large pores in this figure have diameters between 30 and 300 μm. However, the most peculiar attribute of these particles shown in Figure 4.10 is not just the abundance of large pores, but the lack of smaller pores in addition. It is an indication that large pores are unaffected as charcoal is converted to SiC.

Despite the structural changes, as discussed above, it is specified that some of the particles were converted to SiC without any significant structural changes. One such particle is shown in image **(b)** of Figure 4.10. Many smaller pores originating from the original charcoal structure is well visible.

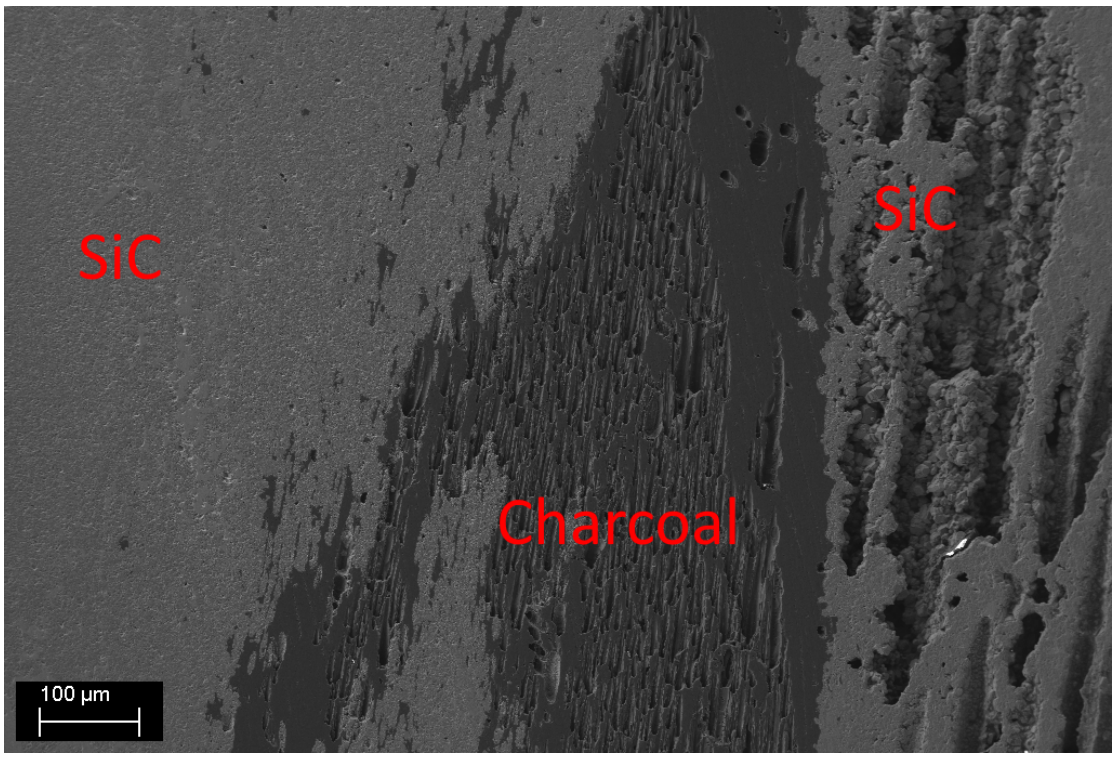

(a) (S1 - 1885.7°C): SE 102X 5kV

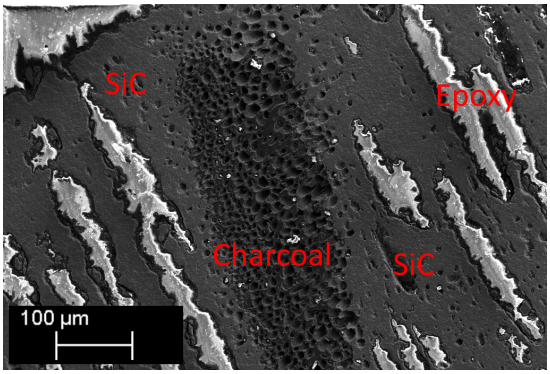

(b) (S2 - 1831.0°C): SE 158X 5kV

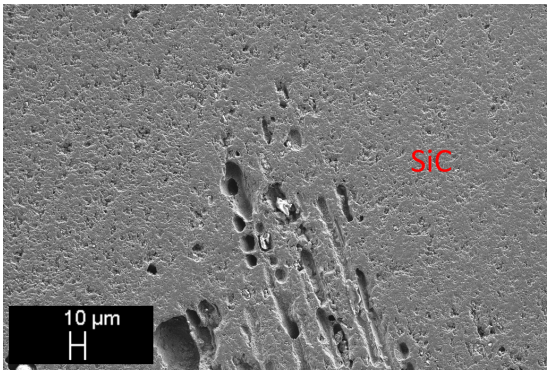

(c) (S4 - 1757.8°C): SE 311X 5kV

Figure 4.9: Various images showing a structural transformation of charcoal as it converts to SiC. Image **(a)**, **(b)**, and **(c)** is from samples 1, 2 and 4, respectively. In images **(a)** and **(b)**, a dark coloured charcoal is surrounded by a more brightly coloured SiC. In image **(b)**, there is also a presence of white coloured epoxy. In these two images, there is a structural contrast between charcoal and SiC since the charcoal contains large amounts of smaller pores which are lacking in the surrounding SiC. A collection of large pores is also shown to the right in image **(a)**. In the final image, **(c)**, a number of smaller pores are shown surrounded by a bulk of SiC. It is possible that the bulk also contained such smaller pores, which has been removed during the convertion from charcoal to SiC.

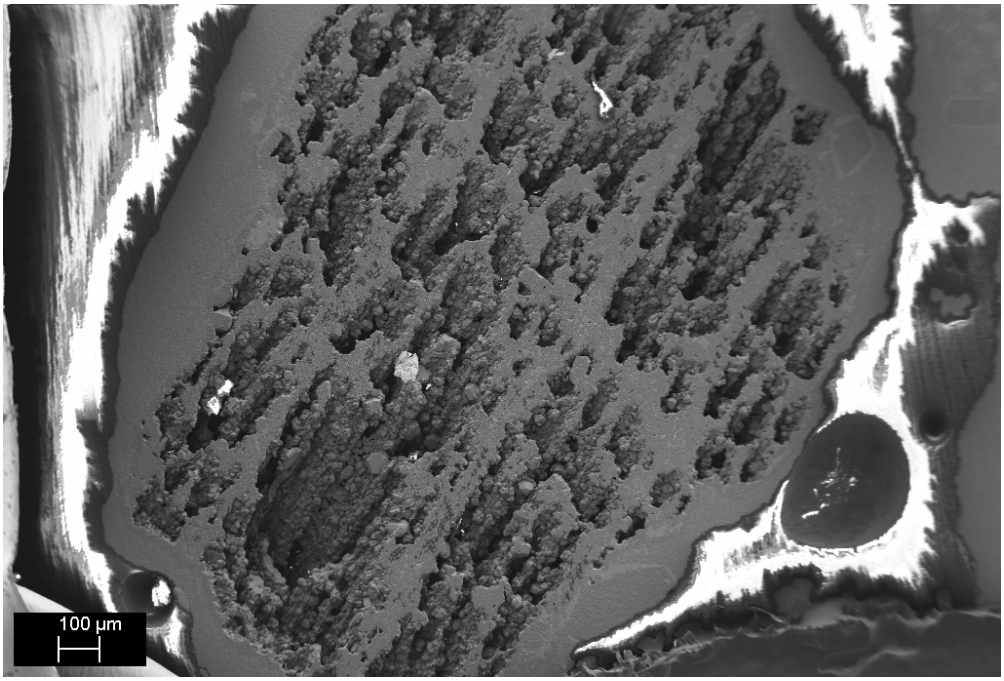

(a) (S1 - 1885.7°C): SE 55X 5kV

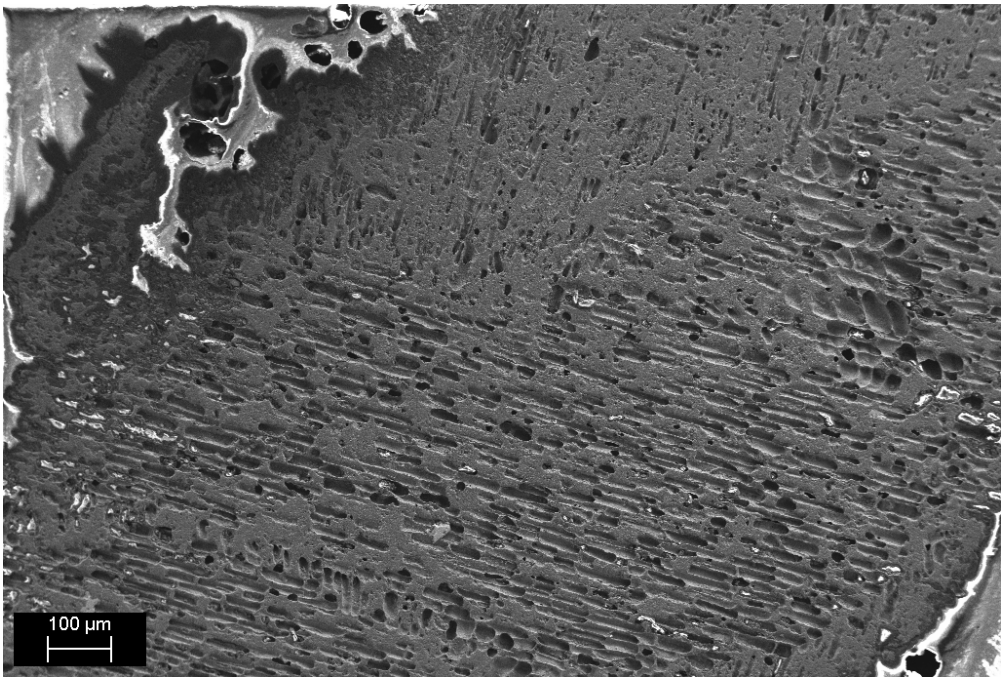

(b) (S4 - 1757.8°C): SE 73X 5kV

Figure 4.10: A varying degree of structural change was often, but not always, observed in the converted charcoal particles. Shown in the two images are grey-blue particles collected from samples 1 and 4. Some converted particles, such as the one shown in image **(a)**, were found without any small pores, while other were found with many, image **(b)**. The large pores in image **(a)** have a size from 30 and 300 μm in diameter.

There are faint indications that particles exposed to larger temperatures have undergone larger structural changes. Sample 1 (1885.7°C) were found with many of the structural changes as discussed above, while samples 4 and 5 (1757.8 and 1763.7 °C) were found with little or none. This difference in structural changes is also shown in Figure 4.10. However, due to the natural structural variety of charcoal and the small number of grey-blue particles collected from samples 4 and 5, the effect of temperature on structural changes is difficult to conclude.

Similar to what was found on the particle surfaces, the internal pore surfaces was in many occasions covered with faceted SiC crystals. The crystals were found to be present in both small and large pores in various sizes. Some of the largest crystals inside the pores had grown to 4-15 μm in diameter. For comparison, the largest crystals found on the particle surface was between 10-30 μm. This find of pore crystals suggest that pores are removed as these crystals grow larger. The morphology and shape of these crystals will be presented later.

One of the smaller pores located in a region of charcoal is seen imaged in Figure 4.11. The internal surface of these pores can be seen covered with very small crystals. BSE imaging, as seen in image **(b)**, revealed these more brightly coloured crystals to be composed of larger atoms than the surrounding carbon phase. Hence, it is most probable that these crystals are composed of SiC. This BSE image also reveals that these crystals have grown directly on a carbon surface.

4.3.3 Phase analysis

In addition to the investigation of topography and the interior pore structure, the different particle types were also analyzed to identify the phases present. It is specified that these samples have been cast in an iodoform-containing epoxy and was ground down and polished to achieve a flat surface. Below are the comparable results from the different particle types: black, yellow-green, and grey-blue.

The black particle type was found to contain mostly unreacted charcoal, with varying amounts of SiC present in the shape of a uniform layer or scattered crystals. Many of the black particles were identified to be unreacted charcoal with no traces of SiC. Still, SiC was found in some of the black particles in the form of small crystals or/and as a large uniform layer. Both of these two SiC forms, which were found inside black particles collected from samples 1 and 4, are shown in Figure 4.12. Layers of SiC were most often found covering the particle surface or the surface of an internal pore. The structure of this layer looks similar to folded sheets of paper. EDS analysis of this layer can be found in Appendix A. Crystals of SiC were sometimes found evenly scattered inside the particle. It is emphasized that the presence of SiC is overshadowed by the massive amounts of unreacted charcoal

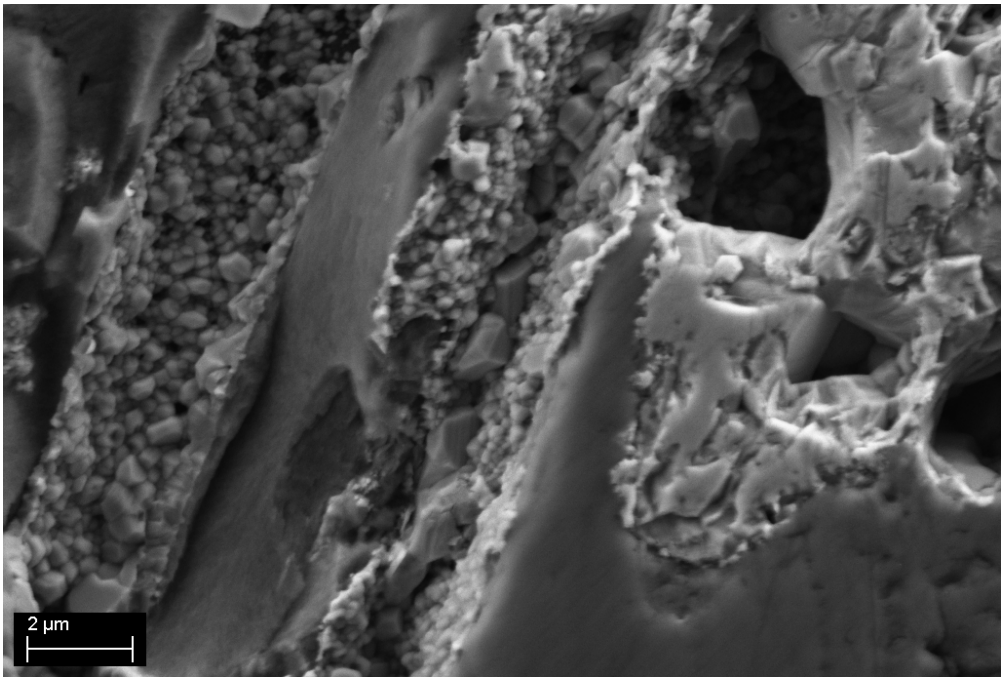

(a) SE 6040X 5kV

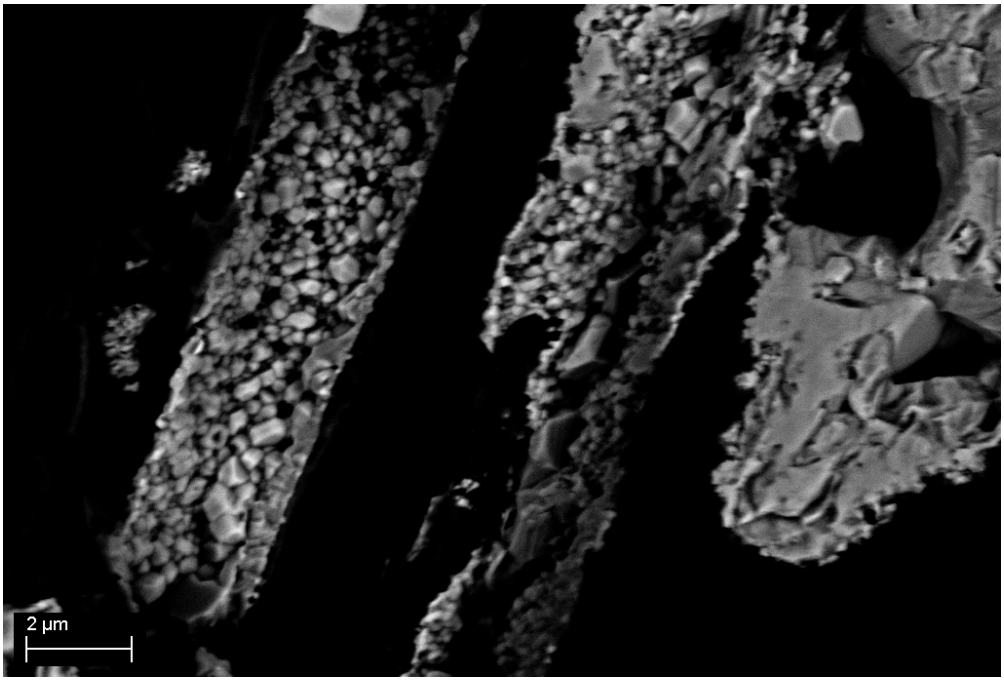

(b) BSE 6040X 5kV

Figure 4.11: A highly magnified image of the smaller pores, as found inside an area of carbon, is provided with both SE and BSE in **(a)** and **(b)**, respectively. Many crystals of SiC, which is brightly coloured in image **(b)**, are discovered inside the pores of an area of unreacted charcoal. It seems most probable that the further growth of these crystals can clog and remove the pores.

found in the black particle types.

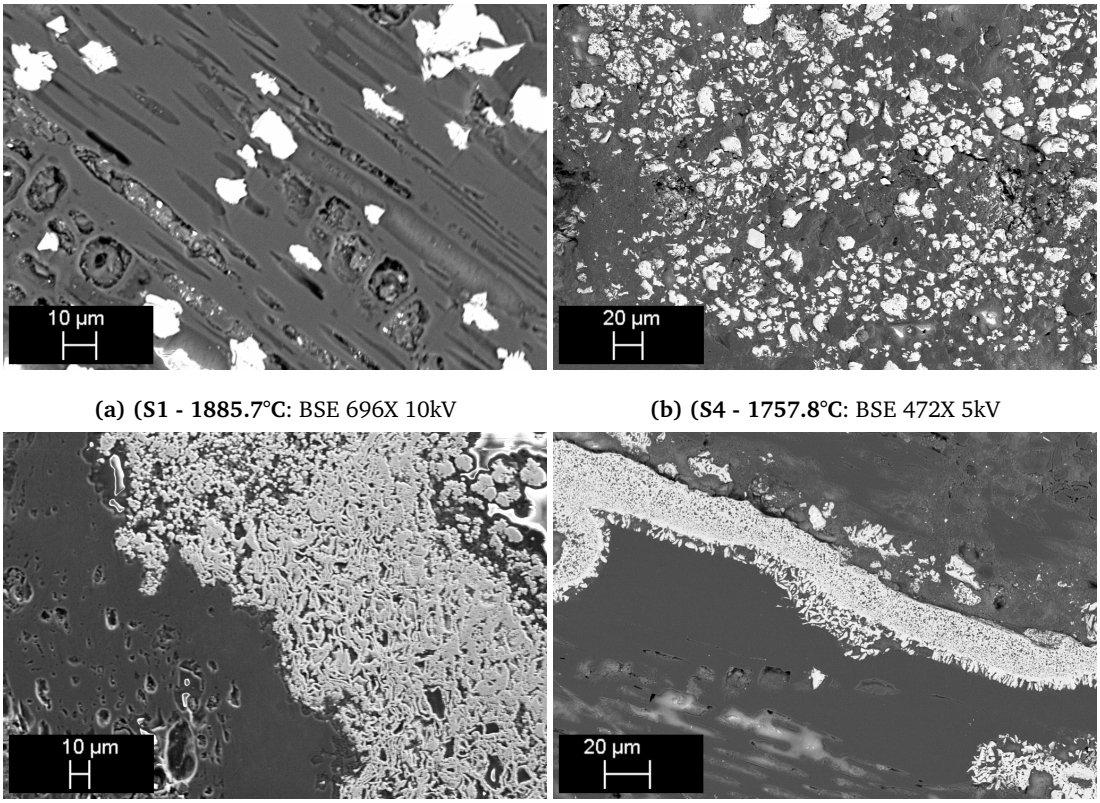

(a) (S1 - 1885.7°C: BSE 696X 10kV

(b) (S4 - 1757.8°C: BSE 472X 5kV

(c) (S1 - 1885.7°C: SE 388X 10kV

(d) (S4 - 1757.8°C: BSE 275X 5kV

Figure 4.12: Although mostly charcoal, some of the black particles were also found to contain crystals and layers of SiC. The brightly coloured areas in all images are identified by EDS to be SiC. In images **(a)** and **(b)** brightly coloured crystals of SiC can be seen. In the other two images, **(c)** and **(d)**, brightly coloured layers of SiC is depicted.

After investigation of the yellow-green particles, it is concluded that they consist of both SiC and C. The yellow-green colour is well correlated with the areas where SiC is present. Figure 4.13 highlights one particle where the boundary between SiC and charcoal is well visible. The following three BSE images are magnifications of this border between SiC and charcoal. There are several different phases depicted in this figure, the most important of which is the large grey coloured area of SiC to the left and the large black coloured area containing C to the right. Optically, it can be seen that the left part of the particle, containing SiC, is yellow-green coloured, while the right part, which is identified to be charcoal, is black coloured. Although the yellow-green particles had large amounts of SiC, many yellow-green particles were found to contain a charcoal core or other areas of charcoal. With that said, it is not unlikely that a yellow-green particle will contain some carbon. Elemental Si was not found inside the investigated yellow-green particles.

In the very same figure, there are two other phases to address. In the region of dark coloured charcoal, large areas of grey coloured ash can be seen. EDS of the ash resulted in a composition of mostly C with lesser parts O, Si, Fe, and Cu. Additionally, a few grains of a white phase is visible in the very same region. Using EDS, these grains are found to contain more than 90 wt% Fe. Such small grains of pure Fe with small concentrations of C were found in several of the investigated samples.

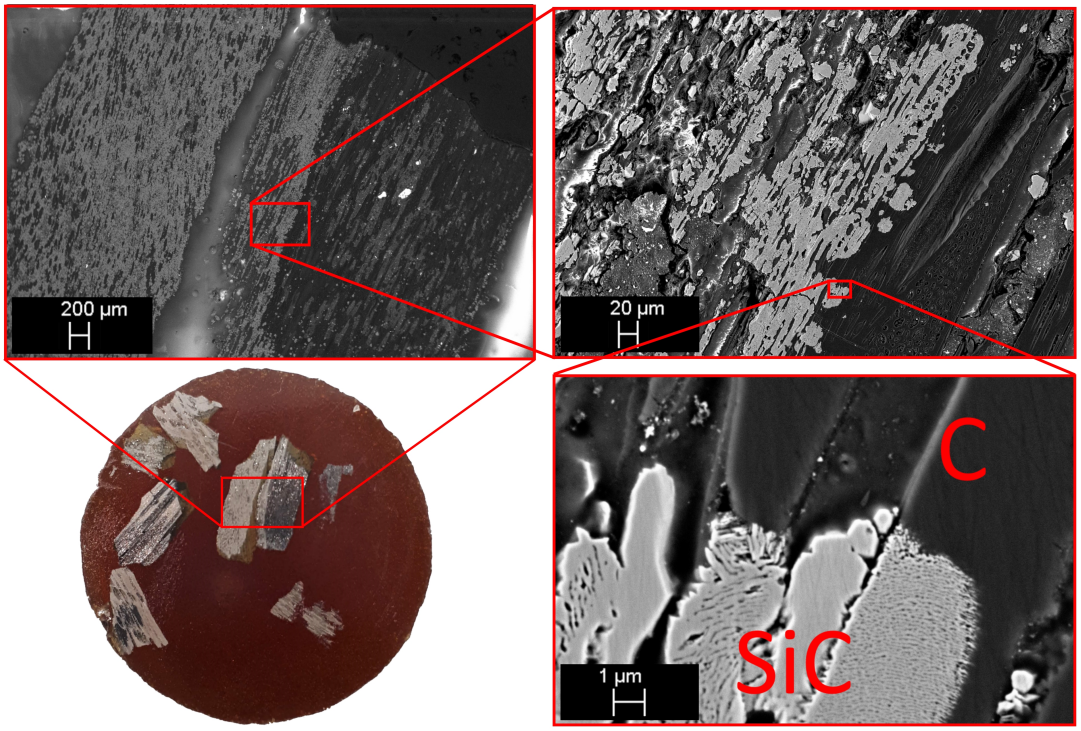

Figure 4.13: S1 - 1885.6 °C: A particle exhibiting both yellow-green and black colours, with magnifications of the boundary between these colours. BSE images correlates the yellow-green colour to areas containing SiC, and the black area to unreacted charcoal.

The grey-blue particle type consist of mostly SiC with varying amounts of elemental Si and C. Most of the investigated grey-blue particles, regardless of temperature exposure, were found to be composed of mostly SiC. Varying amounts of unreacted C remained inside a few of these particles. The concentration of elemental Si inside these grey-blue particles was found to be larger for particles exposed to higher temperatures. Particles exposed to lower temperatures were often found to contain only SiC. Furthermore, particles composed of more Si than SiC, such as the one shown in Figure 4.14, were not often seen.

Three grey-blue particles collected from samples 1 and 4 are shown in Figure 4.14. In these images, the grey areas are SiC, while the brightest grains are areas containing elemental Si. Not to be confused with carbon, the black areas in these images are pores. These three images show the general trend of how the concentration of elemental Si is larger for particles exposed to higher temperatures and

how the concentration varies between each particle exposed to the same temperature. With this in mind, it can be seen that there is a larger concentration of elemental Si in particle **(a)** compared with particle **(b)**. Both particles have been exposed to the same temperature of 1885.6 °C. The grey-blue particle in **(c)**, from sample 4 (1757.8 °C), did not have any elemental Si, but rather a few white grains of pure Fe. Likewise, no elemental Si was found in the other grey-blue particles found in sample 4. Although some carbon was discovered in the investigated grey-blue particles, it can be concluded that carbon was an uncommon discovery.

During the conversion from charcoal to SiC, there were indications of the shrinking-core model, however, not all particles did seem to follow such the model perfectly. As in the typical shrinking-core model, SiC was often found in larger concentrations close to the surface of the investigated particles. However, some investigated particles had crystals of SiC scattered throughout the entire volume of the particle, ahead of the growing SiC layer.

Some investigations revealed elemental Si concentrating the center of a grey-blue SiC particle. The particle which is referred can be seen in Figure 4.14, image **(a)**. Most of the formed Si is found in the center of the particle surrounded by a crust of SiC. Together with the Si, Some grains of SiC can also be seen in the center of this particle. Other investigated particles which had a significant presence of both SiC and elemental Si indicated that Si is more likely to concentrate the center of particles. Consequently, in particles that had been partially transformed from SiC to Si, it was uncommon to find Si near the particle surface.

In grey-blue particles collected from sample 5, which was subjected to a maximum temperature of 1782 ± 17.8 °C, elemental Si was discovered together with SiC. Only two particles collected from sample 5 could be visually identified to be of the grey-blue type. As expected, during the phase analysis of these two particles, large amounts of SiC was revealed. However, inside both the two grey-blue particles, large amounts of elemental Si was also discovered.

One of these two particles from sample 5 is imaged in Figure 4.15 using BSE signals. Image **(a)** shows a larger region of the particle where mainly two more-brightly coloured areas consisting of elemental Si can be seen. In addition to these larger areas, smaller grains of elemental Si can also be seen evenly distributed inside the SiC matrix. One of the larger areas of Si is positioned at the particle surface, while the other area covers the boundary towards an interior pore. The latter area, marked with a red square, is highlighted in image **(b)**. By analyzing this area using EDS, it was confirmed that the larger phase is elemental Si. Surrounding this Si phase is a matrix consisting of SiC and Si. The most brightly coloured phase in this image was found to contain large amounts of Fe, although, the exact composition is unknown. These EDS results are marked in the image accordingly.

The other grey-blue particle from sample 5 also had a few large phases of elemental Si surrounded by

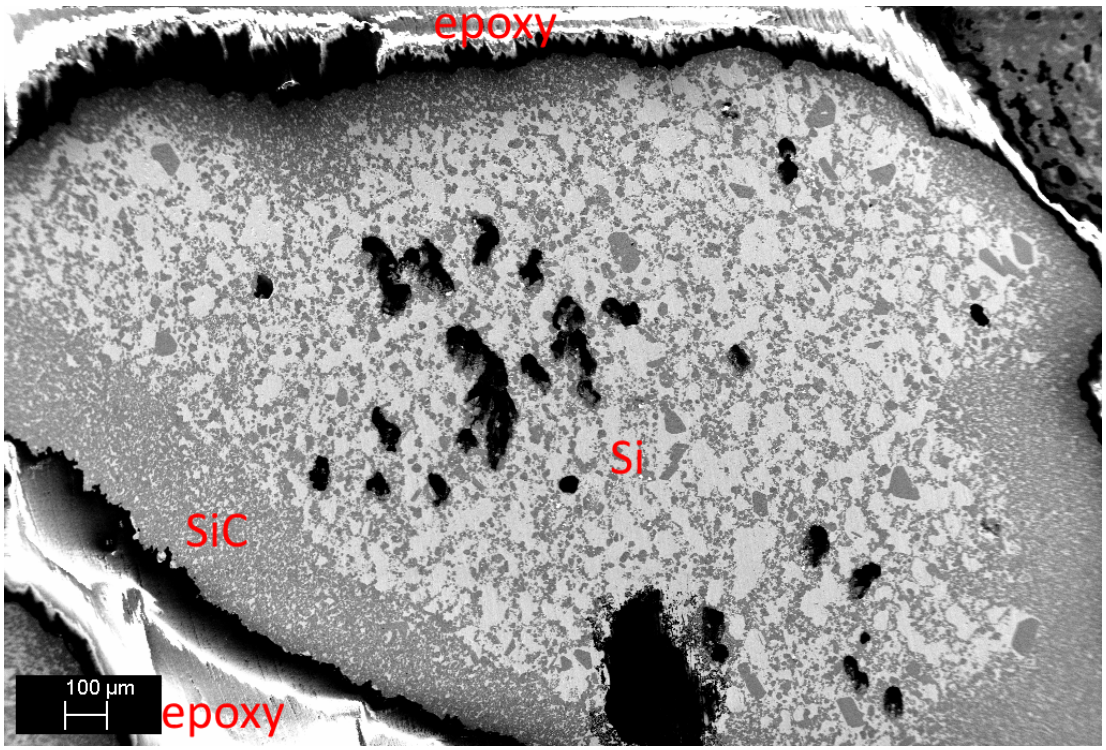

(a) (S1 - 1885.7°C): BSE 55X 10kV

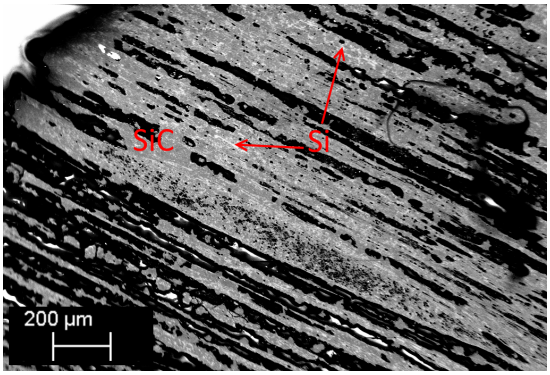

(b) (S1 - 1885.7°C): BSE 60X 10kV

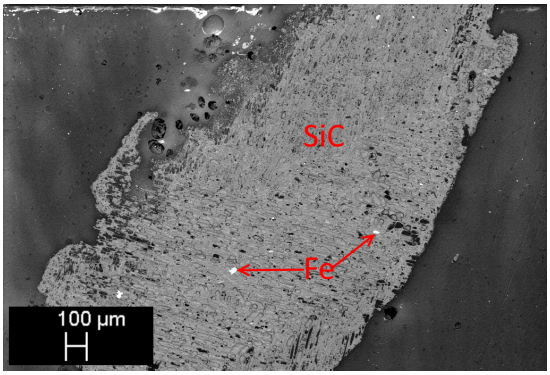

(c) (S4 - 1757.8°C): BSE 44X 10kV

Figure 4.14: BSE images of three grey-blue particles. All images are taken at a similar magnification of 44-60X. In these images, the grey areas are SiC, while the brightest grains are areas containing elemental Si. The black-coloured areas in all images are pores. The particle surface towards the epoxy can be seen in the corners of **(a)**. The amount of elemental Si varies a lot between the investigated particles, but was typically less than the amount of SiC. Particles containing large amounts of Si such as the one shown in image **(a)** was rarely seen. The two other particles shown in images **(b)** and **(c)** with less elemental Si was not uncommon. Peculiarly, while looking at image **(a)**, it can be seen that most Si is located in the center of the particle, surrounded by a crust of SiC.

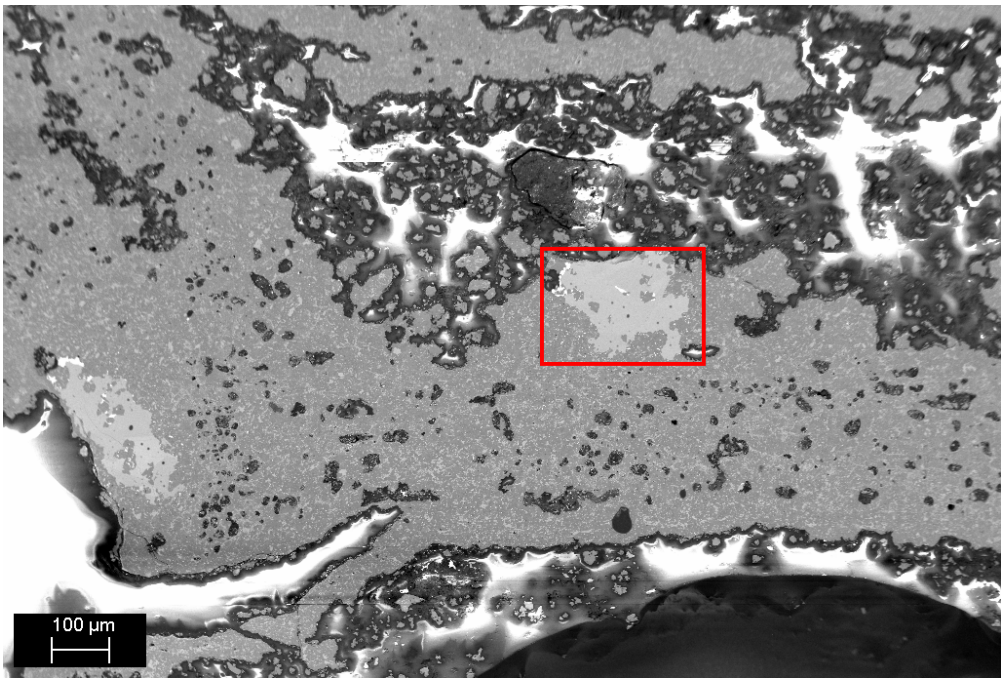

(a) BSE 66X 5kV

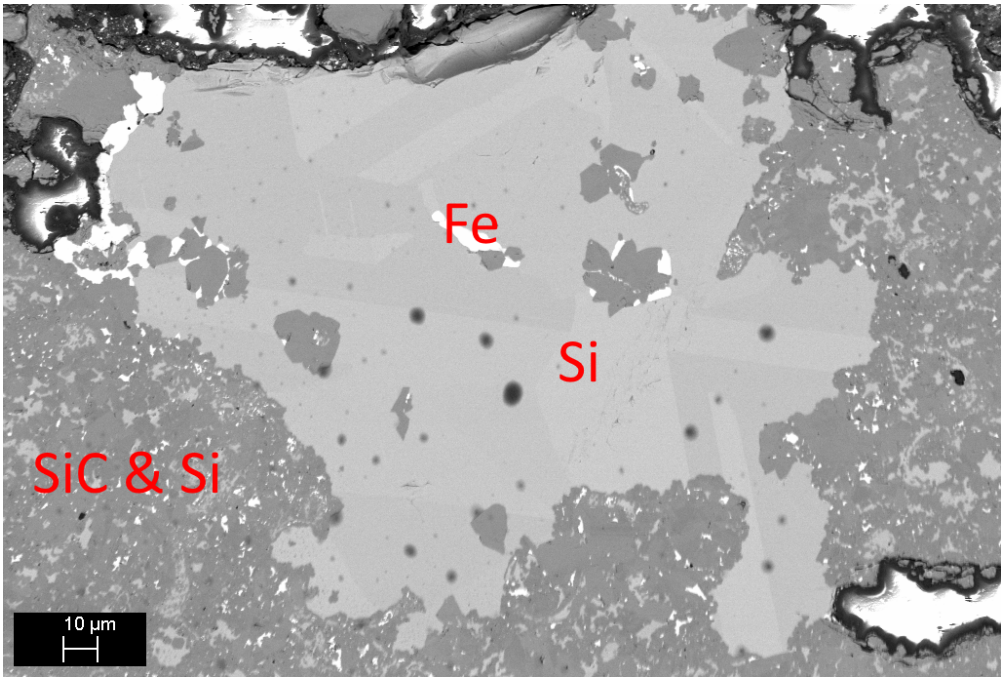

(b) BSE 396X 5kV

Figure 4.15: (S5 - 1763.7°C): One of the two grey-blue particles collected from sample 5. In this particle, large phases of elemental Si was found together with a matrix of SiC and Si. Image **(a)** shows a larger region of the grey-blue particle, including a marked area which is highlighted in image **(b)**. EDS analysis was performed to confirm the phase composition of the different areas in image **(b)**. The temperature was measured to be maximum 1763.7 ± 17.8 °C.

a matrix of SiC and Si. These areas of Si was positioned inside the grey-blue particle, not particularly close to the particle surface or an interior pore. Similarly to the other investigated grey-blue particle from sample 5, EDS was used to confirm the composition of the different phases.

With the exception of elemental Si formation, no correlation between the particle phase composition and the temperature was found. Grey-blue particles composed of only SiC without any Si were found only in samples 4 and 5. No correlation between the formation of SiC and temperature was found.

4.3.4 Morphology

The morphology of the different phases and crystals was investigated. First, the crystals found on the particle surfaces will be presented, followed by the crystals found inside the pore structure. Last, the morphology and growth of SiC throughout the particles will be presented.

The shape of the crystals found on the particle surface is believed to be a function of many variables, including temperature and degree of SiC conversion. The temperature which the particles experience, depends on the particle placement inside the carbon charge. Furthermore, the degree of particle conversion towards SiC, or even elemental Si, might affect the shape of these crystals. For example, some crystals were found to be more spherical, most likely due to the presence of elemental Si inside the crystal core. To make matters more complex, the crystal morphology could vary between different regions on the surface of the same particle. Some particles could have regions where one type of crystal shape was in abundance. Consequently, it would be inaccurate to compare a particle surface grown crystal from one sample with another sample. Yet, an effort is made to present the different shapes of crystal in an understanding manner.

Using the image analysis software, ImageJ, the diameter of crystals grown on the particle surface was compared with crystals found inside particle pores. The resulting size distribution can be seen in Figure 4.16. The size of crystals found on the particle surface is generally found to be larger than what was found inside the pores.

Both mono- and poly-crystals were found covering the particle surface in the form of mostly hexagonal morphologies. A collection of different crystal shapes with a diameter up to 30 μm found on the surfaces of samples 1, 2, and 5 are seen in Figure 4.17. Peculiarly, as seen from this figure, several mono-crystals can be seen with the shape of hexagonal pyramids, indicating to an underlying hexagonal structure. If this is to be true, these crystal are α-SiC. On a few occasions, hexagonal basal plates was discovered, and is shown in images **(a)**, **(d)**, and **(g)**. These hexagonal basal plates were less common than pyramids. On the surface of the hexagonal basal plates, a layer-by-layer mech-

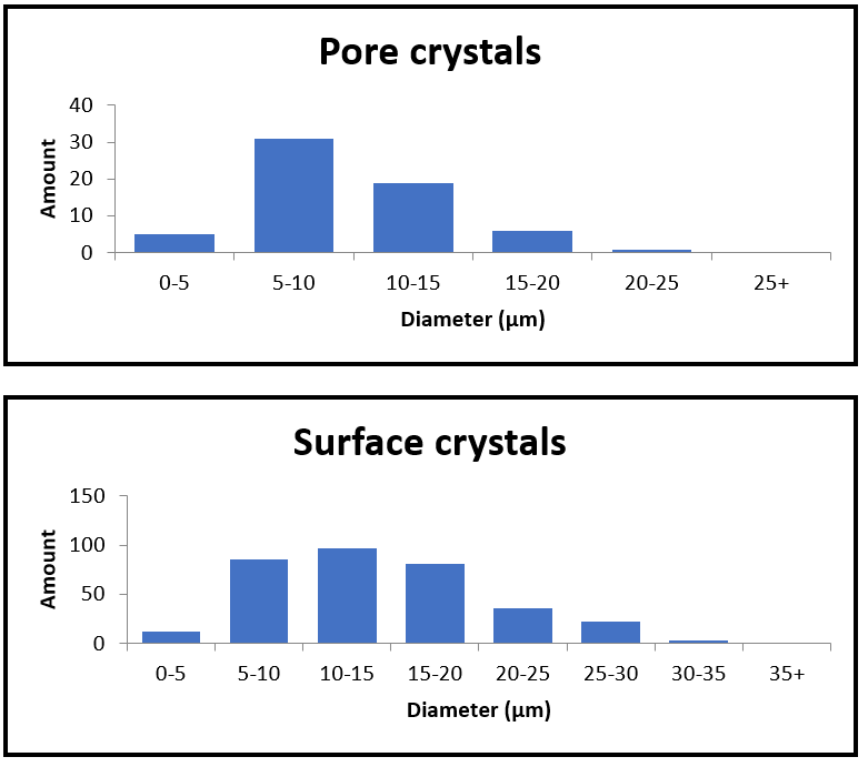

Figure 4.16: The diameter of crystals grown on the particle surface was compared with crystals found inside particle pores. The largest diameter of surface-grown crystals was found to be around 30 μm, while the crystals found inside pores had a maximum diameter of about 20 μm. Little correlation between crystal size and temperature or particle colour were found.

anism of growth is visible. Hexagonal crystals (pyramids and basal plates) were common in all of the investigated samples. However, on the particle surface, poly-crystals were much more common when compared with mono-crystals. The crystal types which are shown in images **(c)** and **(i)** show such a poly-crystal morphology where several individual hexagonal pyramids exist in the very same crystal. More than one crystallographic direction within the same crystal is typical of poly-crystals. Finally, the crystal shape as seen in image **(f)** was also very common in all samples.

The crystals found inside the pore structure of the different particles are more likely to be mono-crystalline and indicate the presence of both β- and α-SiC. Several crystals found inside the pore structure from various samples are imaged in Figure 4.18. Although both poly- and mono-crystals were found inside the pore structure, the mono-crystalline growth was found to be more common. The various shapes of the investigated mono-crystals indicate an underlying cubic structure, which implies that the crystals are 3C β-SiC. Additionally, a few of the mono-crystals inside the pore structure exhibit epitaxial growth resulting in a hexagonal pyramid morphology, similar to what was found on the surface. Again, such a hexagonal shape can indicate an underlying hexagonal crystal struc-

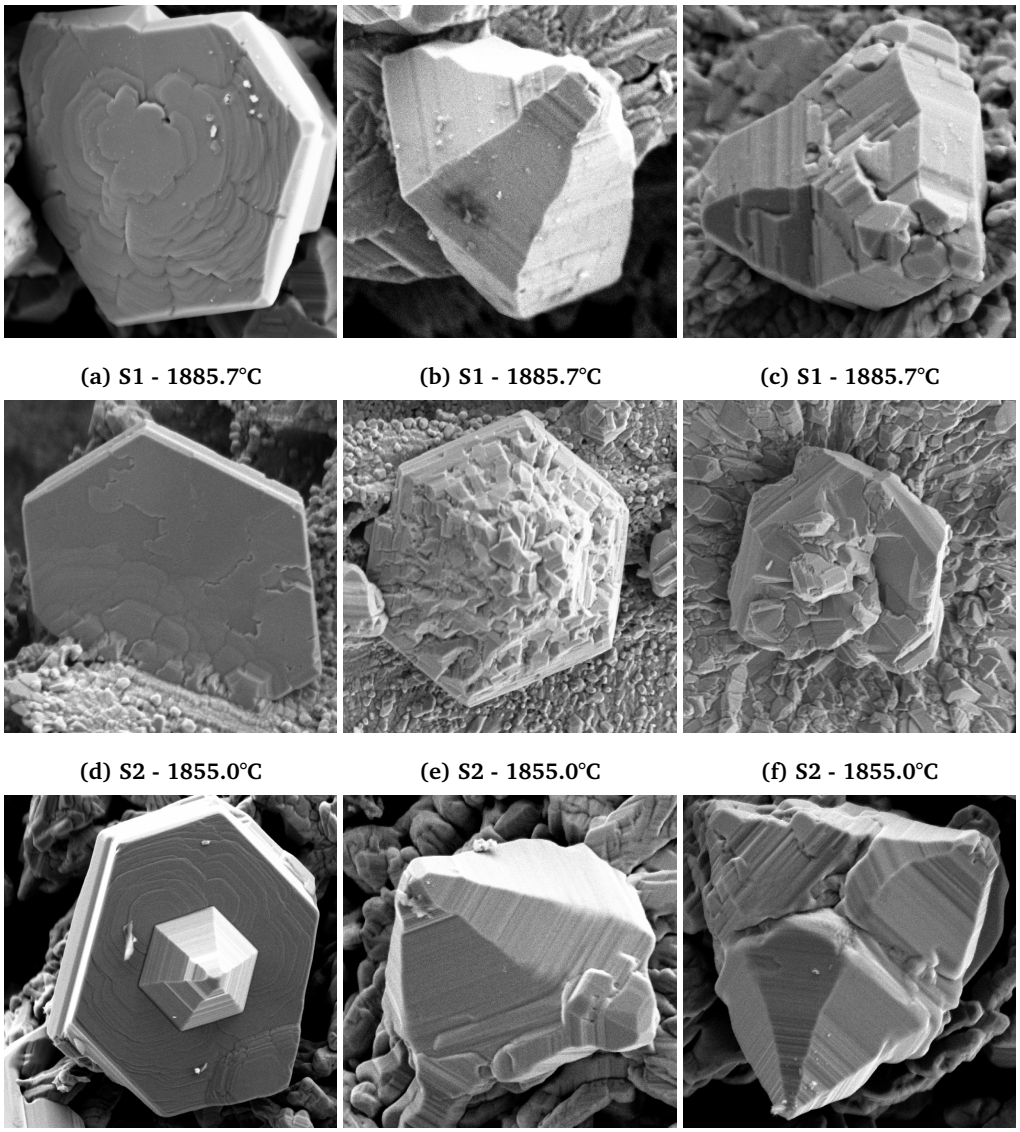

(a) S1 - 1885.7°C **(b) S1 - 1885.7°C** **(c) S1 - 1885.7°C**

(d) S2 - 1855.0°C **(e) S2 - 1855.0°C** **(f) S2 - 1855.0°C**

(g) S5 - 1757.8 °C **(h) S5 - 1757.8 °C** **(i) S5 - 1757.8 °C**

Figure 4.17: The crystals found grown on the particle surfaces, displayed several morphologies, both mono- and poly-crystalline. The mono-crystals seen in images **(a)**, **(b)**, **(d)**, **(e)**, **(g)**, and **(h)** have a hexagonal shape. Some are hexagonal basal plates, while most is found to be hexagonal pyramids. Poly-crystals, such as the ones shown in **(c)**, **(f)**, and **(i)** were much more common on the particle surfaces. The maximum size of all these crystal growths was found to be around 30 μm diameter.

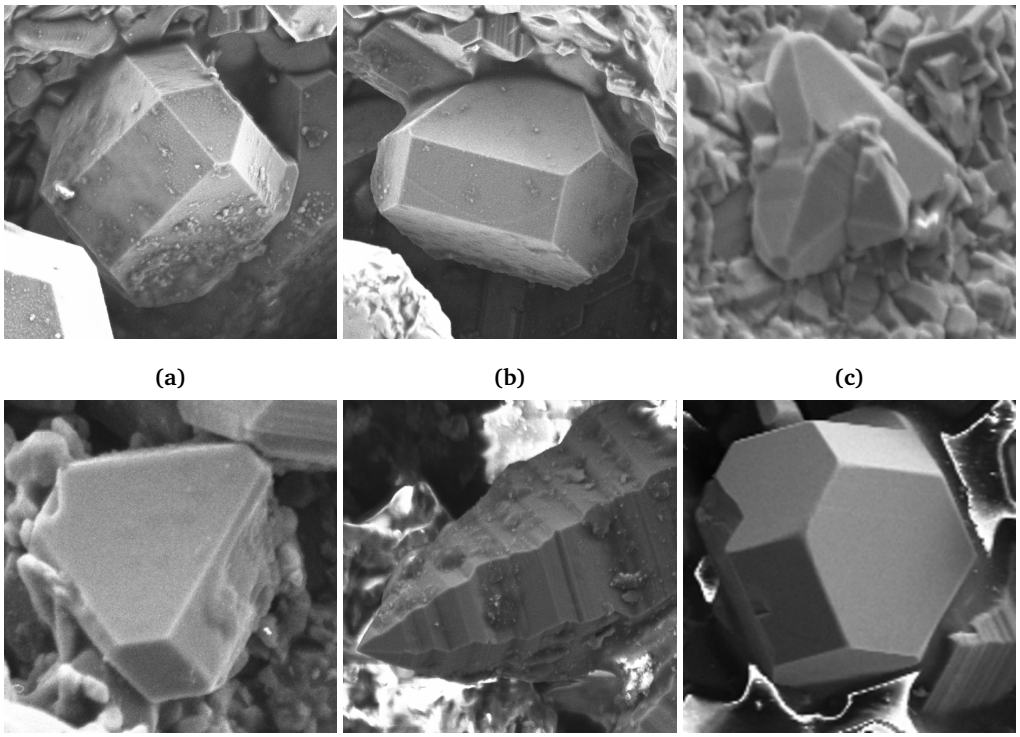

(a) **(b)** **(c)**

(d) **(e)** **(f)**

Figure 4.18: Examples of the final shape of grown crystal found inside pores of the investigated particles. Although both poly- and mono-crystals could be found, the mono-crystal morphology was more common inside the pores. The crystal shown in image **(e)** was only found in sample 4, which was exposed to a (stabilized) temperature of 1757.8 °C. The size of these crystals varies between 4-15 μm diameter. The maximum size was found to be around 20 μm diameters for pore grown crystals.

ture. The hexagonal crystals, such as the ones in image **(e)** and **(c)**, were rarely seen inside the pores. The hexagonal pyramid crystal seen in image **(e)** was found in sample 4, which was subjected to a temperature of 1757.8 °C. The epitaxial growth and resulting shape of this crystal is typical of hexagonal systems. Hence, it is possible that these are hexagonal α-SiC.

Figure 4.19, from the grey-blue particle type, show both the initial stages of Si formation and the later stages where remaining SiC is present as faceted grains. Images **(a)** and **(b)** in the figure show the initial stages of Si formation inside a SiC particle. In these images, formed Si is surrounding a faceted grain of SiC. In images **(c)** and **(d)** a later stage of SiC to Si transformation is seen. Here, the faceted grains of SiC are present inside a matrix of Si.

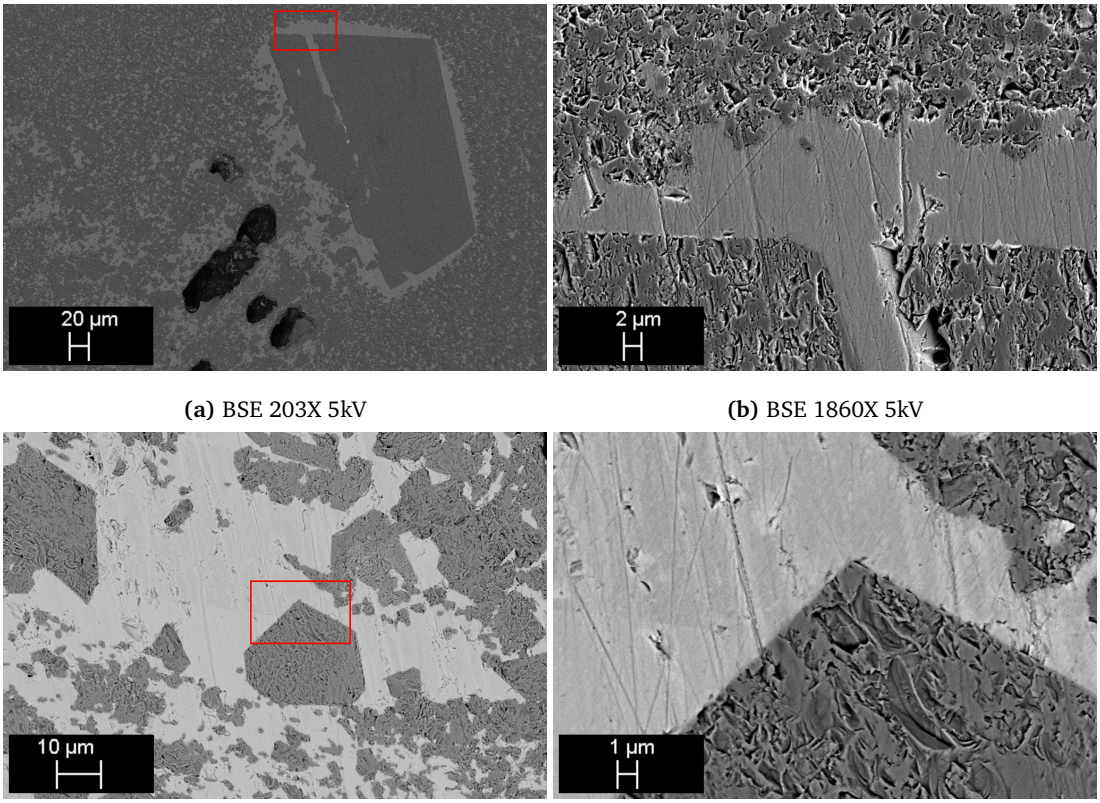

(a) BSE 203X 5kV

(b) BSE 1860X 5kV

(c) BSE 915X 5kV

(d) BSE 4050X 5kV

Figure 4.19: (S1 - 1885.7°C): Two locations inside grey-blue particles showing how the formation of Si inside a SiC matrix results in faceted grains of SiC. Red squares on the images to the left are magnified and shown to the right. Images **(a)** and **(b)** show the initial stages of SiC to Si transformation. The later stages is shown in images **(c)** and **(d)**. The darker coloured phase in all images is SiC, and has a rough surface compared with the formed Si. The bright coloured phase is Si.

Revealed from the same figure is a relatively rough surface of SiC. Contrary, the same amounts of pores or dimples are not visible in the formed Si. Note that stripes seen on the surfaces of both Si and

SiC are believed to originate from the grinding and polishing during sample preparation. However, it is not certain whether the surface roughness of SiC also originates from this grinding and polishing stage.

The morphology of SiC throughout the charcoal particles could be separated into two groups depending on growth location: carbon or pore. The morphology of SiC between these two locations was found to be different. Figure 4.20 displays the inner pore structure of a partially converted yellow-green particle. Although converted to SiC, a contrast between the clogged pores and carbon is still visible. The SiC formed inside the pores does not seem to have any specific growth direction. Comparatively, the SiC found growing through areas of carbon has a growth direction which appears to originate from the pores. The resulting structure is SiC crystals inside the pores, with a directional growth of SiC away from this crystal. Consequently, it is possible that SiC is first formed as crystals inside the pores, and further growth into the charcoal structure occurs from these crystals.

This growth mechanism has also been seen occurring on the particle surfaces. Images from the particle surface indicate a growth mechanism where a crystal is grown first, and the directional growth originates from this crystal. The result of this growth mechanism, shown in Figure 4.21, looks similar to a blossomed flower. This specific image was taken from a grey-blue particle from sample 2, which was subjected to 1855 °C. The particle was covered with such crystals which resembled blossomed flowers.

4.4 XRD

The black, yellow-green and grey-blue particle types from sample 1 were pulverized using a wolfram-carbide ring mill and analyzed with XRD. For reference, charcoal particles were also pulverized in a similar matter. The comparative results from this analysis can be seen in Figure 4.22 and will be explained further in this section. In the figure, the black, yellow-green, and grey-blue particle types are coloured red, blue, and green, respectively. Note that the complete XRD spectrum is included in Appendix B.

Not considering the charcoal reference, the black particle type was the only specimen containing carbon. The very broad peak indicating carbon is located at an angle less than $2\Theta = 30°$ and is visible in both charcoal and the black particle type. This peak is not present in the yellow-green or grey-blue particle types.

All the three particle types (black, yellow-green and grey-blue) contained varying amounts of 3C β-SiC, while indications of 4H α-SiC was found in the grey-blue particle. One of the larger peaks

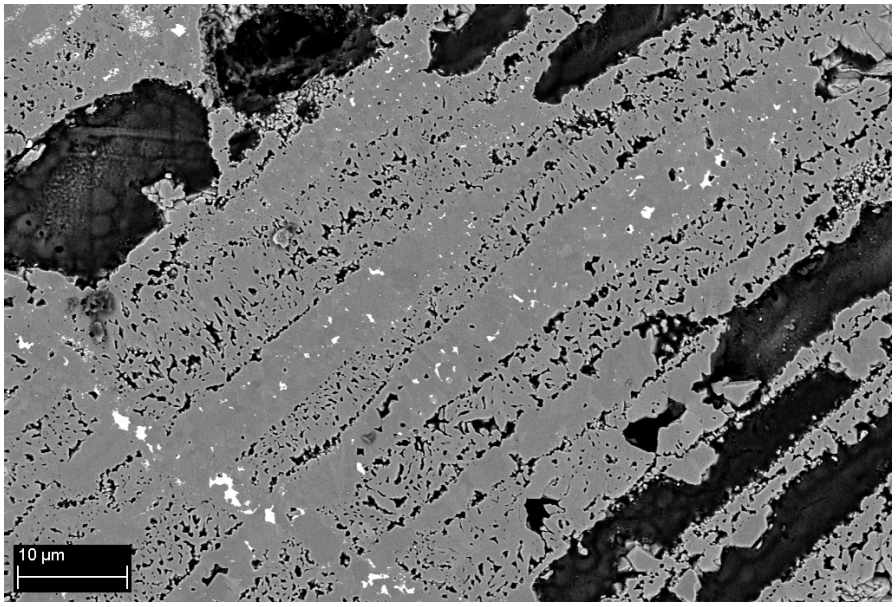

(a) BSE 1410X 5kV

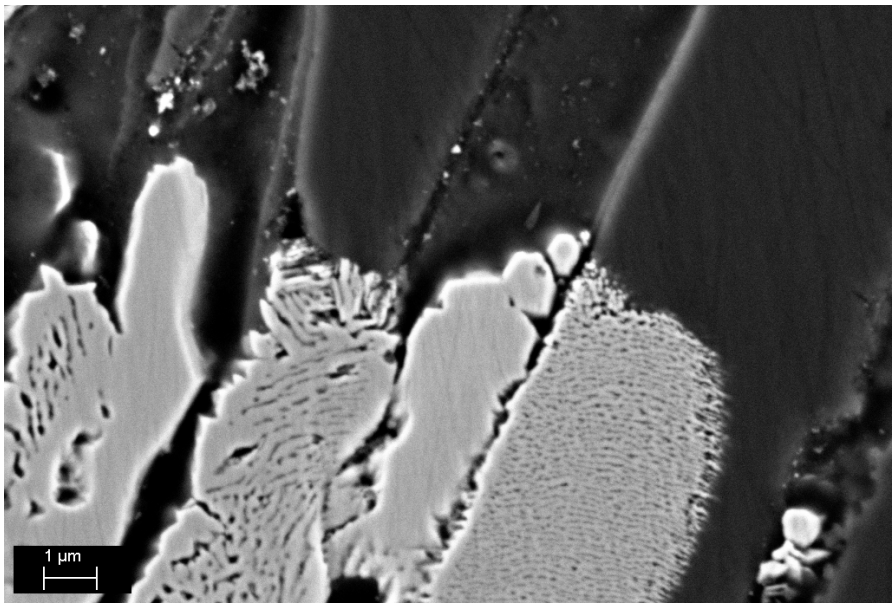

(b) BSE 6840X 5kV

Figure 4.20: (S1 - 1885.7°C): In some particles, there were indications of SiC growing into the charcoal structure with the pores as an origin. The images shown are from the inner pores structure of a yellow-green particle. In these images, there is a contrast between the morphology of SiC found formed inside the pores and through the charcoal structure. SiC inside the pores appear as a mono-crystal, while the SiC throughout the carbon has a growth direction away from the pores. This indicates that SiC is first formed as crystals inside the pores, and further growth into the charcoal structure originate from these crystals.

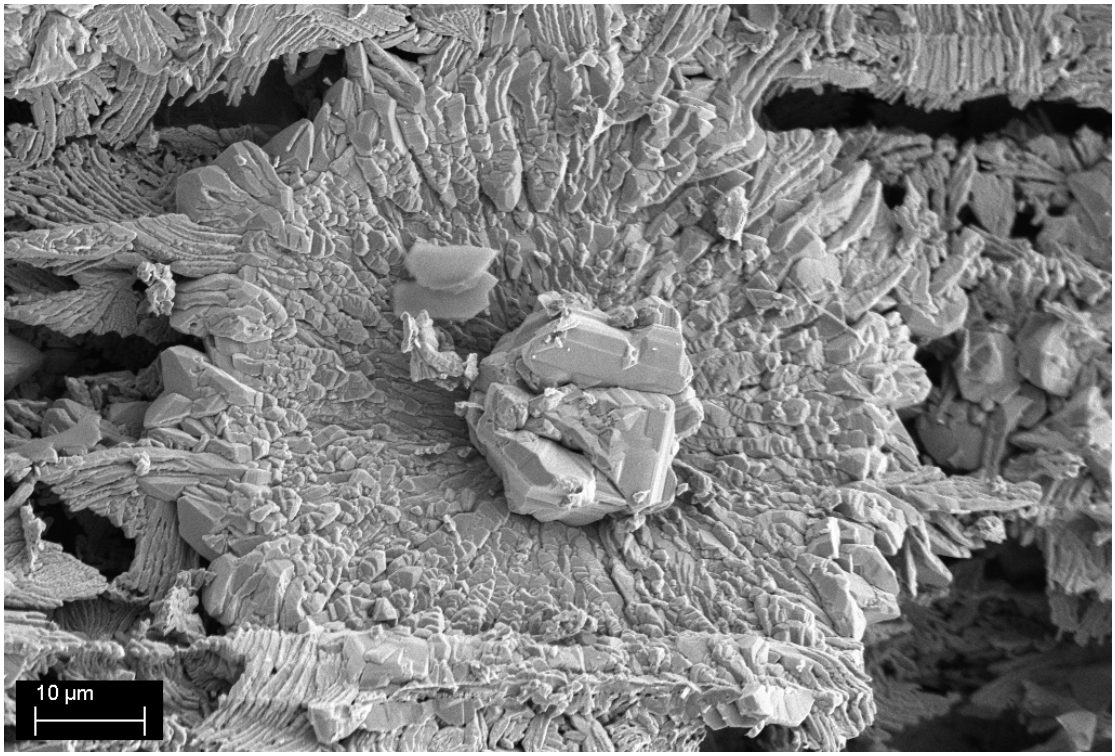

Figure 4.21: (S2 - 1855.0°C): Image from the surface of a grey-blue particle highlighting a growth mechanism of SiC originating from crystals. It indicates that SiC deposits and grows as a crystal first, followed by directional growth away from the crystal.

indicating 3C β-SiC can be seen at $2\Theta = 35°$ and is present in all specimens, except the charcoal reference. The TOPAS analysis also investigated for several other polytypes of SiC (4H, 6H, and 15R). The 4H α-SiC polytype was also discovered in the grey-blue particle. A magnification of the grey-blue particle spectrum is also provided in Figure 4.22. In this magnification, the characteristic spectrum of 3C and 4H polytypes of SiC are included for comparison. There is a small correlation between the small peaks from the grey-blue spectrum and the characteristic spectrum of 4H-siC.

The full results of the TOPAS analysis is included in Table 4.2. Note that the software used to quantify the amounts of each phase only looks for the phases it is told to look for. For this reason, the results should only be used qualitatively. However, it can be assumed that both the yellow-green and the grey-blue particle types do not contain any carbon, due to the missing broad peak at $2\Theta < 30°$. If this is to be true, and no other phase is present, the yellow-green particle type contains only β-SiC, while the grey-blue particle is $\sim$72 % β-SiC and $\sim$11 % 4H α-SiC. The remaining 17% in the grey-blue particle type was identified to be elemental Si. The peak of Si is visible at about $2\Theta = 28°$.

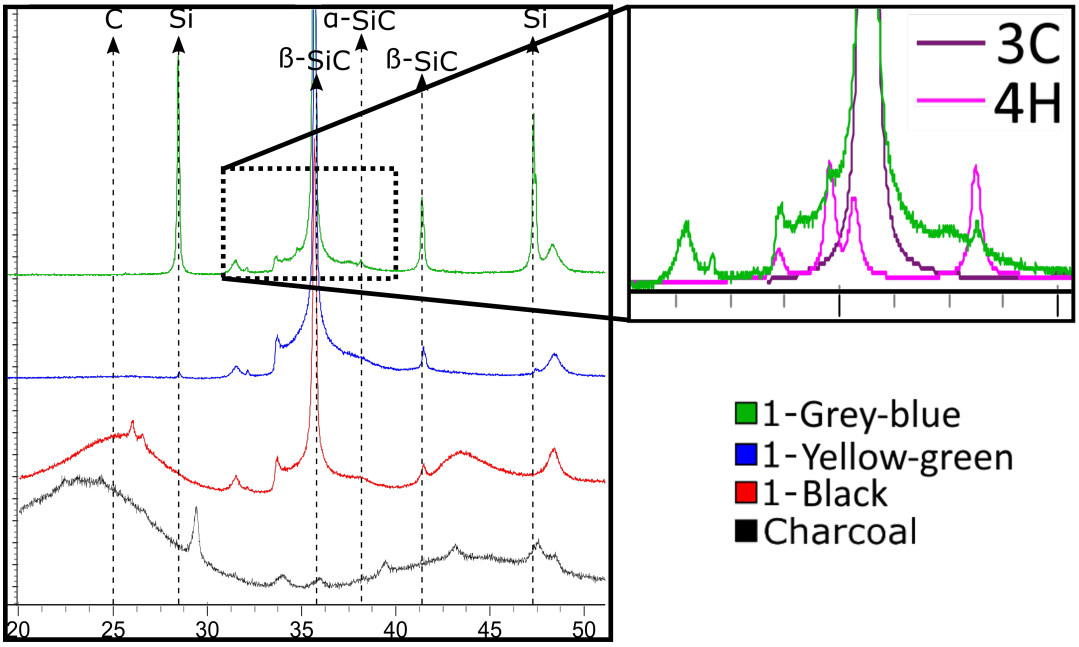

Figure 4.22: (S1 - 1885.7°C): XRD results of the different particle types; black, yellow-green, and grey-blue. On the x-axis, the 2Θ is given. Also included as a reference in this comparison is a charcoal particle. The positions of carbon (C), silicon (Si), 3C β-SiC, and 4H α-SiC are included in this diagram at their respective locations. 4H α-SiC was detected in the grey-blue particle, and an area showing this 4H SiC is magnified to the right. The corresponding characteristic spectrum for the 3C and 4H polytypes are shown together with the green grey-blue particle.

4.5 Results summary

After experiments, cross-sections of the various sample crucibles revealed large amounts of unreacted SiO_2 and Si. There are rough indications that the reaction rate between SiO_2 and Si increases with temperature. There was little to no indications of condensates inside the carbon charge.

Visually, the particles collected from the charcoal charge after experiments could be divided into three groups according to colour: black, yellow-green, and grey-blue. Droplets of Si were often visible on the surface of the grey-blue particles. The mass balance of the carbon charge revealed a linear trend between the change of charcoal mass and temperature. After the experiments, samples exposed to temperatures higher than 1800 °C were found with an increased carbon charge mass. Samples 4 and 5, which was subjected to the temperatures below 1800 °C, had a negative mass balance.

SEM investigations revealed the growth of SiC crystals up to 30 μm diameter on the surface and up to 20 μm diameter inside the pore structure of the various investigated particles. An EDS analysis,

Table 4.2: The results from the TOPAS analysis sample 1 XRD results. Note that the software used to quantify the amounts of each phase only looks for the phases it is told to look for. For this reason, the results should only be used qualitatively. All particle types were found to contain 3C β-SiC, while 4H α-SiC was found only in the grey-blue particle. Note that these are sums of Si and SiC, C is not included.

Particle	**3C-SiC**	**4H-SiC**	**Si**
	wt%	*wt%*	*wt%*
Black	100	0	0
Yellow-green	99.83	0	0.17
Grey-blue	72.43	10.92	16.65

which was performed on the faceted crystals, confirms their composition to be of SiC. BSE images from the pore structures, confirms that these crystals of SiC can grow directly on a carbon surface. The amount of crystals seem to increase from the black to the yellow-green particle type, while the amount on grey-blue is similar to yellow-green. The surface of the grey-blue particle type is more rough and faceted compared with the black and yellow-green particle types. No correlation between the crystals and temperature was found.

Areas of SiC were typically lacking smaller pores, and crystal growth was observed in the smaller pores inside regions of charcoal. Figure 4.9 show an area of partially converted charcoal. Peculiarly, there is a sharp contrast between the amount of smaller pores in the dark coloured area of charcoal and the grey coloured SiC. Closer investigations of the small pores inside regions of charcoal revealed a substantial amount of small crystals consisting of SiC. Equally, large crystals are found in abundance inside the larger pores. Large pores were common in the converted SiC particles. There are faint indications that samples exposed to higher temperatures undergo larger structural changes.

The phase composition of the three different particle types collected from each sample was investigated mostly using SEM. The black particle is simply unreacted charcoal. Nevertheless, a few black particles were found to contain crystals or layers of SiC (Figure 4.12). On the other side, the grey-blue particles are found to be mostly SiC, with lesser amounts of Si. The phase composition of the yellow-green particle is somewhere in between the conversion from black charcoal to grey-blue SiC. Generally, the yellow-green particles contained large amounts of both charcoal and SiC, but with no traces of elemental Si. It is emphasized that the grey-blue particle type almost always contained some elemental Si. No correlation between the formation of SiC and temperature was found.

The formation of elemental Si in SiC was found to occur at temperatures below 1800 °C. A grey-blue particle collected from sample 5 was found to contain small amounts of elemental Si when investigated in SEM (Figure 4.15). It was confirmed by EDS analysis that this brightly coloured

phase is elemental Si. This grey-blue particle was found close to the thermocouple, which measured a maximum temperature of 1781.8 ± 17.8 °C during the 1 hour holding time.

Rough indications of the shrinking-core model were found as charcoal is converted to SiC. However, some particles had crystals of SiC scattered throughout the entire particle volume, well ahead of the growing SiC-layer. The formation of elemental Si does not seem to occur at any specific location. However, some particles showed that elemental Si was more likely to be found concentrating the center of the particle, rather than near the particle surface.

The morphology of these crystals could be divided into mono- and poly-crystals. The crystals found on the surface are mostly poly-crystalline, however, some mono-crystalline growth was also seen. Crystals found on the surface were more likely to resemble hexagonal plates or pyramids, indicating a α-SiC polytype. Contrary to this, the crystals found inside the pore structure were mostly mono-crystals and indicated to β-SiC.

The conversion of charcoal to SiC could occur by the formation of crystals on any surface, followed by a directional growth throughout the particle. Many images (Figures 4.20 and 4.21) reveal two different morphologies of SiC, one found clogging the pores with crystal growth, while the other grow directionally through the carbon.

Furthermore, a number of black, yellow-green, and grey-blue particles from sample 1 were pulverized and analyzed using XRD. The results can be seen in Figure 4.22, together with pulverized charcoal as a reference. Clear peaks of carbon were only found inside the black particle type. All three particle types were found to have varying amounts of β-SiC (3C). Indications of 4H α-SiC was discovered in the grey-blue particle type. The grey-blue particles were also found to contain elemental Si.

Chapter 5

Discussion

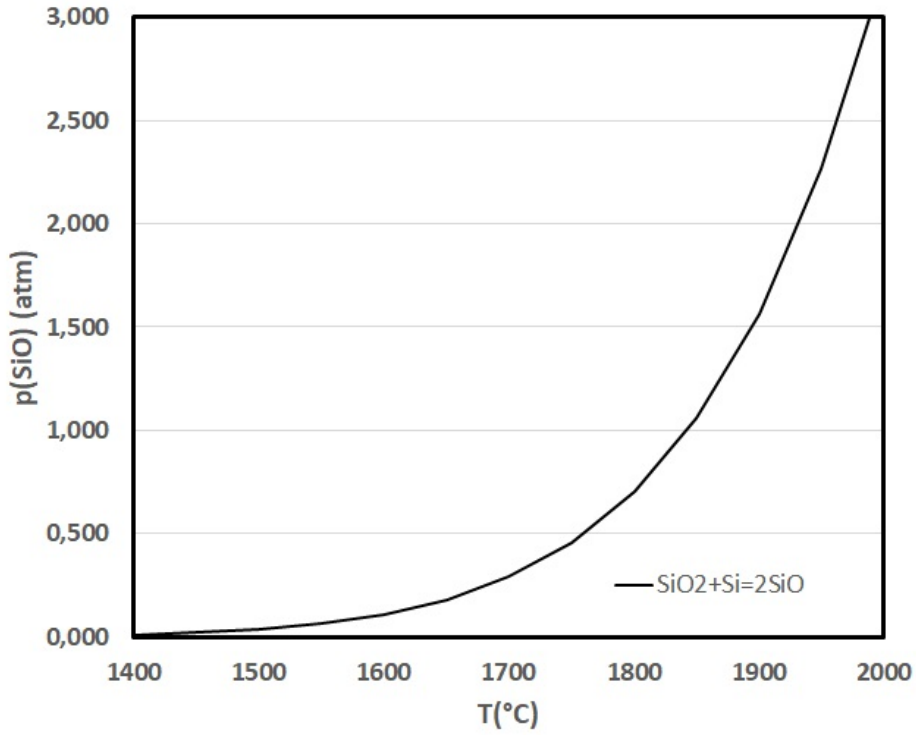

Figure 5.1: Equilibrium diagram of the reaction between SiO_2(l) and Si(l) to form SiO(g) created using the HSC 9 Chemistry database. A significant evolution of SiO-gas is expected to occur above 1500 °C.

In the initial stage of the experiment, there is only one reaction to consider; the reaction between SiO_2 and Si to form SiO-gas. According to the equilibrium diagram in Figure 5.1, constructed from HSC Chemistry 9, significant evolution of SiO-gas will first occur at about 1500 °C. At this early stage, Ar-gas is present inside the crucible, but can be assumed to be forced out due to increasing partial

pressures of SiO and CO. Additional Ar-gas is applied to the furnace at the top of the carbon charge. With that said, it can be assumed that Ar-gas will not be present in any significant amounts inside the crucible after the initial stages of the experiment. Consequently, with this assumption, the total pressure measured is simply the sum of SiO- and CO-gas.

Figure 5.1 is, however, only applicable to identify the lower temperatures where SiO-gas is produced. After this, the interaction between SiO-gas and other species has to be accounted for. As previously mentioned in Chapter 2, the presence of mixtures or gases will affect the equilibrium of the system. For that reason, the evolution of CO-gas has to be accounted for. An equilibrium diagram which better represents the system was presented by Schei (1998)[10]. Similarly, the same diagram was created using the HSC Chemistry 9 database and is shown in Figure 2.4. The main difference between these two diagrams is the triple-point temperature. Schei found it to be at 1811 °C, while the one calculated using the HSC 9 database was found to be closer to 1800 °C. Hence, it is indicated that the temperature Si-production, is lower than previously thought. Nevertheless, these temperatures depend very much on the accuracy of the database the diagram has been constructed from.

The same diagram constructed using the HSC Chemistry 9 database is reproduced in Figure 5.2 using a more relevant temperature range. In this figure, the maximum temperatures measured in the carbon charge is shown as dotted red lines.

There are a few important assumptions which have to be addressed if any of these equilibrium diagrams can be used. First of all, it is assumed that no Ar-gas is present inside the crucible. Hence, there are only two gaseous species, SiO and CO. Secondly, it is assumed that the sum of the partial pressure of these two species is equal to 1 bar. Finally, it has to be assumed that the partial pressures of each species at 1 bar do not change when the total pressure reaches 1.45 bar. In other words, the partial pressures of all species are independent of the total pressure. With these assumptions, it is possible to compare the experimental results from this work with the theoretically constructed equilibrium diagram: First of all, as seen in Figure 5.2, samples 4 and 5 experienced a maximum temperature below the ternary point of 1800 °C. Hence, given a sufficiently large partial pressure of SiO-gas, this gas becomes unstable by condensation or reaction with CO-gas. In other words, samples 4 and 5 could, depending on the partial pressure of SiO-gas, contain SiO_2. Furthermore, as these two samples are outside the region of Si production through Reaction (1.4), no elemental Si is expected to be formed. Following the same reasoning, samples 1, 2, and 3 would contain elemental Si, but little or no SiO_2. It can also be seen that at equilibrium SiC will be formed at almost any temperatures and at very low partial pressures of SiO-gas.

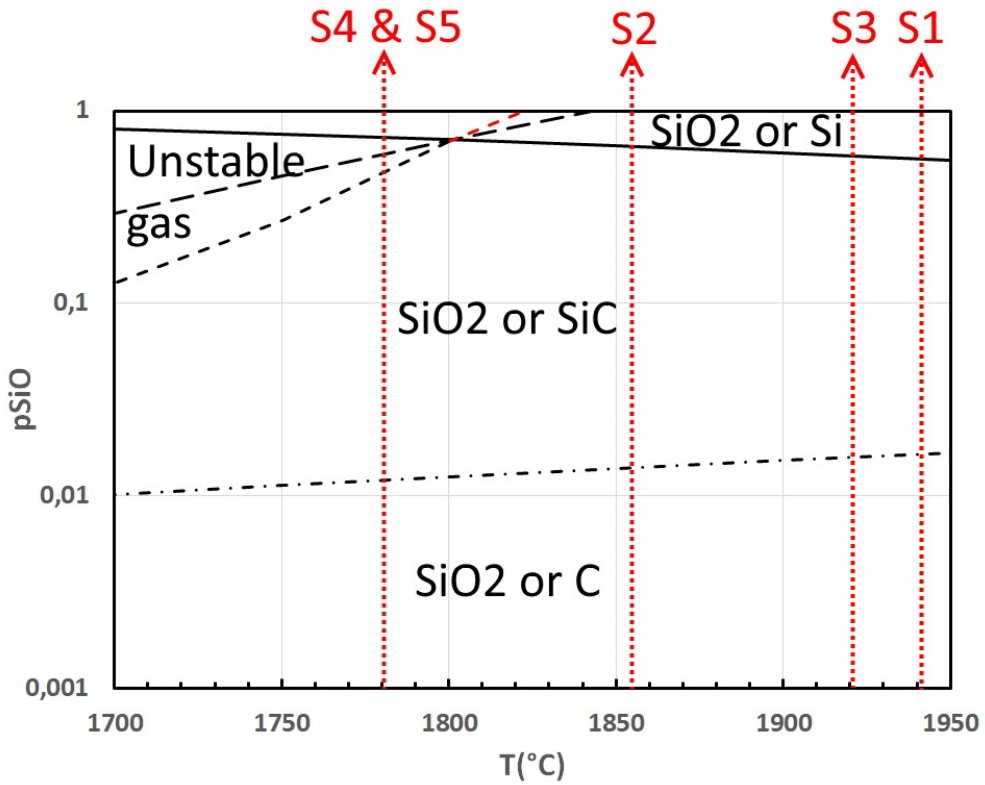

Figure 5.2: Equilibrium diagram of the Si-C-O-system with the partial pressure of SiO-gas and temperature as variables. The equilibrium diagram is constructed assuming a total pressure of 1 bar with the HSC Chemistry 9 database. The maximum temperatures measured in the carbon charge for each sample is shown as a dotted red line.

5.1 Visual

The particle collected from the carbon charge could be separated by colour into three different groups: *black*, *green-yellow* and *grey-blue*. As told by Harris (1995)[7], the cubic β-SiC, exhibits a yellow or greenish-yellow colour depending on the impurities, similar to what is found in this study. With this in mind, the final grey-blue colour can be explained by a presence of elemental Si. The presence of elemental Si could often be visually confirmed, as droplets of Si was typically seen on the grey-blue particle surface.

Little indication of SiO-gas condensation in the form of SiO_2 was discovered in the carbon charge of any of the experiments. Following the equilibrium diagram in Figure 5.2, samples 4 and 5 could have contained SiO_2 given a sufficiently large pressure of SiO-gas. Regarding all samples, just a few grey-blue particles were found glued together. Although not confirmed, it is believed that the glue might be SiO_2. Yet, from an overall view, significant amounts of SiO_2 was barely seen, which can

either indicate to an inaccurate equilibrium diagram or that the condensation reaction is slower than the reaction to form SiC and Si. This would however require further investigation.

5.2 Mass change

As expected, there is a carbon charge mass increase at temperatures above 1775 °C due to the formation of SiC and elemental Si. This increase, as shown in Figure 4.1, was observed to occur linearly when compared with temperature. A mass decrease was also observed for samples at temperatures below 1775 °C

Peculiarly, there was a decrease in carbon charge mass for samples exposed to temperatures less than 1800 °C. The most probable cause for this mass decrease, is the evaporation of volatiles and moisture from charcoal. In Table 3.1 **(b)**, 7.41 to 8.01 wt% of the charcoal is measured to be volatiles, while 8 wt% is found to be moisture. Summarized, the evaporation of volatiles and moisture results in a mass decrease of a maximum 16 wt%. However, the mass decrease was measured to be -18 wt% for sample 4, 2 wt% more than possible by evaporation of volatiles and moisture alone. The remaining 2 wt% can be explained by several mechanisms: First of all, the combustion of charcoal is more than likely to have occurred. Secondly, charcoal can have reacted with SiO_2-condensates to form SiO- and CO-gas. Third, some charcoal may have fallen through the holes of the gas-permeable disc. And finally, uncertainties in the chemical analysis of the raw materials must be taken into account.

Samples 1 and 2 had a mass increase of 41 and 22 wt%, respectively. The theoretically calculated mass increase due to evaporation of volatiles and moisture and from the full conversion of fixC to SiC was found to be between 24 wt% (WB) and 35.5 wt% (DB). It comes with no surprise that some samples 1 and 2, which was found to contain elemental Si, have a larger mass increase than what was calculated. This is most likely due to the formation of elemental Si through Reaction (1.4), which has not been accounted for in the previous calculations. Some increase could also be traced to carbons in volatile species reacting to SiC.

5.3 Crystal morphology and growth mechanism

The crystals found on the grey-blue particle surface and the inside pore structure is believed to have different growths due to varying pressures of SiO-gas on these locations. The crystals found on the particle surface were often found to be larger poly-crystals. If it is assumed that the particle surface is exposed to a higher pressure of SiO-gas, or flux of SiO-gas, the poly-crystalline growth

is in fair agreement with the finds of Bloem (1979)[21]. As argued by Bloem, a high-temperature system with a high flux of reactants will prefer the formation of poly-crystals, such as found on many particle surfaces. Additionally, a high flux of reactants and the resulting larger growth rates can explain why the crystals on the surface are generally larger. Following the same finds of Bloem, the different mono-crystals typically found inside the pore structure is believed to originate from the lower exposure to SiO-gas. It is probable that the pressure of SiO-gas inside the pore structure is far lower than what is found on the particle surface, which is believed to be the reason for the two different crystal growths.

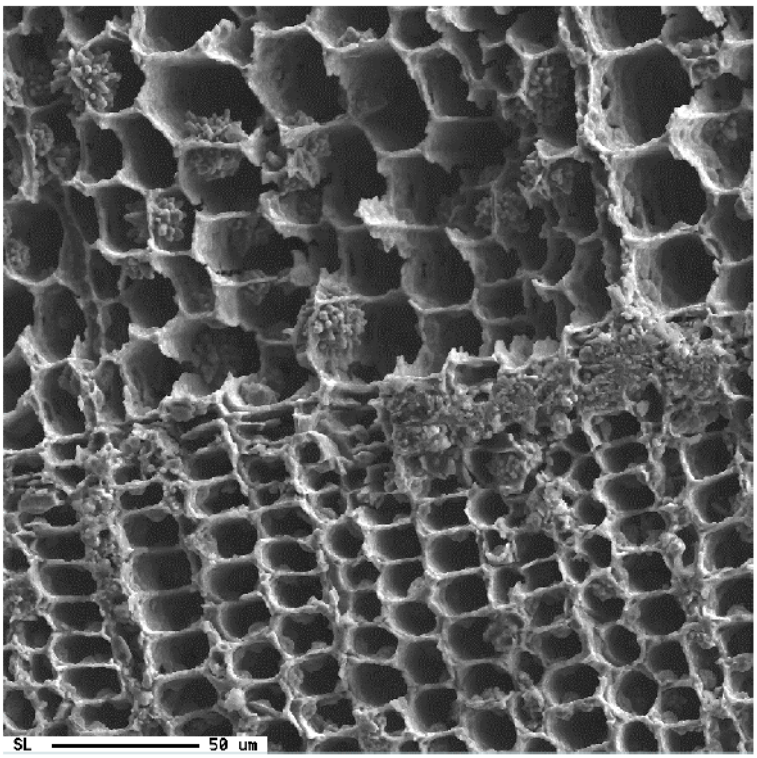

Figure 5.3: From Myrhaug (2003)[4]. Faint crystal growth inside the walls of a charcoal particle.

In the works of Myrhaug (2003)[4] charcoal particles were exposed to SiO-gas at 1650 °C. One image shown in Figure 5.3 of a partially converted charcoal particle show, what which looks like, poly-crystalline growth on the charcoal walls. Although not addressed by Myrhaug, it can be assumed that these crystals are SiC, similar to what has been found in this work. Although not specified by Myrhaug, it appears as these poly-crystals are found on the charcoal particle surface, similar to the finds in this work.

Although mostly poly-crystalline growth was seen on the particle surfaces, a few instances of mono-crystalline growth were also observed. Both mono- and poly-crystals found on the particle surface all indicated to an underlying hexagonal structure. Hence, these crystals may have an underlying

α-SiC structure. The morphology of these hexagonal crystals varied between hexagonal pyramids and hexagonal basal plates. These different crystal shapes are believed to have come from two different scenarios, where the hexagonal crystal is either bound by a slow-growing [0001] or [01$\bar{1}$1] index plane (Figure 5.4). As explained by Kurz & Fisher (1989)[15], the slowest growing index plane(s) tends to dictate the final crystal structure. A slow-growing [0001] index plane will result in a crystal with a morphology of a basal plate, while a fast-growing [0001] index plane might result in a hexagonal tube. These two scenarios are depicted in Figure 5.4 image **(a)**. Furthermore, a hexagonal pyramid morphology is believed to have occurred as the crystal is bound by a slow-growing [01$\bar{1}$1] index plane as illustrated in image **(b)**. Similar hexagonal pyramids were also found during the growth of hexagonal ZnS (wurtzite) crystals[17, 18].

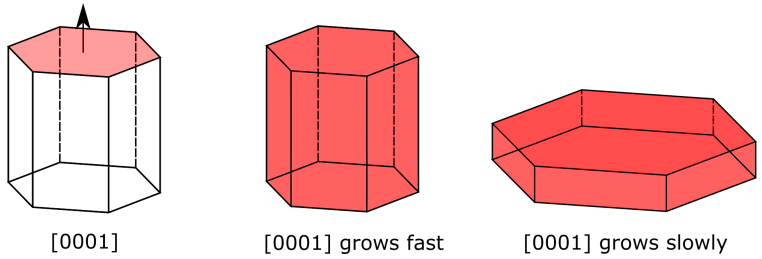

(a) Varying growth rates of [0001].

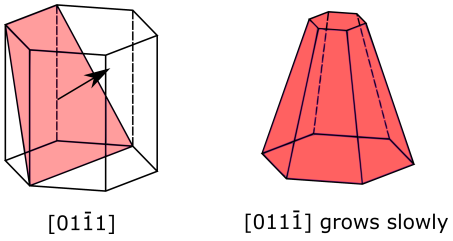

(b) Varying growth rates of [01$\bar{1}$1].

Figure 5.4: An illustration of how varying growth rates of the [0001] and [01$\bar{1}$1] index planes in the hexagonal crystal system can result in different crystal morphologies.

Naturally, the discovery of α-SiC at temperatures as low as 1781.1 °C is unexpected as α-SiC is believed to be stable only at temperatures above 2000 °C[7]. Still, there are several reports of α-SiC crystals grown at temperatures well below 2000 °C[19, 20]. These studies do however use assisted methods of growth and for that reason might limit their comparative value here. The morphology of the hexagonal crystals in such studies is identical to the crystals from this work. Consequently, a hexagonal polytype of SiC may be the best explanation for this hexagonal shape. Results from XRD analysis of sample 1, as seen in Figure 4.22, also gave some indications of 4H α-SiC together with a large amount of 3C β-SiC. One of the peaks indicating the 4H polytype is shown in the figure as the dotted line labeled α-SiC. Such peaks indicating the 4H polytype are quite small and occurs

in a region of the spectrum where β-SiC is susceptible to stacking faults. Such stacking faults in β-SiC have been investigated by Pujar et al. (1995)[29]. Stacking faults makes identification of small concentrations of hexagonal polytypes difficult. Yet, the characteristic peak of 4H is perfectly aligned with several small peaks from the grey-blue particle type spectrum. Moreover, the example of a typical β-SiC spectrum provided by Pujar et al., does not appear to have similar small peaks as seen in the grey-blue particle type.

Judging a polytype based on morphology alone would in any case not be accurate. Equally, as the XRD results only faintly indicates to the 4H-SiC polytype, the exact polytype of these hexagonal shaped crystals are yet to be confirmed. Still, both the morphology and XRD indicate to a α-SiC polytype.

As the transformation from β- to α-SiC is seen mostly above 2000 °C, α-SiC formed below this temperature might be metastable and may, given a sufficiently large temperature, transform back to β-SiC. If this theory of metastable α-SiC crystals is true, then a transformation of α- towards β-SiC might be more visible at higher temperatures, close to the 2000 °C limit. Consequently, a larger presence of hexagonal crystals without significant defects could be visible in samples exposed to low temperatures compared with high-temperature samples. However, the presence of elemental Si could also affect the morphology of these crystals. Hence, the yellow-green particles might be the best comparison. Following this hypothesis, the most perfect examples of hexagonal pyramid crystals were found in a yellow-green particle from sample 5 (1763.7 °C). The few such hexagonal crystals found in samples 1 and 2 had several flaws, as seen in 4.17, image **(e)**). Nevertheless, the hypothesis of hexagonal α-SiC being more common or apparent at low temperatures is still uncertain and will require more research to be confirmed.

Contrary to a metastable α-SiC, one could also assume that it is β-SiC who is metastable in a temperature range not far below 2000 °C. Besides, some older studies claim to have seen indications of this transformation of β- to α-SiC at temperature as low as 1200 °C[7]. This could explain the formation of α-SiC at temperatures below 2000 °C.

It is possible that the large amounts of α-SiC discovered in excavated furnaces by Ksiazek et al. (2014)[30] could be partially explained by crystal growth of α-SiC in the carbon charge, as found here. The leading hypothesis for these deposits of α-SiC in excavated furnaces have been the transformation from β- to α-SiC at temperatures above 2000 °C. It is believed that crystal growth of α-SiC in the carbon charge may more or less contribute to the accumulation of α-SiC in the furnace.

Inside the pores of the particles, a mono-crystalline cubic structure of SiC was often observed. The only cubic form of SiC is the 3C polytype, referred to as β-SiC. These are believed to have grown from a cubic structure where (110) planes are growing the slowest. Such a scenario was also illustrated

by Kurz & Fisher in Figure 2.7 image **(b)**. Looking at the third stage of conversion in this illustration, a similar morphology of square facets surrounded by hexagonal facets can be seen. The XRD results of sample 1 also found a large presence of the 3C β-SiC.

There are two proposed reaction mechanisms of crystal growth in this system:

1. A reaction between SiO- and CO-gas to form SiC and SiO_2, followed by a reaction between SiO_2 and C to reproduce SiO- and CO-gas. Remaining species on the surface would be SiC. This mechanism was proposed by Ramos (2018)[5] to explain deposits inside the charcoal structure.

2. A direct reaction between SiO-gas and diffused carbon atoms at the crystal surface to produce SiC and CO-gas. This mechanism is based on Reaction (1.5) and the diffusion of carbon atoms through the SiC crystals to the surface.

Reaction mechanism 1 does, however, seem unlikely as crystal growth was also common in samples exposed to temperatures well above the ternary point of 1800 or 1811 °C. Samples 1 and 2 were exposed to 1885.6 and 1831.0 °C, respectively, which is well above the maximum temperature for the decomposition of unstable gases according to the equilibrium diagram (Figure 5.2). A temperature below the ternary point, along with a fairly large partial pressure of SiO-gas, would be necessary for the reaction between SiO- and CO-gas. As the temperatures of samples 1 and 2 were above the maximum for a reaction between SiO- and CO-gas, combined with the crystal growth found in these samples, reaction mechanism 1 seems unlikely. It is emphasized that this argument is based on a theoretic equilibrium diagram. Yet, as almost no condensates were discovered, reaction mechanism 2 seems more probable.

As the growth of crystals stops at a diameter of about 30 μm, there must be some limiting factor. Both suggested reaction mechanisms require a sufficient pressure of SiO-gas and the diffusion of carbon through the crystal. Reaction mechanism 1, which used SiO_2 as an intermediate species, also requires a pressure of CO-gas. Below are two suggestions for crystal growth retardation which applies for both proposed reaction mechanisms.

First of all, the retardation of crystal growth could occur through decreasing pressures of SiO-gas. SiO-gas is produced using a batch of Si and SiO_2. Contrary to a continuous production, the SiO-gas pressure will at some point decrease due to the consumption of Si and SiO_2. As the pressure of SiO-gas decreases and the flux of reactants to the crystals is limited, the crystal growth will stop. Yet, from Figure 4.1 large remains of Si/SiO_2 can be seen at the bottom of the crucible. Consequently, unless the flux of SiO-gas has been hindered to the carbon charge or been diluted by CO- or Ar-gas, this growth retardation mechanism seems less likely. Secondly, the retardation of crystal growth

could occur due to an increasingly larger diffusion distance of carbon through the crystal. As the crystals grow, the distance of carbon diffusion to the crystal surface increases and a logarithmic growth rate can be expected. Such a retardation mechanism has been seen before. The growth rates of SiC-layers between liquid Si and glassy carbon have previously been studied and found to exhibit a logarithmic growth behavior due to the diffusion of carbon-ion vacancies through the growing SiC layer[31].

5.4 Structural changes

As charcoal is exposed to SiO-gas and is converted to SiC, significant structural changes was found to occur in many samples. As partially converted particles were investigated (Figure 4.9) a contrast between the structures of charcoal and converted SiC was easily seen. The most striking difference, is the lack of smaller pores in areas containing SiC. However, larger pores still remained in SiC after the conversion from charcoal.

It is hypothesized that the growth of SiC crystals will clog and effectively remove the smaller sized pores in charcoal. The smaller pores inside the charcoal area were investigated using higher magnifications in Figure 4.11. From this Figure, a large amount of SiC crystals can be seen covering the internal surface of the pores. These crystals found on the pore walls closely resemble the crystals found on the particle surface. Although too small for accurate size measurements, the smallest of these crystals are estimated to be around 0.1 μm in diameter. If these crystals were to grow to the maximum size of 20 μm diameter as found other locations inside the pore structure, logically, they would completely clog the pore. The lack of smaller pores in areas containing SiC, as discovered above, combined with the find of small crystal particles inside the small pores, leads to the hypothesis of pore clogging as these crystals grow larger. Similarly, the growth of SiC crystals was also observed in larger pores, however, as the crystal growth is limited, the larger pores are not completely clogged and remain in the converted SiC (image **(a)** in Figure 4.10).

Ramos (2018)[5] did not find the same extent of structural changes as found in this work. Ramos exposed charcoal to SiO-gas at 1650 °C and concluded that the resulting charcoal structure is mostly preserved. Yet, a few deposits of SiC which is said to have resulted in a reduced fiber lumen (or cell wall) diameter can be seen in Figure 5.5. This observation of SiC deposits only further supports the theory of structural changes due to pore clogging as suggested above. In comparison with Ramos, the charcoal in this work was exposed to much higher temperatures (all above 1750 °C), and most displayed significant structural changes. For this reason, it is believed that structural changes are more significant at higher temperatures. Following this theory, a lower structural change was found

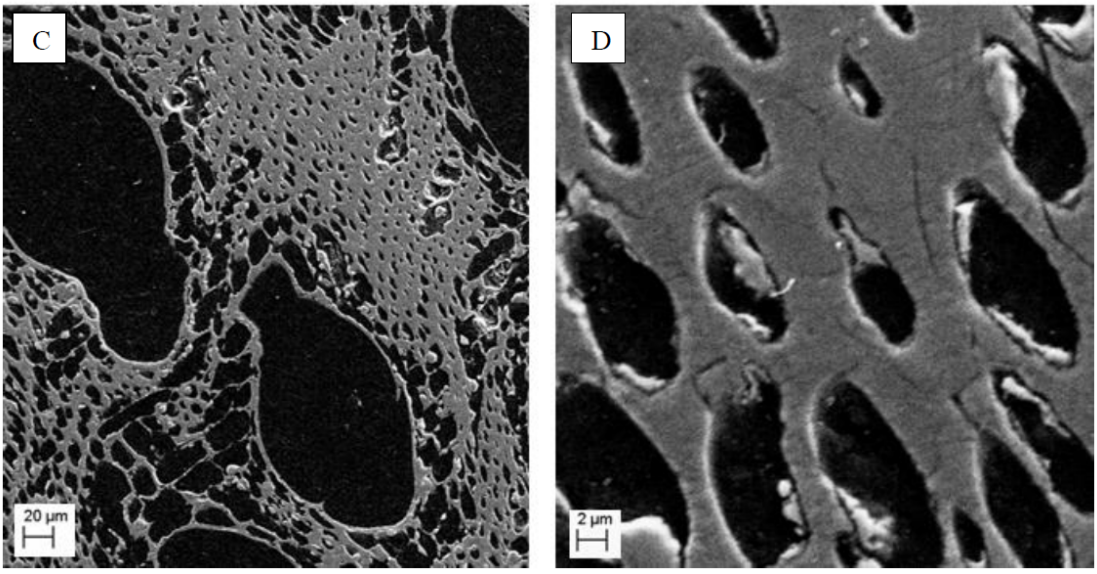

(a) Ramos (2018)[5]

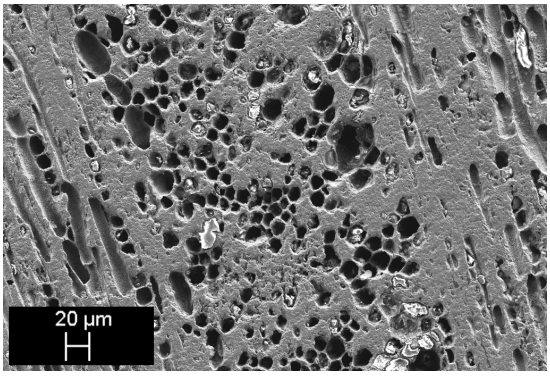

(b) (S4 - 1757.8°C)

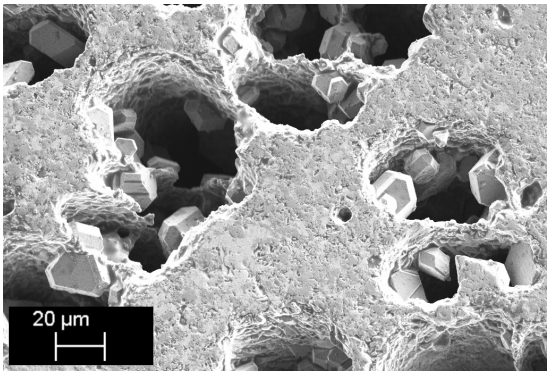

(c) (S2 - 1855.0°C)

Figure 5.5: Previous studies did not show the extent of structural transformations as seen in this work. The two images in **(a)** from Ramos (2018)[5] show a converted particle of charcoal and the deposits of SiC, which has lead to a reduced diameter of the fiber lumen (or cell wall) diameter. In comparison, there are two images in **(b)** and **(c)** from this work. The results from Ramos are more similar to sample 4, where less structural changes were seen. A lower temperature of sample 4, closer to 1650 °C which Ramos used, is believed to be the reason for this. Structural changes are much more significant in sample 2, which have been exposed to higher temperatures.

in sample 4 (1758.8 °C) compared with sample 2 (1885.7 °C), see difference between images **(b)** and **(c)** in Figure 5.5. Yet, it is emphasized that very few particles of SiC were obtained from both samples 4 and 5 due to a low temperature exposure. Subsequently, a further investigation of this theory might be required.

5.5 Phase analysis

The black, yellow-green, and grey-blue particle types were found to contain an increasing amounts of SiC and elemental Si. The black particles were found to contain mostly unreacted charcoal, with traces of SiC in form of layers or scattered crystals. The yellow-green particles contained both SiC and unreacted charcoal. Finally, the grey-blue particles were found to contain mostly SiC, with varying amount of elemental Si. No correlation between the formation of SiC and temperature were found.

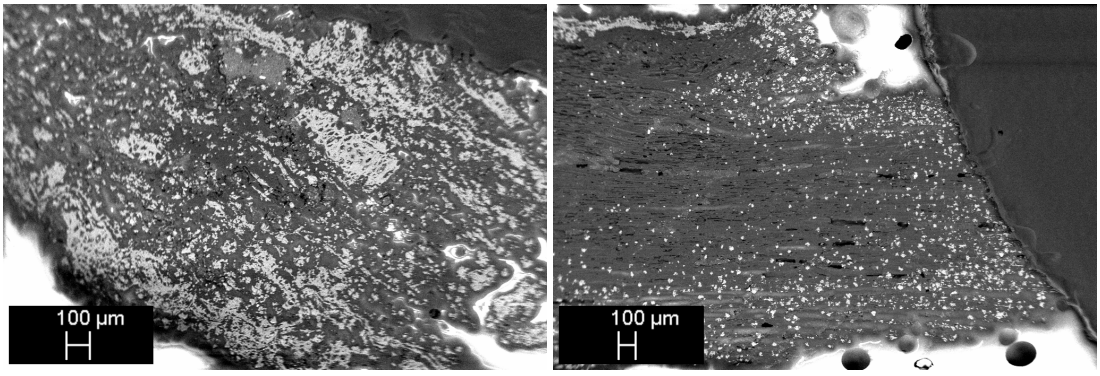

(a) (S1 - 1885.7°C: BSE 49X 10kV **(b) (S4 - 1757.8°C**: BSE 35X 10kV

Figure 5.6: Although most particles show a shrinking-core model, some particles also appear near a volume-control model where the reaction occurs simultaneously throughout the particle volume. The two images show how crystals of SiC are often found scattered throughout the particle, although larger concentrations are sometimes seen near the particle surface. A volume-control model, where the reaction occurs simultaneously throughout the entire volume is explained by Rosenquist (2004)[14] to best describe the kinetics of smaller porous particles.

While investigation the partially converted particles of charcoal, the shrinking-core model is somewhat visible, although a volume-control model also seems applicable. A few particles gave indications of the shrinking-core model with layers of SiC originating from the surface, however, many partially converted particles were found to have SiC scattered throughout the particle (see Figure 5.6). Yet, a larger concentration of scattered SiC is often found closer to the particle surface, which is typical of a shrinking-core model. In comparison, a reaction that takes place throughout the entire parti-

cle simultaneously is typical of the volume-control model. According to Rosenquist (2004)[14], the volume-control model best describes particles that are both small and very porous.

Myrhaug (2003)[4] used an average particle size of 5.2 mm, compared with the 4-4.7 mm used in this thesis. In the work of Myrhaug, the shrinking-core model was well indicated in resulting SEM images, although an increased degree of conversion was seen along the porous cell structure of charcoal. This was an indication that porous structures transport SiO-gas better than other structures. Ramos (2018)[5] used a particle size of 2-4.5 mm and the same shrinking-core model appeared. Both authors used the same temperature of 1650 °C. As Ramos used a similar particle size, the remaining main difference between the works of Myrhaug and Ramos, and this work, is temperature. All experiment in this work was done at temperatures above 1750 °C.

Contrary to a shrinking-core model, some particles were found to have elemental Si concentrating the center of the particle. Peculiarly, as seen in image **(a)** of Figure 4.14 elemental Si is found in the center of the particle and is surrounded by a crust of SiC. This is not proof that Si is formed in a growing-core model, as the formed Si will be in a liquid state. Consequently, as liquid Si is formed at high temperatures, movement of this phase can be expected. The results of Jayakumari (2018)[1] as seen in Figure 2.14 also indicate that the formed Si is more likely to concentrate the particle center. Possibly, as the solid grains of SiC floats around in a particle of mostly liquid Si, the SiC will attach themselves to the liquid surface to the due to capillary forces. Next, more and more grains of SiC attach themselves to an increasing layer of SiC at the liquid surface, again due to capillary forces. The result would be liquid Si surrounded by a crust of SiC as seen in image **(a)** of Figure 4.14.

5.6 Formation of elemental Si

The lowest temperature of elemental Si formation was found in sample 5 and measured 1781.8 °C. Only two grey-blue particles was found in the carbon charge of sample 5, and both were found to be composed of elemental Si in SiC. The temperature in the carbon charge of sample 5 measured 1781.8 ± 17.8 °C. One of these two grey-blue particles are seen in Figure 4.15. Here, two larger areas composed of pure Si is visible, surrounded by a matrix of SiC with small grains of additional Si. An EDS analysis was also performed to confirm the presence of elemental Si.

Although sample 4 was subjected to very similar temperatures as sample 5, no elemental Si could be discovered in this sample. Samples 4 and 5 measured the same maximum temperature, but different stabilized temperatures. Sample 4 had measured a stabilized temperature of 1757.8 ± 17.6, which is ~5 °lower than sample 5. This might explain why elemental Si was not found in sample 4. However, it is also possible that elemental Si was present, but not discovered in the following

characterization.

The results from this work, indicate that the minimum temperature of elemental Si formation through Reaction (1.4) is around 1780 °C. In most cases, grey-blue particles were found to contain elemental Si in various amounts. Yet, as seen in Table 4.1, the amount of these grey-particles in samples 4 and 5 is less than 0.1 gram. This corresponds to about 1 % of the original mass of charcoal added to each sample. To make matters worse, the content of grey-blue particles are often found to be mostly SiC. Hence, the actual amount of elemental Si in each of these two samples is far less than 1%. This implies that samples 4 and 5 are close to a critical temperature where elemental Si is formed.

There is an important uncertainty regarding the formation of elemental Si below 1800 °C which has to be addressed. According to the equilibrium diagram in Figure 5.2 elemental Si can be formed at temperatures below the ternary point if the partial pressure of SiO-gas is sufficiently high. However, such a large partial pressure of SiO-gas would require a passage through the region termed "unstable gas" which would result in the formation of SiO_2. In other words, if this equilibrium diagram is assumed to be correct, and if elemental Si is found below the ternary point of 1800 °C, SiO_2 can have been formed in addition.

Let us assume that the equilibrium diagram is correct and that the samples have at some point traveled through the unstable gas region. Yet, no SiO_2 was discovered in the following sample analysis. Hence, it implies that the reactions occurring in the "unstable gas"-region is much slower than the formation of elemental Si. As previously mentioned, some of the grey-blue particles were found partially "glued" to the gas-permeable disc and had to be removed using weak mechanical force. This was true for many of the samples. If this "glue" is assumed to be SiO_2, the exact origin of it is still a mystery. It could have been formed as samples are held at high temperature, or it could have been formed from the decomposition of SiO-gas during the final cooling of samples. All in all, it is difficult to know. Nevertheless, it seems more likely that this glue is elemental Si since no SiO_2 was discovered in the following SEM analysis. Furthermore, such glue was also discovered in samples which were treated above 1800 °C, which makes the glue more likely to be elemental Si.

The finds of elemental Si at temperatures below 1800 °C correspond to the results of Jauakumari (2018)[1]. The particle containing elemental Si was found right next to the thermocouple which measured a maximum temperature of 1781.8 ± 17.8 followed by a stabilized temperature of 1763.7 ± 17.6. These temperatures include the upper and lower accuracy range of a C-type thermocouple. Similarly, Jayakumari found elemental Si in SiC at a temperature measured to be between 1762 and 1783 °C. This was done in an open induction furnace resulting in a total pressure of 1 atm. Although a very similar experimental setup was used the experiment of Jayakumari was performed in a much larger induction furnace, which makes accurate temperature measurements difficult. Furthermore,

a total gas pressure of 1.45 bar was measured during these experiments, in comparison with Jayakumari's 1 atm experiments. As elemental Si was discovered below 1800 °C in both experiments, the effect of the increased total pressure seems negligible. Nevertheless, the finds of elemental Si at temperatures below 1800 °C by Jayakumari are further supported by the results in this thesis.

Chapter 6

Conclusions

The relative mass change of particles collected from the carbon charge after experiments were found to follow a linear trend when plotted against temperature. These results, as seen in Figure 4.3, show an increase in the mass of the carbon charge at temperatures above ∼1775 °C. Accordingly, samples subjected to temperatures below 1775 °C was found to have a decline in the mass of the carbon charge. Simultaneously, the evaporation of volatiles and moisture causes a mass decrease, while the formation of SiC and Si causes a mass increase. At temperatures below 1775 °C, the evaporation effect dominates, while the SiC formation is more prominent at larger temperatures.

The particles collected from the carbon charge were divided into three groups by colour: black, yellow-green, and grey-blue. The black particles was identified to be mostly unreacted charcoal, with traces of SiC in the form of layers or crystals. Furthermore, the yellow-green particles consist of both SiC and unreacted charcoal. Finally, the grey-blue particles were found to contain mostly SiC with various amounts of elemental Si.

Both mono- and poly-crystalline growth was observed on the particle surfaces and inside the pores structure. However, poly-crystals up to 30 μm diameter were found to be more common on the surface, while mono-crystals with a maximum size of 20 μm diameter was typical inside the pore structure. A possible explanation for this difference in crystal morphology is a larger pressure of SiO-gas on the surface compared with the inner pore structure. Similarly, a larger pressure of SiO-gas on the surface can explain why the crystals grown there are larger. The growth of these crystals are believed to have occurred through a reaction between SiO-gas and diffused C on the crystal surface. To account for the growth retardation, two mechanisms are proposed: an increased distance for carbon diffusion, and decreasing SiO-gas pressure due to batch production.

The morphology of these crystals indicates to both hexagonal α-SiC and cubic β-SiC. The morphology of crystals found on the particle surface was mostly hexagonal pyramids or basal plates, indicating to α-SiC. Similarly, spherical cubes found inside the inner pore structure of particles indicate to β-SiC. XRD confirmed the presence of 3C β-SiC and gave further indications of 4H α-SiC.

The initial porous structure of charcoal changes as it is converted to SiC. Smaller pores were found to be lacking in converted SiC particles, while larger pores remained. A mechanism of crystal growth and resulting pore clogging is proposed. These structural transformations are seen to be more prominent at higher temperatures.

There are indications that the reaction to form SiC and Si occurs much faster than the condensation reaction which produces SiO_2. Further investigations are required to confirm this.

The formation of elemental Si in SiC was found to occur at 1781.8 °C. A grey-blue particle collected from sample 5 was found to contain small amounts of elemental Si when investigated in SEM (Figure 4.15). It was confirmed by EDS analysis that this brightly coloured phase is elemental Si. This grey-blue particle was found close to the thermocouple, which measured a maximum temperature of 1781.8 ± 17.8 °C during the 1 hour holding time. A few grey-blue particles collected from sample 4, did not show any elemental Si. Sample 4 was exposed to the same initial maximum temperature, but a ~5 °C lower stabilized temperature of 1757.8 °C. Hence, while using SiO_2/Si to form SiO-gas, the production of Si might occur around 1780 °C.

Bibliography

[1] S. Jayakumari. “Experimental procedure and results: Induction furnace/ReSiNa furnace/Hot press”. Unpublished. Data collected by personal communication. 2018.

[2] M. Ksiazek, M. Tangstad, and E. Ringdalen. “Five furnaces five different stories”. In: *Silicon for the Chemical and Solar Industry XIII* (June 2016).

[3] J. K. Tuset and O. Raaness. “Reactivity of Reduction Materials for the Production of Silicon, Silicon-Rich Ferroalloys and Silicon Carbide”. In: New York: American Institute of Mining, Metallurgical, and Petroleum Engineers, 1976, pp. 101–107.

[4] E. H. Myrhaug. *Non-fossil reduction materials in the silicon process : properties and behaviour*. eng. Trondheim, 2003.

[5] D. C. Ramos. *Quality of eucalyptus charcoal for use in silicon production*. eng. Mina Gerais, Brazil, 2018.

[6] R. T. Dolloff. *Research study to determine the phase equilibrium relations of selected carbides at high temperatures*. Tech. rep. Parma, Ohio: Research Laboratory of National Carbon Company, 1960.

[7] G. Harris. *Properties of Silicon Carbide*. eng. Institution of Engineering and Technology, London, 1995, pp. 1–16 & 189.

[8] K. Wiik. *Kinetics of reactions between silica and carbon*. eng. Trondheim, 1990.

[9] R. E. Johnson and A. Muan. “Phase Diagrams for the Systems Si-O and Cr-O”. In: *Journal of the American Ceramic Society* 51.8 (1968), pp. 430–433.

[10] A. Schei, J. K. Tuset, and H. Tveit. *Production of High Silicon Alloys*. Trondheim: Tapir, 1998, pp. 25–30.

[11] A. F. Wells. *Structural inorganic chemistry*. eng. Oxford, 1984.

[12] J. Szekely. *Gas-solid reactions*. eng. New York: Academic Press, 1976.

[13] S. Yagi and D. Kunii. “Studies on combustion of carbon particles in flames and fluidized beds”. eng. In: vol. 5. 1. University of Pittsburgh: Elsevier Inc., 1955, pp. 231–244.

[14] T. Rosenqvist. *Principles of extractive metallurgy*. eng. 2nd ed. Trondheim: Tapir Academic Press, 2004.

[15] W. Kurz and D. J. Fisher. *Fundamentals of solidification*. eng. 3rd ed. Aedermannsdorf: Trans Tech Publications, 1989, pp. 34–41.

[16] A. A. Chernov. “The spiral growth of crystals”. eng. In: *Soviet Physics Uspekhi* 4.1 (1961), pp. 116–148.

[17] B. Sotillo, P. Fernández, and J. Piqueras. “Growth by thermal evaporation of Al doped ZnS elongated micro- and nanostructures and their cathodoluminescence properties”. eng. In: *Journal of Alloys and Compounds* 603 (2014), pp. 57–64.

[18] B. Sotillo et al. “Gallium doped ZnS micro- and nanostructures: thermal synthesis and structural properties”. eng. In: 2.3 (2015).

[19] S. Harada et al. “Reduction of Threading Screw Dislocation Utilizing Defect Conversion during Solution Growth of 4H-SiC”. eng. In: *Materials Science Forum* 740 (2013), pp. 189–192.

[20] H. Matsunami. “Recent growth in Epitaxial Growth of SiC”. In: Santa Clara: Springer, 1991, pp. 3–12.

[21] J. Bloem. “Improved SINTEF SiO-reactivity test”. In: Princeton: Electrochemical Society, 1979, pp. 41–58.

[22] G. Cao. *Nanostructures & Nanomaterials : synthesis, properties & applications*. eng. London: Imperial College Press, 2004.

[23] H. E. Buckley. *Crystal growth*. eng. New York: Wiley, 1951, p. 339.

[24] T. Lindstad et al. “Improved SINTEF SiO-reactivity test”. In: Delhi: Macmillan India, 2007, pp. 414–423.

[25] I. Ødegård. “Unpublished PhD”. Personal communication. 2018.

[26] C. O. Gomez, D. W. Strickler, and L. G. Austin. “An Iodized Mounting Medium for Coal Particles”. In: *Journal of Electron Microscopy Technique* 1.3 (1984), pp. 285–287.

[27] J. Piňos, Š. Mikmeková, and L. Frank. “About the information depth of backscattered electron imaging”. In: *Journal of Microscopy* 266.3 (2017), pp. 335–342.

[28] R. Castaing. *Application des sondes electronique a une methode d’analyse ponctuelle chimique et cristallographique*. French. PhD Thesis. University of Paris, 1952.

[29] V. V. Pujar, J. D. Cawley, and S. R. Levine. *Effect of Stacking Faults on the X-Ray Diffraction Profiles of Beta-SiC Powders*. eng. 1995.

[30] M. Ksiazek, M. Tangstad, and J. E. Andersen. “Zones and materials in the Si furnace”. In: *Silicon for the Chemical and Solar Industry XII* (June 2014).

[31] H. Zhou and R. Singh. “Kinetics model for the growth of silicon carbide by the reaction of liquid silicon with carbon”. English. In: *Journal of the American Ceramic Society* 78.9 (1995), pp. 2456–2462.

Appendices

Appendix A

SEM

Results from the EDS analysis of different areas are presented below. Keep in mind that the volume of which the EDS interacts with can extend out of the area which is of interest. In addition, once a spot is chosen, the actual position of this spot can move during the EDS analysis. Hence, the values should only be use for qualitative analysis.

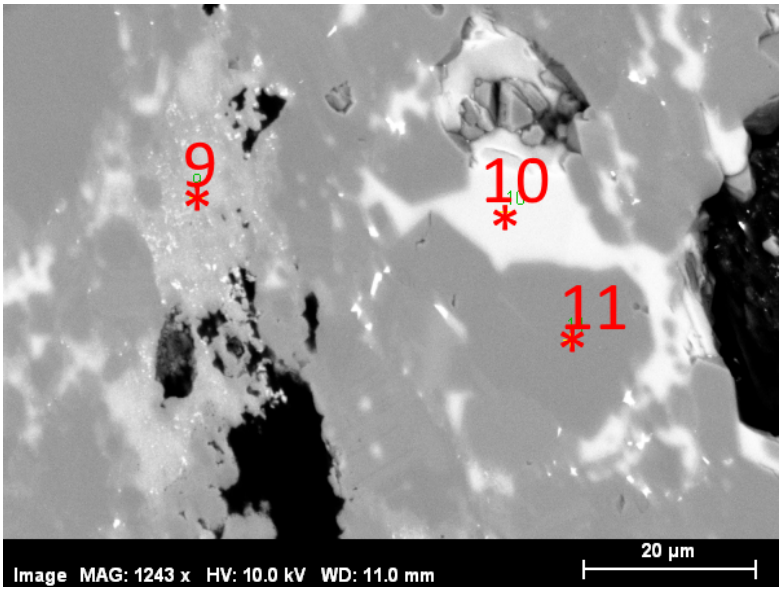

(a)

Spot	C (at%)	O (at%)	Si (at%)
9	55.31	3.39	40.69
10	-	-	94.24
11	14.79	-	80.27

(b)

Figure A.1: (S1 - 1885.7°C): Grey-blue particle

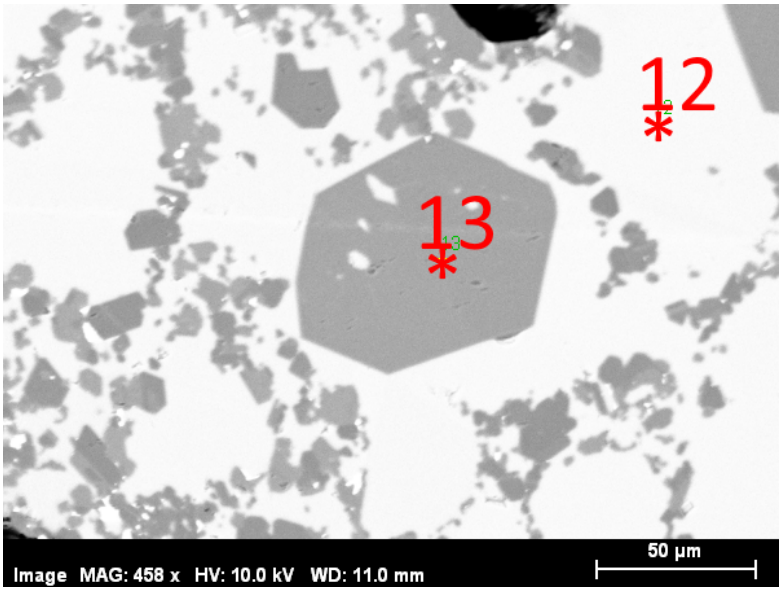

(a)

Spot	C (at%)	O (at%)	Si (at%)
12	-	-	94.17
13	16.90	-	78.27

(b)

Figure A.2: (S1 - 1885.7°C): Grey-blue particle

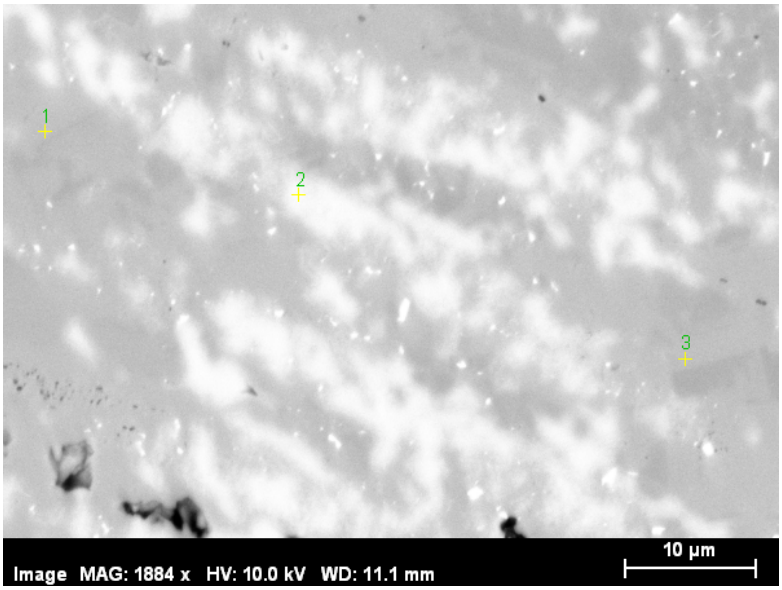

(a)

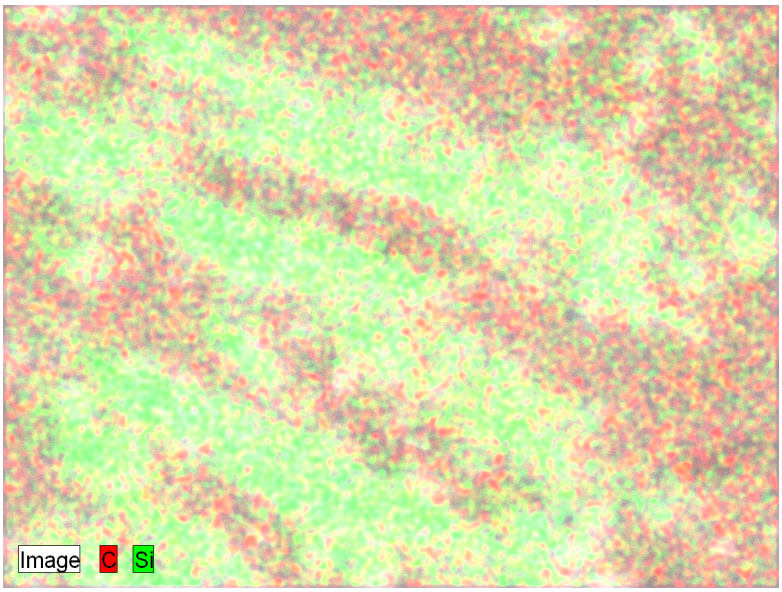

(b)

Figure A.3: (S1 - 1885.7°C): Grey-blue particle. In **(b)** a mapping technique is used of an area containing Si in SiC. Image **(a)** and **(b)** depicts the same area.

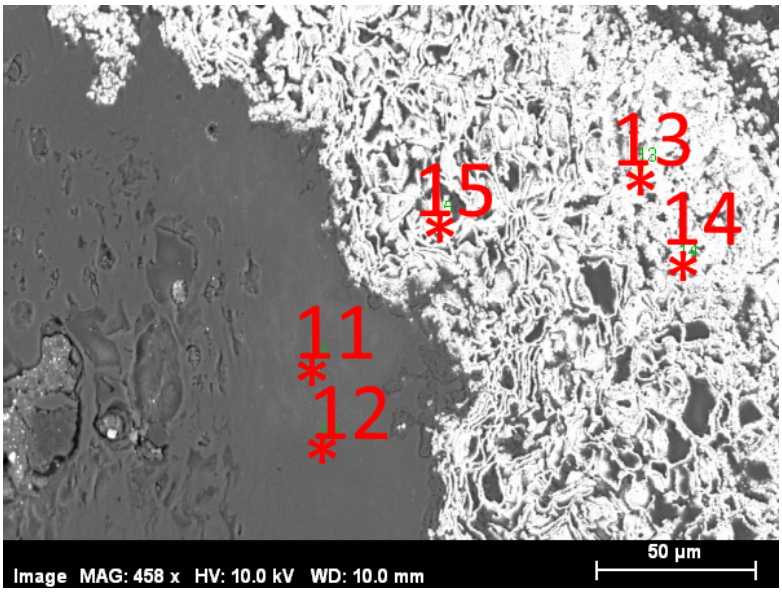

(a)

Spot	C (at%)	O (at%)	Si (at%)
11	97.49	0.73	0.60
12	98.47	0.80	0.31
13	31.99	1.13	62.96
14	47.68	1.28	51.04
15	68.91	4.39	25.16

(b)

Figure A.4: (S1 - 1885.7°C): Black particle, SiC-layer surrounding C bulk.

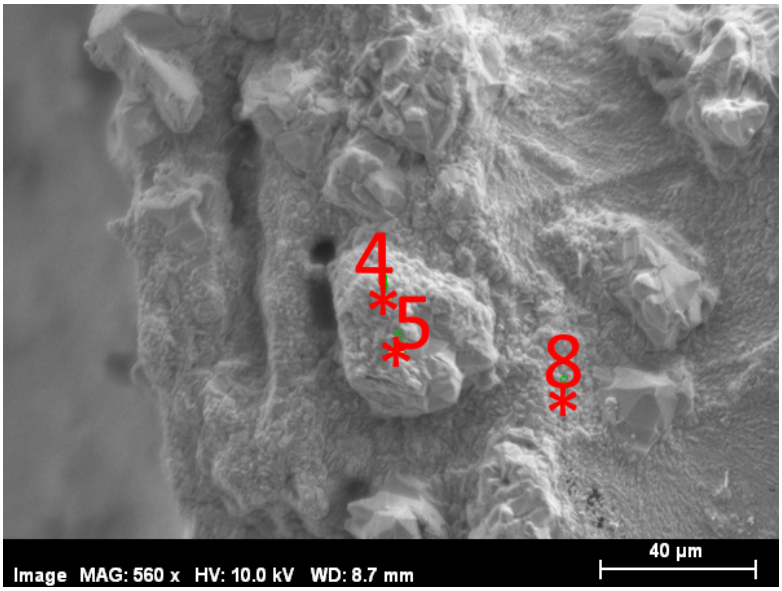

(a)

Spot	C (at%)	O (at%)	Si (at%)
4	61.01	0.78	38.10
5	33.23	2.87	62.49
8	63.84	5.03	31.05

(b)

Figure A.5: (S1 - 1885.7°C): Growth of a smaller particle on the surface of the grey-blue particle.

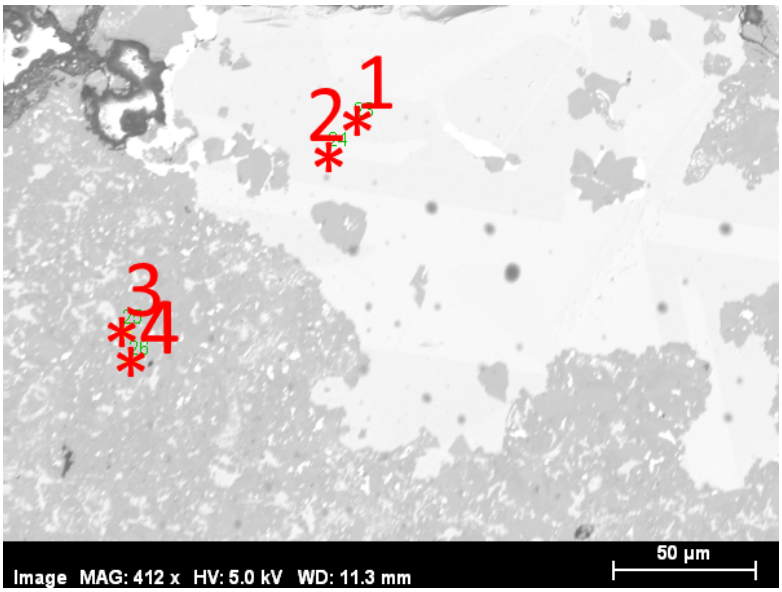

(a)

Spot	C (at%)	O (at%)	Si (at%)
1	2.03	0.56	97.41
2	1.93	0.50	97.57
3	36.11	0.46	63.44
4	40.14	0.75	59.10

(b)

Figure A.6: (S5 - 1763.7°C): Phase of elemental Si surrounded by a SiC with Si matrix.

Appendix B

XRD

Results from the XRD and TOPAS analysis of the different particle types, including references, are presented below. It should be kept in mind that the TOPAS software can only do qualitative analysis. The software looks for the elements it is told to look for. Hence, the amounts of each phase discovered is only qualitative comparable with other phases it was told to look for. Due to technical difficulties, carbon was never investigated with TOPAS. This error is well demonstrated by the black particles which is known to contain mostly carbon, although TOPAS analysis gives 100% SiC-3C (β-SiC). TOPAS also looked for 4H, 6H and 15R polytypes of SiC, but only indications of 4H was found in the grey-blue sample.

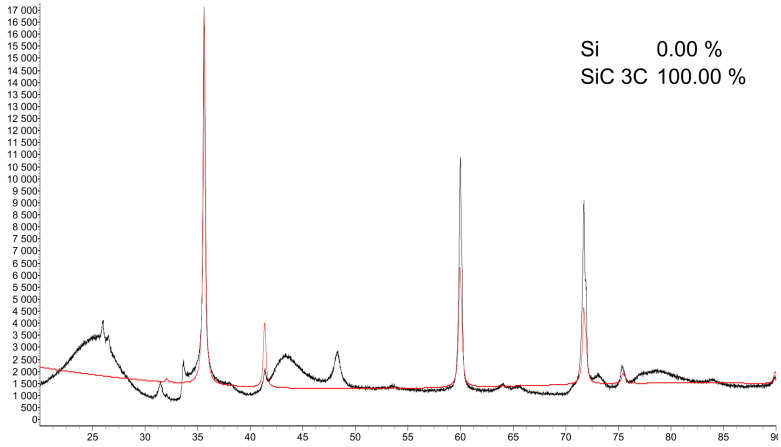

(a) Black particle

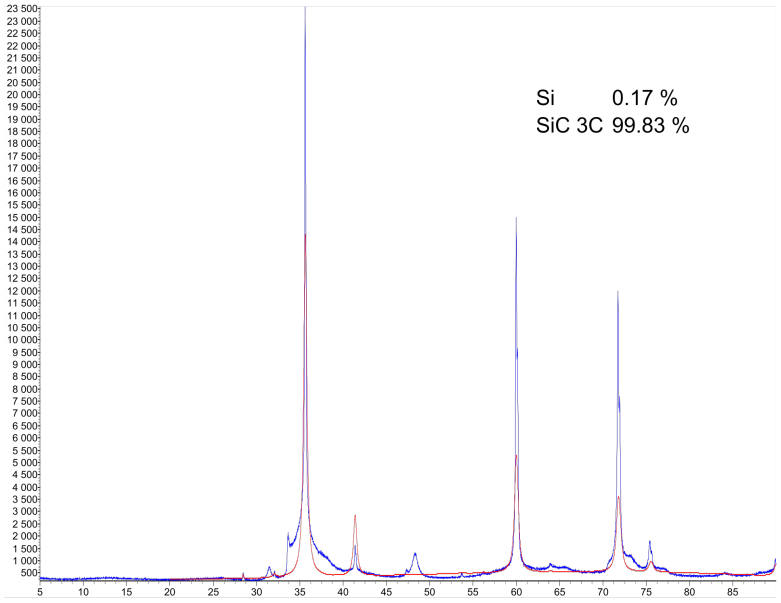

(b) Yellow-green particle

Figure B.1: (S1 - 1885.7°C): Results from XRD and TOPAS qualitative analysis of black, **(a)**, and yellow-green, **(b)**, particle types. Note that the black particle does not contain 100% β-SiC, as carbon was not looked for.

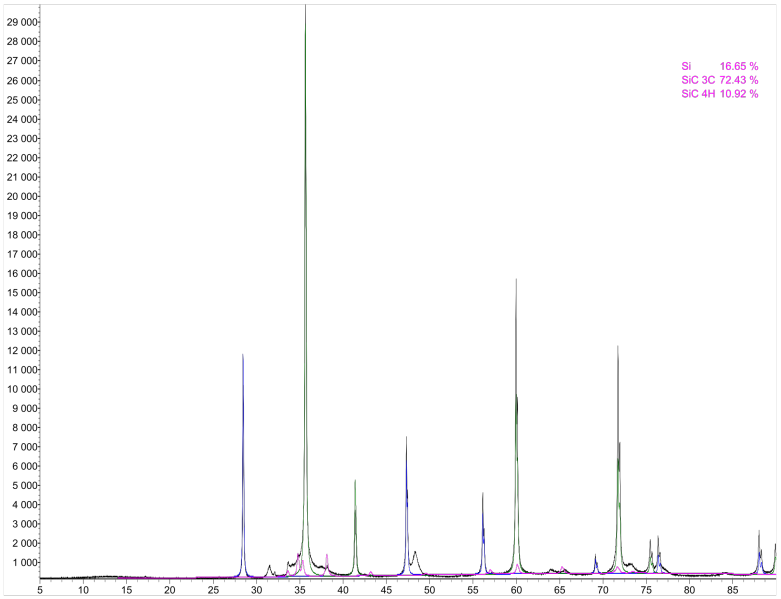

(a) Grey-blue particle

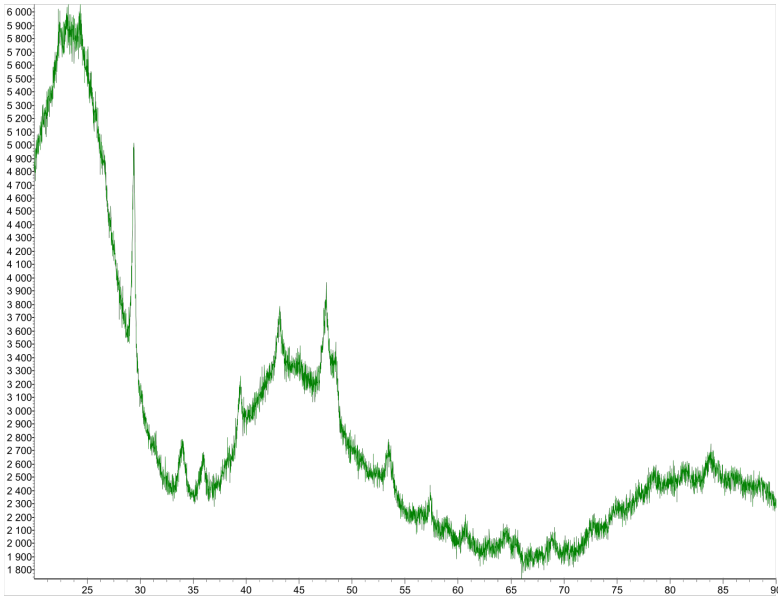

(b) Charcoal particle

Figure B.2: (Sample 1): Results from XRD and TOPAS qualitative analysis of grey-blue, **(a)**, and charcoal, **(b)**, particle types. The charcoal particle is added as a reference.

Appendix C

Risk Analysis

Endelige vurderinger (må fylles ut før lukking) *

Fyll ut begrunnelser og kommentarer til restrisiko, samt om usikkerhet ved vurderingen (f.eks. om den er av generell art, om vurderingen er basert på få personer etc.).

De er lite eksponering til farlige kjemikalier, og ved bruk av ventilasjonsskap og vernebriller, samt hansker, er dette beregnet til å være trygt. Ovnene som brukes til forsøk skal aldri forlates eller brukes etter normal arbeidstid.

Hjelp

Endelig resultat

I tabellen under er hver uønsket hendelse merket med det endelige resultatet av risikovurderingen.

Konsekvensområde	Resultat	Resultat etter tiltak
▲ *Farekilde:* Casting with iodoform epoxy [57265]		
▲ *Uønsket hendelse:* Not casting with ice and water [71162]		
Materielle verdier	Akseptabel risiko	
▲ *Farekilde:* Cleaning of furnace [55513]		
▲ *Uønsket hendelse:* Exposure to dust [68690]		
Helse	Akseptabel risiko	
Materielle verdier	Akseptabel risiko	
▲ *Farekilde:* Gas leak [54913]		
▲ *Uønsket hendelse:* Ar-leak [71161]		
Helse	Akseptabel risiko	
▲ *Uønsket hendelse:* Breathing of CO gas [67566]		
Helse	Akseptabel risiko	
▲ *Farekilde:* High temperatures [54914]		
▲ *Uønsket hendelse:* Burn damages [67567]		
Helse	Akseptabel risiko	
▲ *Uønsket hendelse:* Water cooling [67568]		
Helse	Akseptabel risiko	
Materielle verdier	Akseptabel risiko	
▲ *Farekilde:* Preparation of raw materials [55514]		
▲ *Uønsket hendelse:* Breathing of dust during seiving [68691]		
Helse	Akseptabel risiko	